UNIVERSIDAD COMPLUTENSE DE MADRID

FACULTAD DE CIENCIAS FÍSICAS

UNIVERSIDAD
COMPLUTENSE
MADRID

TESIS DOCTORAL

Advanced scintillator readout for fast-timing experiments and its application to A=130 nuclei

Lectura avanzada de centelleadores para experimentos de coincidencias ultrarrápidas y su aplicación a núcleos con A=130

MEMORIA PARA OPTAR AL GRADO DE DOCTOR
PRESENTADA POR
Javier Rodríguez Murias

Directores:
Luis Mario Fraile Prieto
Paolo Mutti

To my family,

for all the love and support.

To my friends,

for all the good times and encouragement.

and last but not least,

to me,

Why not?

"Two things are infinite: the universe and human stupidity;
and I'm not sure about the universe."

Albert Einstein (1879–1955)

Summary

Neutron-rich nuclei far from the stability line provide key information of shell evolution when approaching the doubly magic nuclei, which has been a hot topic for the last decades. The study of these regions provides information about nucleon interaction and helps to understand the collective behaviour. One of the most interesting regions is close to the ^{132}Sn nucleus, since it is a doubly magic nucleus with Z=50 and N=82.

This thesis is divided clearly on two sections: the development of a magnetically compatible readout based on SiPM sensor for fast-timing measurements and the data analysis of ^{132}I (Z=53, N=77) and ^{130}Sn (Z=50, N=80) close to the ^{132}Sn region via fast-timing gamma spectroscopy measurements.

The first part of this thesis is focused on the development of a magnetically compatible readout for a SiPM-based detector. This comes as part of the ENDURANCE program at Insitut Laue Langevin (ILL), where one of the instruments (FIPPS) will be coupled to a recoil spectrometer based on a gas filled magnet making the PMT choice non-optimal for timing measurements. A SiPM based array has been developed since SiPM sensors are immune to magnetic fields. The chosen sensors are produced by Onsemi and two arrays have been developed within two different SiPM models: MicroFJ-30035-TSV and MicroFJ-60035-TSV. The selection of this brand is exclusively done based on the two output signals particular to all Onsemi sensors: the standard and the fast output. The readout treats each type of signal coming from the sensors differently, adding all the standard outputs to obtain the best energy response possible while the fast outputs have been grouped and only the fastest signals from each group contribute to the final output signal.

A full characterization of both SiPM-based arrays has been done and compared to an R9779 PMT, which is the choice for fast-timing measurements due to a fast response combined with good energy resolution. The results obtained display a very competitive 3.7% and a 3.9%, for the 30035-TSV and 60035-TSV SiPM-based detectors respectively, against the 4.0% for the PMT, while both maintain a good linearity. However, the time resolution from both of the SiPM sensors, 239 and 275 ps intrinsic time resolution at ^{60}Co energies, is still far from the PMTs 110 ps. This, combined with the evolution of SiPMs and future upgrades into the readout, makes the SiPM based array a future alternative to the PMT tube.

The last section of this thesis focuses of this thesis on the study of two nuclei within the ^{132}Sn region: ^{130}I (Z=53, N=77) and ^{130}Sn (Z=50, N=80). The expected proton-neutron multiplets in ^{130}I arise from the shell-model configurations in the region, with neutrons below N=82 and protons above the Z=50 gap. Their origin is the coupling of the proton $\pi g_{7/2}$ and $\pi d_{5/2}$ configurations with neutrons occupying the $\nu s_{1/2}$, $\nu d_{3/2}$, and $\nu h_{11/2}$ single particle orbits. On the other hand, the expected neutron-neutron couplings in ^{130}Sn arise from the shell-model configurations, with two neutron holes below the N=82 gap. Their origin comes from breaking a pair within the $s_{1/2}$,$d_{3/2}$ or from the $h_{11/2}$ shells.

Both nuclei have been investigated via fast-timing methods. This is an electronic coincidence method that employs fast scintillator detectors in order to extract the lifetimes from the excited states on each of the nuclei. Lifetimes are a key observable in order to understand the behaviour of exotic nuclei since it allows the access to the reduced transition probabilities that are important quantities for the study of single-particle configurations, nuclear collectivity and make it possible to test the theoretical models.

The nuclei under study were populated in two different experimental set-ups. The ^{130}I nucleus was populated on the ^{129}I(n,γ)^{130}I reaction and the experiment took place on the Fission Product Prompt Gamma Spectrometer(FIPPS) at the Institut Laue-Langevin. The experimental set-up consisted of an 8 HPGe detector array coupled to an ancillary device made of 16 $LaBr_3$(Ce) detectors. In order to reduce the analogue modules required for the fast-timing method, a multiplexed-start/multiplexed-stop set up was installed. The ^{130}Sn was populated in the beta-decay of the ^{130}In isomeric states at the IS610 experimental campaign. The experiment took place in the ISOLDE Decay Station (IDS) at the ISOLDE facility in CERN. Taking advantage of isomer selectivity from the RILIS station the three ^{130}In isomeric states were produced and their β-decay was studied. The IDS set up consist on 4 HPGe detector for high-resolution gamma spectroscopy coupled to a fast-timing set up, which consist on one beta and two $LaBr_3$(Ce) detectors with the standard analogue system in order to obtain coincidences that allow the extraction of lifetimes.

The results in ^{130}I yield no new γ-ray transitions or excited levels from the previous experiment performed in the 80s, so lifetime measurements have been the focus of the analysis. However, several new lifetimes have been obtained via triple coincidences between the HPGe and two LaBr detectors. The lifetime is extracted between the $LaBr_3$(Ce)-$LaBr_3$(Ce) coincidences, adding the third coincidence in the HPGe detector for branch selectivity since the ^{130}I level scheme is complex. Three new lifetimes are reported for the $(3,4)^-$, $(4)^-$ y $(5)^-$ excited states, yielding values of 24(9), 129(6) y 45(13) ps respectively.

The nuclear structure of ^{130}Sn has been performed and the level scheme has been expanded with 8 new excited levels and 14 new γ-ray transitions added to the previously known structure for each decay. The β-decay lifetimes of the ^{130}In isomeric states have been measured via using the time stamps of the HPGe detectors and results agree with the previously measured values. The 10^+ and 5^- states have

been reviewed, yielding values of $T_{1/2}$=1.48(6) μs and $T_{1/2}$=50.7(2) ns which are in good agreement to prior measurements. Lastly, two new lifetimes have been obtained from this decay, being the 8^+ state populated on the ^{130m1}In with a value of $T_{1/2}$=321(10) ps and the 6^+ state with a value of $T_{1/2}$=68(3) ps.

Resumen

Los núcleos ricos en neutrones alejados de la línea de estabilidad proporcionan información clave de la evolución de la estructura nuclear cuando se aproximan a los núcleos doblemente mágicos, lo que ha sido un tema importante durante las últimas décadas. El estudio de estas regiones proporciona información sobre la interacción entre nucleones y ayuda a comprender cómo aparece su comportamiento colectivo. Una de las regiones más interesantes es la cercana al núcleo ^{132}Sn, ya que se trata de un núcleo doblemente mágico con Z=50 y N=82.

Esta tesis se divide en dos secciones: el desarrollo de un circuito de lectura inmune a campos magnéticos basado en sensores SiPM para experimentos de coincidencias ultrarrápidas y el análisis de datos de los núcleos ^{130}I (Z=53, N=77) y ^{130}Sn (Z=50, N=80) en la región del ^{132}Sn mediante medidas de espectroscopia gamma y coincidencias ultrarrápidas.

La primera parte de esta tesis se centra en el desarrollo de un circuito de lectura inmune a campos magnéticos basado en sensores SiPM. Esto forma parte del programa ENDURANCE del Instituto Laue Langevin (ILL), en el que uno de los instrumentos (FIPPS) se acoplará a un espectrómetro de masas basado en campos magnéticos, que hace que la elección del PMT no sea óptima para experimentos de coincidencias ultrarrápidas. Se ha desarrollado una matriz de SiPM porque su inmunidad a los campos magnéticos los hacen ideales para esta aplicación. Los sensores elegidos son producidos por Onsemi y se han desarrollado dos matrices empleando dos modelos diferentes: MicroFJ-30035-TSV y MicroFJ-60035-TSV. La selección de esta marca se hace exclusivamente basándose en las dos señales de salida particulares a todos los sensores Onsemi: la estándar y la rápida. La lectura trata de forma diferente cada tipo de señal procedente de los sensores; sumando todas las salidas estándar para obtener la mejor respuesta energética posible, mientras que las salidas rápidas se han agrupado y solo las señales más rápidas de cada grupo contribuyen a la señal de salida final.

Se ha realizado una caracterización completa de ambas matrices de SiPM y se han comparado con un PMT R9779, que es el elegido para experimentos de coincidencias ultrarrápidas debido a su rápida respuesta temporal combinada con una buena resolución energética. Los resultados obtenidos muestran unos valores para la resolución energética muy competitivos de 3.7% y 3.9% para las matrices,

30035-TSV y 60035-TSV respectivamente, frente a los 4.0% del PMT, manteniendo una buena linealidad. Sin embargo, la resolución temporal de ambas matrices, 239 y 275 ps de resolución temporal intrínseca a energías de ^{60}Co, sigue estando lejos de los 110 ps de los PMT. Esto, combinado con la evolución de los SiPMs y las futuras mejoras en la lectura, convierte al conjunto basado en SiPM en una futura alternativa al PMT.

La última sección de esta tesis se centra en el estudio de dos núcleos dentro de la región ^{132}Sn: ^{130}I (Z=53, N=77) y ^{130}Sn (Z=50, N=80). Los multipletes protón-neutrón esperados en ^{130}I surgen de las configuraciones del modelo de capas en la región, con neutrones por debajo de N=82 y protones por encima de Z=50. Su origen es el acoplamiento de protones y neutrones en el modelo de capas. Su origen es el acoplamiento de las configuraciones $\pi g_{7/2}$ y $\pi d_{5/2}$ del protón con neutrones que ocupan las órbitas de partícula independiente $\nu s_{1/2}$, $\nu d_{3/2}$ y $\nu h_{11/2}$. Por otro lado, los acoplamientos neutrón-neutrón esperados en ^{130}Sn surgen de las configuraciones del modelo de capas, con dos agujeros de neutrones por debajo del hueco N=82.

Ambos núcleos se han investigado mediante métodos de coincidencias ultrarrápidas. Se trata de un método de coincidencia electrónica que emplea detectores de centelleo rápidos para extraer los tiempos de vida de los estados excitados. Los tiempos de vida son un observable clave para entender el comportamiento de los núcleos exóticos, ya que permite acceder a las probabilidades de transición reducidas, que son cantidades importantes para el estudio de las configuraciones de una sola partícula, la colectividad nuclear y posibilitan la comprobación de los modelos teóricos.

Los núcleos estudiados se poblaron en dos montajes experimentales diferentes. El núcleo ^{130}I se pobló en la reacción ^{129}I(n,γ)^{130}I y el experimento tuvo lugar en el instrumento FIPPS del Instituto Laue Langevin. El montaje experimental consistió en un conjunto de 8 detectores HPGe acoplados a un dispositivo auxiliar formado por 16 detectores $LaBr_3$(Ce). Con el fin de reducir los módulos analógicos necesarios para el método de coincidencias ultrarrápidas, se instaló una configuración de multiplexado tanto para la señal start como para la señal stop.

El ^{130}Sn se pobló en la desintegración beta de los estados isoméricos del ^{130}In en la campaña experimental IS610. El experimento tuvo lugar en la estación de decaimiento ISOLDE (IDS) de la instalación ISOLDE en el CERN. Aprovechando la selectividad de isómeros de la estación RILIS, se produjeron los tres estados isoméricos del ^{130}In y se estudió su desintegración beta. El sistema IDS consiste en 4 detectores HPGe para espectroscopia gamma de alta resolución acoplados a un sistema de coincidencias, que consiste en un detector beta y dos detectores $LaBr_3$(Ce) con el sistema analógico estándar para obtener coincidencias que permitan la extracción de tiempos de vida.

Los resultados en ^{130}I no aportan nuevas transiciones de rayos γ o niveles excitados respecto al experimento realizado previamente en los años 80, por lo que el tiempo de vida de los estados excitados ha sido el objeto del análisis. Sin embargo, se han obtenido varios tiempos de vida nuevos mediante coincidencias triples entre el HPGe y dos detectores de $LaBr_3$(Ce). El tiempo de vida se extrae entre las co-

incidencias $LaBr_3$(Ce)-$LaBr_3$(Ce) añadiendo una tercera coincidencia en el detector HPGe por selectividad de rama, ya que el esquema de niveles de ^{130}I es complejo. Tres nuevas vidas medias se han obtenido en el análisis para este núcleo para los niveles $(3,4)^-$, $(4)^-$ y $(5)^-$, con valores de 24(9), 129(6) y 45(13) ps respectivamente.

Se ha estudiado la estructura nuclear del ^{130}Sn y se ha ampliado el esquema de niveles con 8 nuevos niveles excitados y 14 nuevas transiciones de rayos gamma añadidas a la estructura conocida para cada desintegración. Se han medido los tiempos de vida de los estados del ^{130}In que se desintegran β mediante desintegraciones γ con los detectores de HPGe y los resultados concuerdan con los valores medidos previamente. Se han revisado los valores de las vidas medias para los estados 10^+ y 5^-, obteniéndose valores de $T_{1/2}$=1,48(6) μs y $T_{1/2}$=50,7(2) ns que concuerdan bien con las medidas previas. Por último, se han obtenido dos nuevas vidas medias a partir de esta desintegración, siendo el estado 8^+ poblado en el decaimiento β del ^{130m1}In con un valor de $T_{1/2}$=321(10) ps y el estado 6^+ con un valor de $T_{1/2}$=68(3) ps.

Contents

1 Introduction

It would be difficult to understand the rapid advancement of nuclear structure research in recent decades without several elements that have contributed to scientific progress. One of them is undoubtedly the augmented capacity of production of the so-called exotic nuclei, those far off stability, which is taking us to extremes that were unsuspected until very recently, and brings us ever closer to nuclides that were once only possible to reach in the explosive astrophysical processes of nucleosynthesis. The production of rare nuclear species at large-scale facilities is common place nowadays in research. The reach to more and more exotic nuclei has been steadily growing, and the spectacular advancement has made it possible to for example tackle ^{78}Ni and to expand spectroscopy in the neutron-rich region south-west of ^{208}Pb, to give just a couple of examples. Complementary techniques such as fission have also been taken to the limit by exploring different fissile targets, incident particles and bombarding energies.

At the same time, the instrumentation and detection techniques that are used to obtain information on many aspects of the produced exotic nuclei keeps progressing. Developments in spectroscopic detectors, reaction techniques and production mechanisms flourish and take advantage of new technologies and ideas. One of the aspects where instrumentation in nuclear physics has been improved relates to high-efficiency gamma-spectroscopy setups based on HPGe arrays. The combination with other complementary detector systems opens up new possibilities for gamma spectroscopy and nuclear structure research. Based on the successful EXILL gamma spectrometer campaign at the Institut Max Laue Langevin (ILL) [Bla+13; Jen+17], work on a permanent HPGe array was started as part of the laboratory ENDURANCE program. The idea was to develop a Fission Product Prompt γ-ray Spectrometer (FIPPS) [Mic+18] consisting of a high-resolution HPGe array coupled to a recoil spectrometer based on a gas-filled magnet. Among the main physics aims were the investigation of nuclear structure of neutron-rich nuclei and the study of the fission process itself.

The measurement of excited level lifetimes in neutron-rich nuclei has proven to be a powerful tool for the understanding of structure of exotic nuclei. It can be applied to fission using fast-timing spectroscopy, as achieved during the EXILL-FATIMA campaign [Rég+14]. The technique takes advantage of fast scintillator crystals with sufficient energy resolution, such as $LaBr_3$(Ce) or $CeBr_3$, coupled to high-performance photosensors, in order to build fast detectors that are used to electronically measure time differences between gamma photons. Customized fast photomultiplier tubes have been traditionally used as photosensors, but this solution will not be possible at FIPPS due to the presence of the magnetic spectrometer.

One of the objectives of this thesis is the development of a magnetically compatible crystal readout system based on Silicon PhotoMultipliers (SiPMs), which have been commercially available for the last decade. Viable solutions for large area SiPM arrays for γ-ray spectroscopy applications did not exist until very recently [Mih+20] and the proposal in this thesis work is to explore fast-timing capabilities of this type

of systems, since there is still ample room for improvement. In the first part of the manuscript, the investigation of $LaBr_3(Ce)$ crystals optimized for fast-timing spectroscopy coupled to different SiPM arrays and a magnetic field compatible readout is described.

The second aspect addressed in this thesis relates to γ spectroscopy making use of $LaBr_3(Ce)$ detectors for fast-timing measurements. Pilot experiments have been performed at FIPPS in its initial phase, without the coupling of the magnetic spectrometer that will be included at a later stage. One of the nuclei whose complete gamma-spectroscopy study was proposed to profit from the high capabilities of the FIPPS Germanium array and a fast-timing array of $LaBr_3(Ce)$ detectors is ^{130}I.

The structure of this doubly odd-nucleus, with Z=53 and N=77, close to the line of stability in the region of the ^{132}Sn double shell-closure, may provide information on the coupling of the proton and neutron single particle configurations and on the evolution of proton orbitals above Z=50 when approaching N=82. It is also expected that some additional information can be gained about the presence of collective effects in this (in principle) spherical nucleus, and their general role off odd-odd nuclides in the region. The collective nature is best revealed by the presence of enhanced quadrupole E2 transitions, which can be derived from the measurement of lifetimes and decay branches.

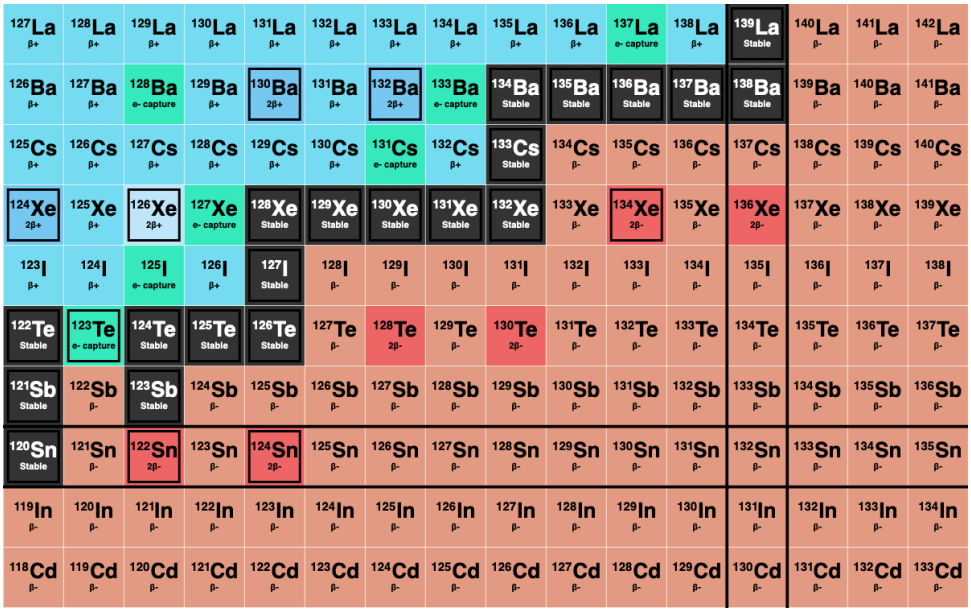

Figure 1: **Close up on region of interest in the chart of nuclides, figure taken from the *Colourful Nuclide Chart* [Cha].**

The way to populate the excited structure of ^{130}I is a neutron capture reaction on an iodine target enriched in ^{129}I, a radioactive long-lived isotope of iodine with

$T_{1/2}$=16.14 My. The nature of this target and the fact that the main mechanisms populating ^{130}I are the (n,γ) and (d,p) reactions, make the knowledge about ^{130}I limited, in spite of the comprehensive work by Shakarov et al. [Sak+89], where gamma and conversion electron spectroscopy, together with a coincidence study using Ge(Li) detectors, was performed using the (n,γ) reaction. A complementary study with (d,p) is also reported in [Sak+89]. Lifetimes of low-lying states in the 100 of ns range were measured using the Ge detectors, and limits were proposed for other states.

In this case, we have an odd-odd nucleus with a few particles above Z=50 and several holes in the N=82 neutron shell. The expected proton-neutron multiplets in ^{130}I arise from the shell-model configurations in the region, with neutrons below N=82 and protons above the Z=50 gap. Their origin is the coupling of the proton πg7/2 and πd5/2 configurations with neutrons occupying the νs1/2, νd3/2, and νh11/2 single particle orbits. Identifying them requires a high-resolution spectroscopy measurement with good efficiency. The measurement of lifetimes and decay branches gives information on the nature of the states. Several of the negative-parity and positive-positive parity states in the range from 300 to 700 keV are expected to have measurable lifetimes.

In addition to ^{130}I, the structure of the tin isotope ^{130}Sn has been investigated in this PhD Thesis in the framework of the IS610 experimental collaboration. The experiment was carried out at the ISOLDE Decay Station in the ISOLDE facility at CERN, and was focused on completing the known level scheme as well as measuring excited level lifetimes. We took advantage of the isomeric selection capabilities of RILIS to enhance the ionization of the three known ^{130}In β-decaying isomers to individually study their decay. To construct the level scheme, high-resolution HPGe detectors have been used while the Advanced Time-Delayed $\beta\gamma\gamma(t)$ method [MGM89] was used to measure excited level lifetimes.

The exotic ^{130}Sn lies in the vicinity of the ^{132}Sn (Z=50, N=82) [Ben+20] double shell closure, and therefore it provides an ideal testing ground of the competition of single-particle and collective degrees of freedom in the region of exotic magic numbers in order to understand the evolution of shell structure far from the β-stability line, which is one of the major challenges in modern nuclear structure.

The decay scheme from three isomerically-purified beta-decaying states in ^{130}In has been obtained. In this thesis work, we present an extended level scheme of 130Sn compared to previous works [FHS81] and the measurement of level lifetimes for some of the low-lying states, from which transition probabilities were obtained. The results are compared to nuclei in the region.

The thesis is organized as follows. Chapter 2 describes the fast-timing methods that allow the study of lifetimes of excited states. Chapter 3 focuses on the two SiPM-based detector development, explaining the process behind the readout as well as the characterization for both of the arrays, and a comparison against the

R9779 PMT used in fast-timing experiments. Chapters 4 and 6 focus on each of the experimental set-ups employed to study both of the nuclei under study in this thesis. THE results for ^{130}I and^{130}Sn are presented in Chapters 5 and 7. In Chapter 8 the conclusions and future outlook for this thesis are drawn.

2 Lifetime measurements via fast-timing methods

Nuclear level lifetimes are a key parameter in nuclear structure studies since they grant access to the reduced transition probabilities. A better understanding of nuclear symmetry and collectivity behaviours can be studied with the transition probabilities. Currently, there is a great variety of methods that allow for the study of lifetimes down to the 10 of picoseconds range.

In this thesis we use electronic timing methods to measure lifetimes from the time differences between the population and de-population of excited states. Slow timing measurements have been performed between HPGe (High Purity Germanium) detectors in order to measure long lifetimes ranging from μs up to the ms range. Two types of slow timing have been used in IS610 data, the β-HPGe(γ) coincidence was employed to measure lifetimes in the ns range while HPGe(γ)-HPGe(γ) coincidences has been employed in order to study the ^{130}In isomer half-lifes, which go up to the ms range.

In order to access lifetimes from several ns down to the ps range, delayed coincidence methods using fast $LaBr_3$ scintillators have been employed. Such methods are the Advanced Time Delayed $\beta\gamma\gamma$(t) (ATD) method and the Generalized Centroid Shift (GCD) method. The main principle behind both methods is the measurement of the time difference between the population and de-population of the level under study with fast scintillators, if no need for an extra energy selectivity is needed. The sensitivity of these techniques is directly proportional to the time resolution of the setup used. This chapter reviews both of the fast-timing methods and the reduced transition probabilities.

2.1 The Advanced Time delayed $\beta\gamma\gamma$(t) method

Developed in the 1980s by H. Mach, M. Moszynski and R. Gill [MGM89; MM89] the Advanced Time delayed $\beta\gamma\gamma$(t) method, or ATD method, is an electronic technique that allows the measurement of lifetimes of excited states populated in β decay down to the ps range. Neutron-rich nuclei populated by β decay have large Q_β values, allowing the population of excited levels at high energy following the selection rules.

These levels, once populated, de-excite themselves by γ cascades until reaching the ground state. This behaviour is perfect for fast-timing techniques. This method profits from the $\beta\gamma$ and $\beta\gamma\gamma$ coincidences in order to access lifetimes of the populated excited states after β feeding occurs.

Lifetimes on this method are obtained by measuring the time difference between the arrival of the β particle and the γ-rays that de-excite the level under study. Since the β spectrum is a continuum, energy branch selection resides on the $LaBr_3(Ce)$ scintillators, although an additional HPGe coincidence can be required. $LaBr_3(Ce)$ detectors combine good energy resolution with a fast time response, making them the best choice for this type of experiments. An extra condition may be applied if the scintillator detector can't resolve the desired energy, applying an energy gate on a HPGe detector whose energy resolution is greater than the $LaBr_3$ one.

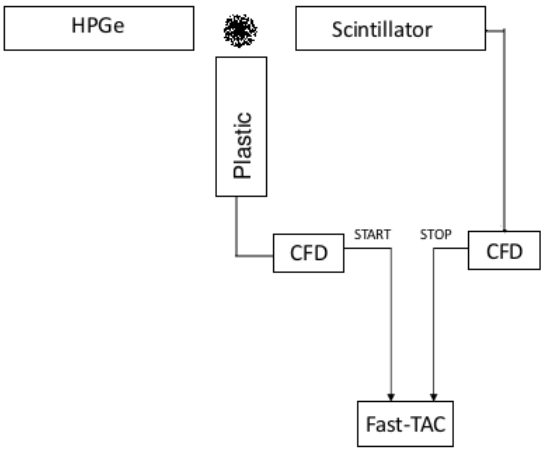

Figure 2: **Simplified standard $\beta\gamma\gamma$(t) electronic setup.** Fast-timing measurements obtain the lifetimes of excited levels studying the time difference between the populating and the de-exciting radiation of such level. On beta decay this difference is measured using fast β and scintillator detectors. HPGe detectors are used for branch selectivity

The electronic setup to measure the time difference is displayed in figure 2. Two signals are taken from each detector to the CFD module. The time difference between the arrival of two signals is converted into an output signal with an amplitude proportional to their time difference by three ORTEC 567 Time to Amplitude Converter (TAC) 200 MHz modules. The time spectra obtained by the TAC is given when using the β signal as the start and the γ signal as the stop (or vice-versa) and has a square shape, which height is proportional to the time difference between signals. The time distribution obtained can be expressed as:

$$F(t_j) = N \int_{t_0}^{+\infty} P(t_j - t) f(t - t_0) dt \tag{1}$$

Where N is the total number of counts in the time distribution, $f(t)$ is an expo-

nential decay function like $f(t) = e^{\lambda t}$, where λ is the time constant of the level under study. The last term on the equation, $\mathrm{P(t}_j)$, is the system response contribution and it is the origin of most of the uncertainties. This can be experimentally verified to have a quasi-gaussian form whose centroid varies with the energy of the detected particle. This dependency of the centroid with the energy has to be studied and is known as time walk and it's of vital importance for centroid shift measurements.

At last, the lifetime of the desired level can be extracted using the ADT by two ways: the convolution technique and the centroid shift method. The main difference between these two methods is the time range and they will be explained in the following sections.

2.1.1 The Convolution technique

When the lifetime of the level is long enough, it will appear as a slope on the delayed part of the time spectra. The lifetime can be measured by fitting the slope to an exponential function convoluted by the prompt response. In order to access the lifetime it has to be unfolded by an iterative procedure. Analytically, the time distribution can be described as:

$$F(t_j) = N \int_{t_A}^{+\infty} e^{-\delta(t_j - t)^2} e^{\lambda t - A} dt \tag{2}$$

where the $\mathrm{e}^{\lambda t}$ term comes from the lifetime of the level as previously stated, the $\mathrm{e}^{-\delta(t_j - t)^2}$ term is the system prompt response function given at a certain energy, δ is a parameter determining the width of the Gaussian prompt distribution and A is the centroid of the Gaussian.

Figure 3 panel (b) shows an example of how the time distribution appears as a slope. In red appears the time distribution for a prompt transition, where this method cannot be applied since the lifetime is too short to appear as a slope. The distribution in blue corresponds to a long-lived level, whose meanlife can be obtained by measuring the slope of the distribution. On this case, the blue spectrum is the convolution of a semi-gaussian function with an exponential decay. In order to obtain the meanlife, the fit of the slope has to be done outside of the influence of the prompt.

2.1.2 The Centroid shift method

The centroid shift method is employed when the lifetime under study cannot be measured via the slope method. This occurs when the lifetime does not show as a slope on the delayed part of the spectra, since it's shorter than the quasi-Gaussian component. Lifetimes with these values can be determined if the prompt response function can be approximated by a Gaussian [MGM89; MM89]. The centroid C(F) is the first moment of the statistical convoluted time distribution:

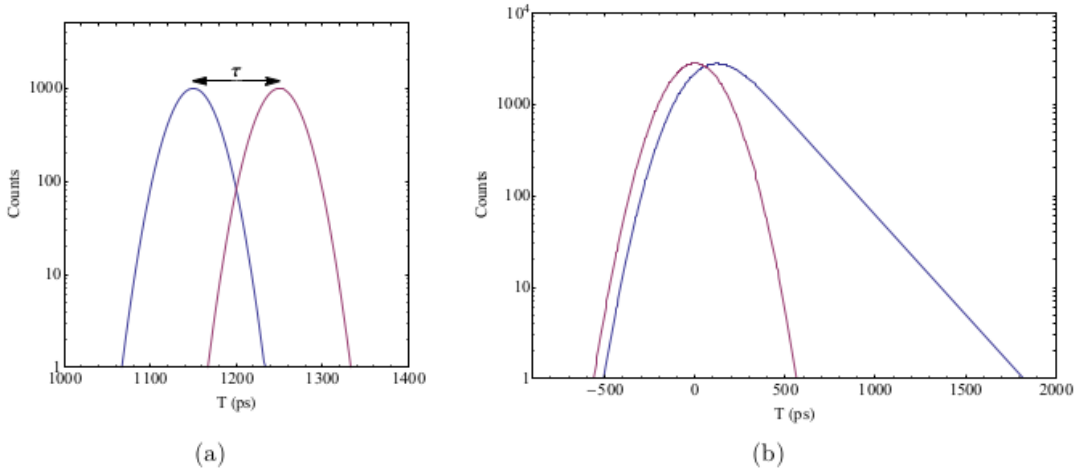

Figure 3: **Advanced Time delayed $\beta\gamma\gamma$(t) lifetime measurements.** Centroid shift method is illustrated in figure (a), where the lifetime is given by the difference between the time distribution (blue) and the prompt reference (red). Figure (b) shows the convolution technique, where the lifetime is obtained from the slope of the time distribution. Image obtained from [VPa].

$$C^D = \frac{\int_{-\infty}^{+\infty} tF(t)dt}{\int_{-\infty}^{+\infty} F(t)dt} \tag{3}$$

with F(t) of equation 1. The centroid of the prompt distribution will only depend on the energy, so the lifetime can be extracted from the shift between the centroids from the prompt time distribution and the convoluted time distribution:

$$\tau = C^D(E_{feeder}, E_{decay}) - C^P(E_{feeder}, E_{decay}) \tag{4}$$

where C^P is the prompt centroid and C^D is the centroid of the time distribution. In order to perform this type of measurements the prompt response function needs to be calibrated as well as the compton curve. This method is more effective when working with simple level schemes.

2.2 The Generalized Centroid Difference method

The Generalized Centroid Difference method (GCD) was specially develop for large fast-timing arrays such as the Fission Product Prompt γ-spectrometer (FIPPS) installed at the Institut Laue Langevin. This instrument can be coupled to an

auxiliary device made o 16 $LaBr_3$(Ce) scintillators allowing the study of lifetimes down to the ps range.

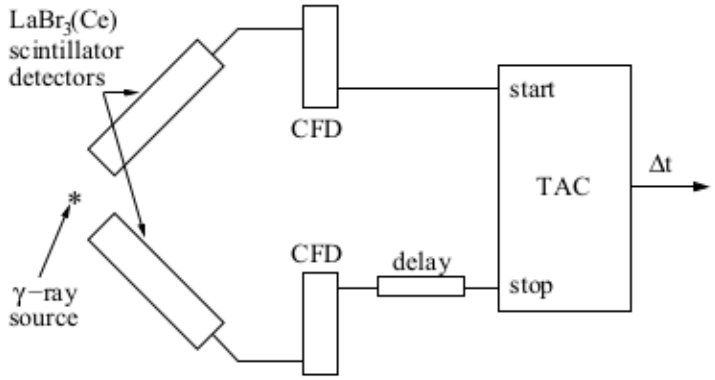

Figure 4: **Simplified standard $\gamma\gamma$(t) electronic setup.** Standard electronic setup γ-γ fast-timing circuit. Branch selection comes by gating HPGe detectors (not displayed on the image). Image taken from [Rég+15]

Lifetime measurements come from the time difference between the radiation populating the excited level and the radiation decaying from it. This time difference is measured with two $LaBr_3$(Ce) whose fast time response and good energy resolution make them the optimal choice for the technique. An extra coincidence can be placed in the HPGe detector which does not play a role on the timing measurement, rather it is used for the selection of the decaying branch. The lifetime of the excited state will be:

$$\tau = C^D(E_{feeder}, E_{decay}) - C^P(E_{feeder}, E_{decay}) \tag{5}$$

where C^P is the prompt centroid and C^D is the centroid of the time distribution, an example can be seen in Figure 5 . Although this method is focused on fast-timing arrays, let's consider first an experimental setup with only two scintillator detectors (a start and a stop) studying the same source. Two time distributions on the offline analysis can be distinguished: the delayed and the anti-delayed. The delayed time distribution is obtained when the γ-ray that feeds the level (also called "feeder") acts as the start in the measurement while the stop is set to the decay γ -ray (also known as "decay"). The centroid of the obtained distribution is "delayed" (or shifted to the right) by the lifetime of the level. The other distribution, the anti-delayed, is the result of selecting the γ-ray that de-excites the level (decay) as the start in the TAC and the feeding γ-ray as the stop. This time distribution is also shifted by the lifetime but on this case to the left (or "anti-delayed"), an example of both time distributions is displayed in Figure 5.

If one assumes no background contribution, the time shift between both distributions corresponds to:

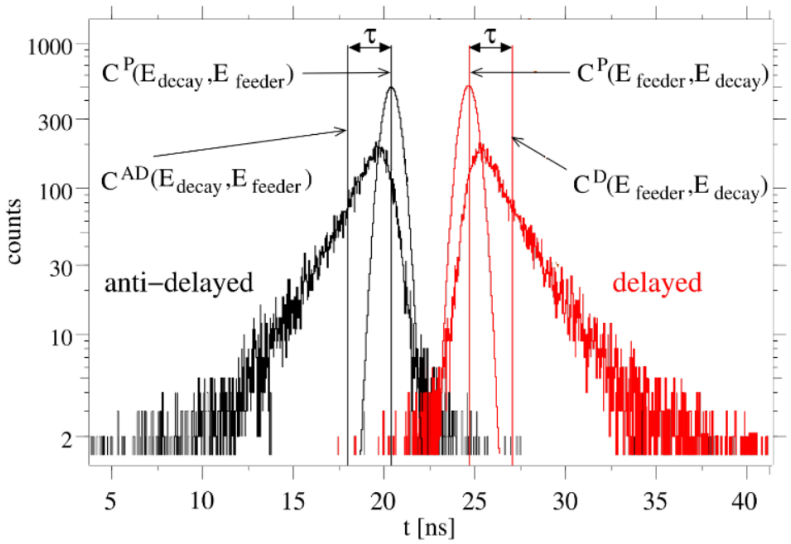

Figure 5: **Example of delayed and anti-delayed time distributions.** The GCD obtains the lifetime under study from the shift between the delayed (red) and anti-delayed (black) time distributions. Image taken from [Rég+16].

$$\Delta C(D, AD) = \Delta PRD(D, AD) + 2\tau \tag{6}$$

where the PRD stands for Prompt Response Difference and describes the γ-γ time walk response of the detector timing system. The PRD curve studies the energy-dependent system response of γ-rays that have deposited their full energy into the scintillators. The prompt response difference is also mirror symmetric, like the centroid shift method, so when the start-stop conditions are inverted:

$$\Delta C(E_\gamma)_{dec} = -\Delta C(-\Delta E_\gamma)_{feed} \quad ; \quad PRD(\Delta E_\gamma)_{dec} = -PRD(-\Delta E_\gamma)_{feed} \tag{7}$$

and of course, for only two detectors two detectors it can happen:

$$PRD(\Delta E_\gamma = 0) = 0 \quad \Rightarrow \quad |\Delta C(-\Delta E_\gamma = 0)| = 2\tau \tag{8}$$

The method described by Equations 6 through 9 is known as the Mirror-Symetric Centroid Difference (MSCD) [Rég+10] and is a method employed for fast-timing measurements for a two detector set up. This method cancels the systematic errors product of electronic drifts. One of the major challenges when using this method is the procedure to obtain the PRD(E_γ) curve for a given system. In order to study the dependence between the time response difference and the energy, different

radioactive sources are employed in order to cover a wide energy range. By using a fixed energy reference, the energy dependence of the PRD is rather smooth. By making PRD($E_{reference}$)=0, any given γ-γ transition will have the following time response difference:

$$PRD(E_{feeder}, E_{decay}) = PRD(E_{feeder}) - PRD(E_{decay}) \tag{9}$$

When the previous method is translated into fast-timing arrays, the procedure would need to look at every combination of fast detectors on the timing set up, which is not optimal. For this reason, the Generalized Centroid Difference (GCD) was developed [Rég+13; Rég+15] in order to provide a simplification of fast-timing analysis for large timing arrays. This method avoids the determination of the Full Energy Peak (FEP) walk time response to be determined for every detector on the timing array. This method reduces the complexity of the scheme into a two detector system by imposing all the detector-detector combinations. Analogous to the MSCD method, the mean life of a given excited state is given by the equation:

$$\Delta C_{FEP} = \Delta PRD(E_{feeder}, E_{decay}) + 2\tau \tag{10}$$

One can note that the construction of the (mean) PRD curve is important, since it constitutes the only correction for the lifetime determination. The PRD is determined by background free events, so the correction due to this type of events is performed within the centroid difference using:

$$\Delta C_{FEP} = \Delta C_{Exp.} + \frac{\Delta C_{Exp.} - \Delta C_{Compton}}{p/b} \tag{11}$$

where $\Delta C_{Exp.}$ is the experimental centroid difference, p/b is the peak to background ratio on the coincidence spectra and $\Delta C_{Compton}$ is the time response of the Compton background at the corresponding energy. In order to understand the latter one, a ^{60}Co source is often used to study the Compton events as a calibration of the detector time walk for the region between 250 keV up to 1.17 MeV, following the continuum of the 1173 keVγ-ray in the decay. The Compton response curve provides the system response to the γ-ray that have deposited part of their energy through Compton scattering. This curve is important to evaluate the contribution of Compton events to the time distribution under study and needs to be implemented for different energies

2.3 Transition probabilities and Weisskopf estimates

Once lifetime measurements are obtained with the previous mentioned methods, one can obtain the reduced transition probabilities which provide unique information

about the nucleus under study such as ground state deformation and collective deformations. This reduced transition probabilities for a γ transition is given by [BM75]:

$$B(X\lambda; J_i \to J_f) = \frac{1}{2J_i + 1} \langle J_f M_f | H(X\lambda) | J_i M_i \rangle^2 \tag{12}$$

where J_i and J_f are the angular momentum of the initial and final state after the transition has taken place. If the levels involved do not possess a confirmed spin and parity assignment, the transition with a multipole λ is given by:

$$B(X\lambda; J_i \to J_f) = \frac{\lambda[2\lambda + 1]]^2 \hbar}{8\pi(\lambda + 1)} \left(\frac{c\hbar}{E_\gamma} \right)^{2\lambda+1} \tau_\gamma^{-1} \tag{13}$$

The energy transition on the formula comes as E_γ. The B(Xλ, $J_i \to J_f$) coefficient is a dimensional estimate, so the units for electric or magnetic transitions are different. The first two order of these coefficients for each of the transition types are displayed in Table 1.

X λ	B(X$_\lambda$)		B$_{Weisskopf}$(X$_\lambda$)	
E1	6.288x10^{-16}E$_\gamma^{-3}$ τ_γ^{-1}	e^{2}fm^2	0.06446x A$^{2/3}$	e^{2}fm^2
E2	8.161x10^{-10}E$_\gamma^{-5}$ τ_γ^{-1}	e^{2}fm^4	0.05940x A$^{4/3}$	e^{2}fm^4
M1	5.687x10^{-14}E$_\gamma^{-3}$ τ_γ^{-1}	μ_N^2	1.7905	μ_N^2
M2	7.381x10^{-8}E$_\gamma^{-5}$ τ_γ^{-1}	μ_N^2fm^2	1.6501x $A^{2/3}$	μ_N^2

Table 1: **Transition probabilities for the first two types of transition.** Transition probabilities and Weisskopf estimates for the first 2 multipolarities. Data taken from [Kra91]

The comparison between the transition probabilities obtained theoretically and experimentally is a good test of theoretical models. These values can be strongly influenced by the structure of the initial and the final states, which can be explained due to collective behaviours or transition forbidden by the selection rules.

The Weisskopf estimates were introduced to compare experimental and theoretical transition probabilities. These are single particle estimates that consider a constant radial wave-function (given by R $\approx$A$^{1/3}$) has caused the transition without affecting other particles. These estimates are given by the equations:

$$B_{Weisskopf}(E\lambda) = \frac{1}{4\pi} \left(\frac{3}{\lambda + 3} \right)^2 (1.2)^{2\lambda} A^{\frac{2\lambda}{3}} \qquad e^2 fm^{2\lambda} \tag{14}$$

$$B_{Weisskopf}(E\lambda) = \frac{10}{\pi} \left(\frac{3}{\lambda + 3} \right)^2 (1.2)^{2\lambda-2} A^{\frac{2\lambda-2}{3}} \qquad \mu_N^2 fm^{2\lambda-2} \tag{15}$$

With these estimates, one can study the collectivity of a transition making a comparison between transition probabilities and the Weisskopf estimates. If the transition probability is greater than the Weisskopf estimate, this would imply that many nucleons are acting together in a collective manner. Usually E2 transition related to collectivity due to rotations of deformed nucleus or quadrupole vibration. In most cases, it competes with the M1 transitions which are much slower and do not exceed the 1 W.u..

3 Silicon Photomultiplier array based read-out for $LaBr_3$ (Ce) in fast-timing studies at FIPPS

Many experimental nuclear physics studies take advantage of highly efficient gamma spectroscopy setups based on HPGe arrays. The combination with complementary/ancillary detector systems opens up new possibilities for gamma spectroscopy and nuclear structure research. Based on the successful EXILL gamma spectrometer campaign at the Institut Laue Langevin (ILL), work on a permanent HPGe array was started as part of the laboratory ENDURANCE program. The idea was to develop a Fission Product Prompt γ-ray Spectrometer (FIPPS) [Mic+18] consisting on a high-resolution HPGe array coupled to a recoil spectrometer based on a gas-filled magnet. Among the main physics aims were the investigation of nuclear structure of neutron-rich nuclei and the study of the fission process itself.

The measurement of excited level lifetimes in neutron-rich nuclei has proven to be a powerful tool for the understanding of structure of exotic nuclei. It can be applied to fission using fast-timing spectroscopy, as achieved during the EXILL-FATIMA campaign [Rég+14]. The technique takes advantage of fast scintillator crystals with sufficient energy resolution, such as $LaBr_3$(Ce) or $CeBr_3$, coupled to high-performance photosensors, in order to build fast detectors that are used to electronically measure time differences between gamma photons. Customized fast photomultiplier tubes have been traditionally used as photosensors, but since they are offset by magnetic fields it will not be implemented at FIPPS due to the presence of the magnetic spectrometer.

A magnetically compatible crystal readout system is currently under development based on Silicon PhotoMultipliers (SiPMs), which have been commercially available for the last decade. Although viable solutions for large area SiPM arrays for γ-ray spectroscopy applications exist [Mih+20] the fast-timing capabilities of this type of systems has still room for improvement. In this work we present the investigation of $LaBr_3$(Ce)) crystals optimized for fast-timing spectroscopy coupled to two different SiPM arrays and a magnetic field compatible readout. One of the arrays is based on a MicroFJ 60035 TSV by Onsemi, and the other one is a commercially-available MicroFJ 30035 array from the same brand. The performance

of the detector assemblies with respect to time response and energy resolution and a comparison to a similar $LaBr_3(Ce)$ crystal coupled to a PMT will be provided.

3.1 Motivation: From EXILL to FIPPS

Thermal-induced fission, which is possible at Institut Laue Langevin (ILL), provides important data for nuclear structure studies and nuclear reactor physics. The design of future Generation IV reactors requires information on how nuclear waste evolves during the fission process. For this reason, modelling the fission process requires the understanding of several observables in such type of reactions to be measured. In addition, the study of neutron-rich nuclei far from the stability line has been one of the great challenges of the last decades. With a better comprehension of them, scientists aim to understand how nuclear structure evolves far from the stability line as well as the creation of heavy elements in the astrophysical rapid process. One powerful approach to study excited states on neutron rich nuclei is γ-ray spectroscopy of fission products. With the extracted information from these nuclei, the nuclear models can be tested. Fission can be induced in actinide targets with thermal or cold neutrons. Neutron rich fragments from the neutron induced fission will be produced following the fission reaction. Out of all the fissile actinide targets available, ^{235}U and ^{245}Pu remain the most interesting. As can be seen from Figure 6 (left) ^{235}U and ^{241}Pu targets give access to large amounts of nuclei ranging from A=75 up to A=165, making it possible to study nuclei such as ^{76}Ni and ^{132}Sn which are of great interest to study variation on nuclear potential parameters close to the exotic "magic numbers". Furthermore, Figure 6 compares the mass distribution of ^{252}Cf and ^{248}Cm which are widely used targets to study nuclei on the mass range A=85-160 populated in spontaneous fission.

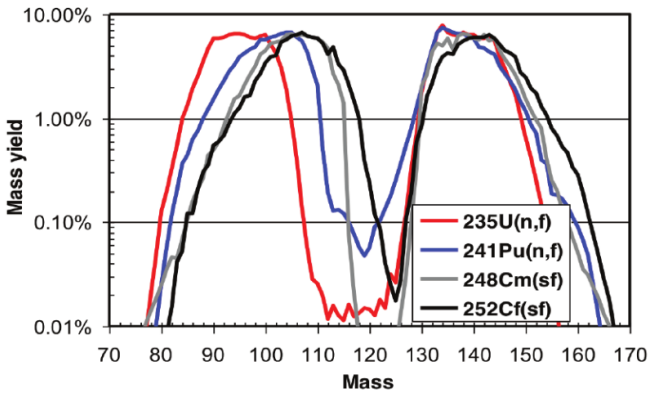

Figure 6: Mass distribution following spontaneous fission of ^{252}Cf (grey) and ^{248}Cm (black), and the neutron induced fission of ^{235}U (red) and ^{245}Pu (blue), image taken from [Mut17].

In 2012, a nuclear spectroscopy campaign was launched at ILL. This campaign,

by the name of EXILL (EXogam at ILL) [Jol+15], combined one of the most intense cold neutrons source available with a high efficiency germanium array (EXOGAM) coupled to an ancillary device made of 16 $LaBr_3$(Ce) detectors [Jen+17; Bla+13], a schematic view of which can be seen in Figure 7. The campaign lasted 2 reactor cycles, measuring a total of 24 targets, which included ^{235}U and ^{245}Pu. The spectroscopy of very neutron-rich isotopes, the result of the fission of ^{235}U and ^{245}Pu, was carried out via γ-γ and γ-γ-γ coincidences. After a successful campaign [Rég+14; Bla+15; Cie+16], EXILL proved the potential of (n,γ) and (n,f) reactions to study nuclear structure on this type of experiments. Isotope selection was based on the use of the above-mentioned triple coincidences as well as partially known level schemes. Based on the experience obtained during this campaign, ILL started to develop a new instrument combining an EXILL-like germanium array with a recoil spectrometer based on a gas-filled magnet [Pau+89] by the name of FIPPS (Fission Product Prompt γ-ray Spectrometer) [Mic+18]. FIPPS is one of the 7 instruments on the modernization programme called "ENDURANCE", currently under progress at ILL. This instrument, when finished, will combine a collimated neutron beam with a HPGe array, a gas filled magnet and auxiliary detectors. The gas filled magnet will ensure sufficient mass resolving power on this type of experiments, since mass and kinetic energy are key factors for the identification of fission fragments.

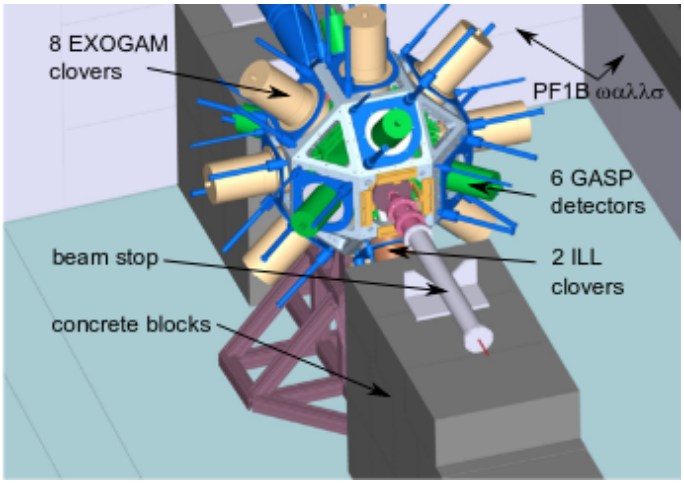

Figure 7: Schematic view of the EXILL set up in the PF1B beam line during the experimental campaign, image taken from [Jen+17].

The Fission Product Prompt γ-ray Spectrometer (FIPPS), like most instruments in the ENDURANCE programme, is scheduled in 3 phases. Phase 1, finished in 2016, focused on the creation of a halo-free pencil neutron beam incident on a target surrounded by a HPGe array [Mic+18], as seen in Figure 8, being a similar setup as the one used in the EXILL campaign but allocated on a different neutron guide (H22 instead of the PF1B). This instrument has been operational since 2017 and is currently being used for (n,γ) experiments. FIPPS is made of 8 HPGe detectors, but it has the capability to be coupled to others such as extra HPGe detectors (as

can be seen in Figure 8 (right)) or $LaBr_3(Ce)$ to mention a few, allowing FIPPS to perform a variety of experiments that suit the needs of different scientific proposals submitted to ILL. Starting its second phase of development in 2018, the goal is to complement the current HPGe array with a recoil spectrometer based on a gas-filled magnet [Kim+20; Che+16]. This upgrade will allow a better study of the fission mechanism and nuclear structure of neutron-rich nuclei by allowing fission product tagging for γ spectroscopy measurements.

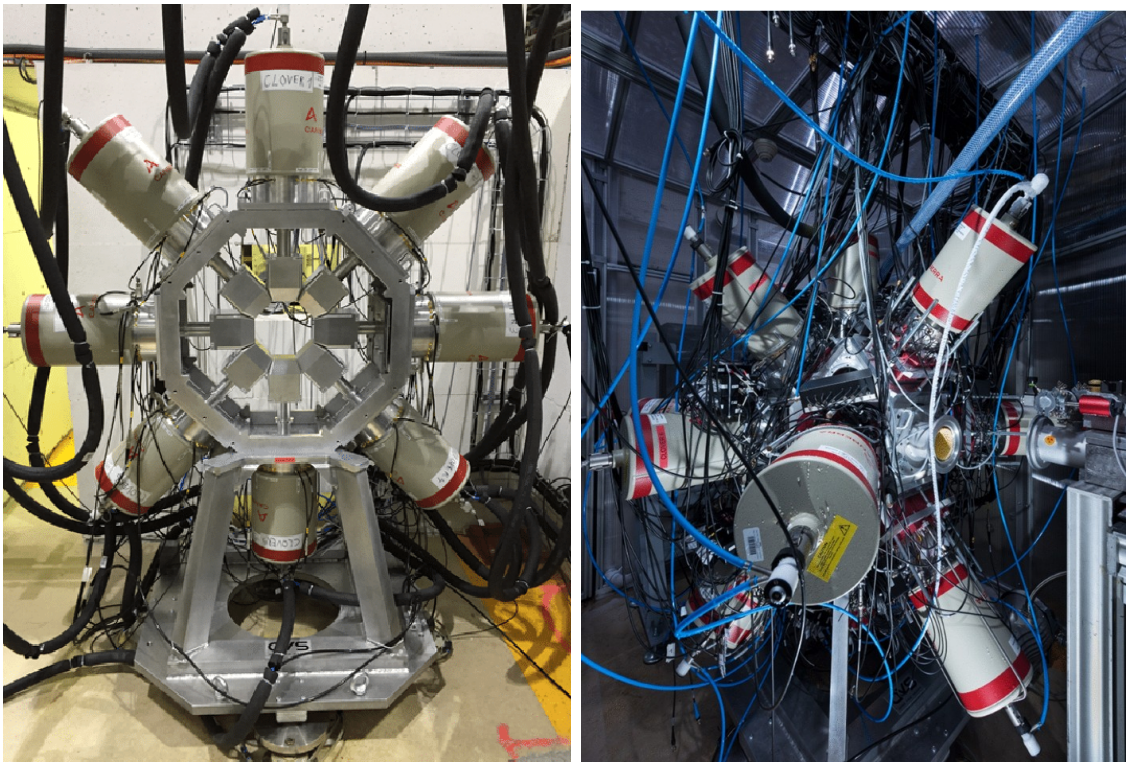

Figure 8: **Left:** FIPPS phase 1 initial set up: 8 HPGe clovers surrounding target position, image taken from [Mic+18]. **Right:** FIPPS, during an experimental campaign, coupled with additional HPGe clovers from the IFIN-HH collaboration, image taken from [Bla+13].

One of the proposed techniques to study the fission product fragments is the Advanced Time-Delayed technique γ-γ coincidence technique, or ultra-fast timing spectroscopy. This is an electronic coincidence method that allows for the measurement of lifetimes down to the tens of picoseconds range, by the direct measurement of the time difference between radiation populating a given level and the de-exciting radiation [MGM89; MM89; MF14]. The technique takes advantage of fast, high performing scintillators for gamma detection. Currently, the most used detectors are $LaBr_3(Ce)$ crystals coupled to PMT (PhotoMultiplier Tube), this choice will not be optimal for future phases of the FIPPS setup since the presence of a magnetic field will affect the performance of the PMT. For this reason, this part of this thesis has been focused on developing a photo-detection device for $LaBr_3(Ce)$ crystals based

on SiPMs, whose immunity to magnetic fields and similar properties as PMTs make them the logical choice for an eventual replacement.

3.2 The Silicon Photomultiplier: operation principle and characteristics

The use of scintillator detectors is a key component in gamma spectroscopy for nuclear science and applications such as medical imaging. A detector is made by coupling a scintillator crystal to a photodetector. The scintillator crystal absorbs the radiation from the environment (mainly gammas for γ-ray spectroscopy) and emits light of a certain wavelength in return, this is detected by the photodetector which starts the mechanism in order to produce a signal. For this reason, the use of optimal photodetectors for this weak scintillation signals is of paramount importance when performing an experiment. In gamma spectroscopy, the photomulitplier tube (PMT) has become a popular choice in order to detect these signals. This photodetector combines a good quantum detection efficiency (up to 40%), a high gain (that ranges from 10^3 up to 10^8), low dark current and a variety of sizes to suit every different application. Nonetheless, the PMT has also several drawbacks; they are very sensitive to magnetic fields and have a relatively high price (due to the handmade manufacturing process). The first one, sensitivity towards the magnetic fields, is an important factor to take into account as magnetic fields are a great way to tag fission fragments and perform more precise experiments. In the presence of a magnetic field, the PMT (vacuum tube) the trajectories of photoelectrons are affected such that the collection efficiency at the first dynode is a function of the orientation of the PMT relative to the magnetic filed. Furthermore, the trajectories of secondary electrons in the dynode chain are affected as well, having a fluctuation in parameters as the gain or the detection efficiency. For this reason, a suitable replacement needs to be found in order to upgrade experimental setups.

The silicon photomultiplier (SiPM) is a solid-state detector that has similar properties as the PMTs, such as high gain, with the immunity to magnetic fields combined with a low voltage operation (nowadays bellow 100V). For this reason, SiPMs have been regarded as a suitable alternative to the popular PMTs since their development [Ren06]. Currently, SiPMs have started to replace PMTs in several scientific fields, such as high energy physics, astrophysics and medical imaging [And+06; Bil+08; Moe+06] to name a few. For this reason, SiPMs are manufactured by several companies: Hamamatsu Photonics (Japan), ON Semiconductor (previously SensL from Ireland), Broadcom (US)... and can be purchased with a great variety of characteristics suitable for any application; from a single device with a small area 0.18x0.18 mm^2 to larger detection areas such as SiPM arrays with 64 sensors with a surface of 6x6 mm^2.

The SiPM is a common-bias and common output sensor made of APD (Avalanche PhotoDiodes) connected in parallel that work in Geiger mode each with its own quenching resistor (as seen in Figure 9 left). Each photodiode is formed by a silicon

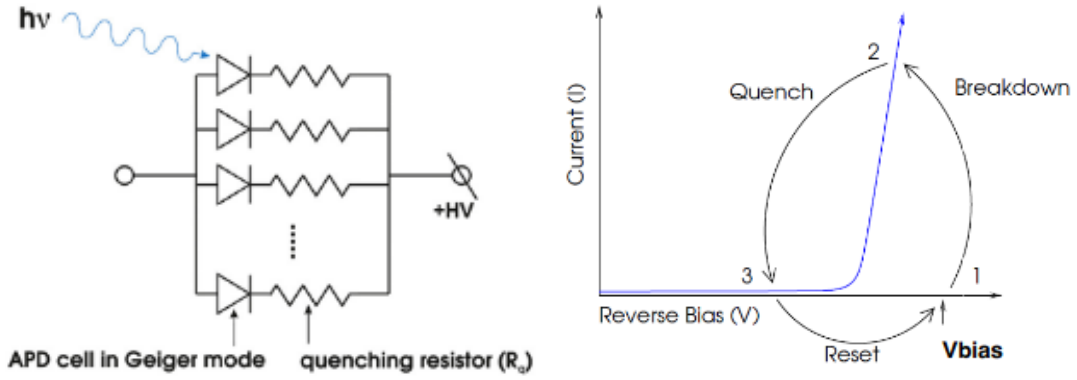

Figure 9: **Left:** Simplified structure of a SiPM detector where the combination of the APD cell and the quenching resistor is defined as a "microcell", image taken from [GMS19]. **Right:** Breakdown, quench and reset of a photodiode working in Geiger mode, image taken from [ONS21a]

p-n (or n-p) junction that creates a depletion region free from carriers to move. When a photon is absorbed by silicon it can transfer its energy to a bound electron. The transferred energy causes the electron to jump the narrow bandgap (1.14 eV), promoting itself from the valence band into the conduction band and creating an electron-hole pair. Applying a reverse bias to the photodiode sets up an electric field across the depletion region that makes the charger carriers to be accelerated towards the anode in case of the electrons and the cathode in case of the holes. If the electric field reaches a certain level, the carriers are more likely to collide with the crystal lattice. The carriers that escape the collision will be carrying sufficient energy and will create new electron-hole pairs. This effect is called as the avalanche multiplication (or chain reaction of ionization). The SiPM works in Geiger mode (Figure 9 right), which means that the sensor enters into the avalanche multiplication process when is reversed-bias above the electrical breakdown voltage (V_{bd}). The avalanche will be self-sustained until one of two things happen: either the voltage supply is lowered below the breakdown voltage or in a more passive way, which consists on the connecting the diode with a quenching resistor in series. Each combination of a photodiode with a quenching resistor is defined as a microcell, and the combined output will correspond to the signal produced by the SiPM. Every detected photon will arrive at a microcell which triggers an avalanche, making the final signal proportional to the number of photodiodes that have been fired when the photon was absorbed.

Individual performance reviews of SiPMs are described in [LFA21; ONS21a; Fir19; Eck+10]. These references test the performance of several SiPM and characterize some of the SiPM characteristics, some of the most important factors are:

- **Power supply.** One of the main advantages of a SiPM is that it operates on a low voltage, usually below 100 V. The bias point at which the electric

field generated in the depletion zone is strong enough to generate the Geiger avalanches is called breakdown voltage (V_{bd}) [Chm+17]. Usually, SiPM operate above the breakdown voltage. The difference between the bias used and the breakdown voltage is referred to as overvoltage (V_{ov} or ΔV, depending on the bibliography). The bias voltage of the sensor is defined by the sum of the breakdown voltage and the overvoltage:

$$V_{bias} = V_{bd} + V_{ov}$$

The sensor's performance is strongly influenced by this parameter which controls characteristics such as the gain and the dark noise of the sensor. The power supply of the SiPM influences several performance parameters, some listed below [Bon+19], and needs to be controlled throughout experimental measurements

- **Temperature dependence.** One of the main drawbacks of this sensor is the sensitivity to temperature shifts [Ram08]. Breakdown voltage (and hence, the gain of the detector) and dark count rate are the two parameters most influenced by temperature changes. With high temperature fluctuations a change in the overvoltage value is observed, which makes the SiPM performance vary. There are two ways to address the performance fluctuations, such as power supply control [Eig+16] or thermal regulation control (an example would be the use of a Peltier device [LFA00].

- **Gain (G).** This parameter is defined as the charge (Q) of the pulse generated from one pixel when it detects one photon, divided by the elemental charge per electron:

$$G = \frac{Q}{q}$$

where "Q" is the charge of a single avalanche in a photodiode, triggered either by the photon or by thermal noise on the silicon, and "q" is the elementary charge $1.602 \cdot 10^{-19}$C. Typically, SiPM gains range from 10^3 up to 10^7 which is in the same order of magnitude as those for PMTs.

- **Fill factor (FF).** this value refers to the percentage of the SiPM that senses the light. As expected, each microcell is isolated for both optical and electrical purposes. Also, space is required to place the quenching resistor and the signal tracks that come out from each photodiode on the microcell. This generates dead space around each microcell and is dependent on its size. As a result, a larger microcell will have a high active surface, which results into a higher PDE and gain but will lower the dynamic range and elongate the recovery time. On the other hand, a smaller microcell, with a lower active surface area, will achieve a lower PDE and gain, but will shorten the recovery time and will have a higher dynamic range.

- **Photon detection efficiency (PDE).** This characteristic is an indication of what percent of the incident photons are detected [Bon+09]. The overall

efficiency will depend on three different factors:

$$PDE = QE \cdot FF \cdot Pa$$

QE is the quantum detection efficiency, which is the probability of a carrier being generated after a photon is absorbed. This parameter depends on the wavelength of the incident photon and in silicon detectors it is rather high ($\approx$ 80% at 500nm [GMS19]). FF is the fill factor, which is the ratio between the active and the real area of the sensor. Pa defines the probability of any carrier generating a Geiger discharge.

- **Dynamic range and Linearity.** The dynamic range of a SiPM can be defined as the optical wavelength range where the sensor gives an output. This range depends on several parameters such as the total number of microcells fired, the overvoltage used and the wavelength of the incident photons. In gamma spectroscopy, the more linear a detector is on the desired energy range, the better. Due to how SiPMs are built and operated, nonlinear behaviour is expected. Linearity will depend on the number of cells fired when photons are detected. As the number of photons increases, two or more photons can enter into the same microcell. Each of the microcells only detects if a photon has entered the sensor, which means that the linearity of the detector will degrade with the increase of the number of photons. For this reason, using smaller sized microcells results into a better linearity and a greater dynamic range.

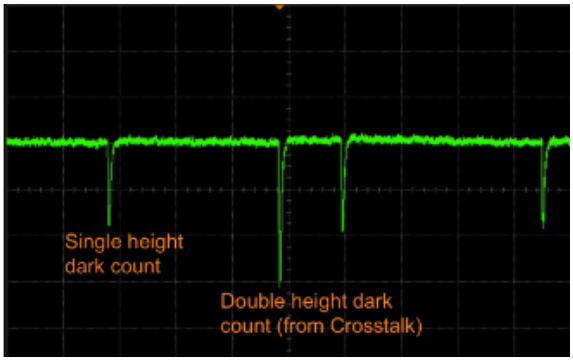

Figure 10: Example of dark noise signals in a SiPM detector, image taken from [ONS21a]

- **Dark noise.** It is the main source of noise in a SiPM. Such noise is generated from a thermally excited electron which causes an avalanche of its own. This *false* signal is indistinguishable from a signal generated from a photon and there are two ways to restrict this noise. The first one is to increase the threshold above the single photon level, so false triggers from the noise are reduced. The other solution is to reduce the temperature, since for every 10 degrees reduction, dark count rate can go down by 50% [LFA00].

- **Optical cross-talk.** During the avalanche process, some of the kinetic energy that the carriers have can be emitted as phonon vibrations through the crystal, but also, as photons. Photons may travel to neighbouring microcells and trigger another Geiger discharge, generating secondary pulses. This process is called optical cross-talk [Nak+19] and is dependent on the overvoltage used and the fill factor of the microcell. Unfortunately, there is no way to discriminate against prompt cross-talk pulses (as seen in Figure 11 left), except for the use of an upper-level discriminator. Optical cross-talk in SPAD is discussed in [Rec+08] and test measurements are discussed in [Eck+10].

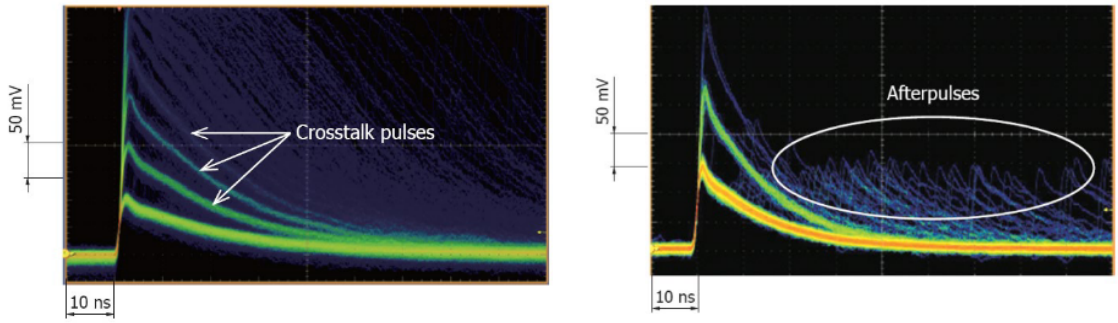

Figure 11: **Left:** Cross-talk pulses out of a MPPC (SiPM) detector, image taken from [LFA21]. **Right:** Afterpulses out of a MPPC (SiPM) detector, image taken from [LFA21]

- **After-pulses.** When an avalanche occurs (either by a photon-induced or a thermal-induced carrier) a portion of the carriers get trapped into impurities of the silicon crystal. These carriers are released after a short delay (around 1-10 ns, Figure 11 right), generating an after-pulse signal. The production of this secondary avalanches will depend on the breakdown voltage and the amount of impurities that are on the crystal lattice [Gar+14].

Over the last decade, SiPM based-detectors have started to replace the PMT in several fields [And+06; Bil+08; Moe+06]. With a similar gain and a lower power supply the SiPM begin to be used in the field of nuclear spectroscopy since the PMT is not an optimal choice for these types of experiments under the presence of the magnetic field. The magnetic fields will represent an upgrade on the current state of the art on fission-related experiments by allowing an easier fragment selectivity and allowing the fission process deeply. With similar characteristics as the PMT, SiPM are however immune to the effects of magnetic fields making them an ideal alternative to study under this harsh conditions.

3.3 Development of fast-timing detectors for FIPPS

Nowadays, lifetimes down to the 10 ps range are measured at the Fission Product γ-ray Spectrometer (FIPPS) by coupling an ancillary device made of $LaBr_3(Ce)$ to the HPGe core array. For future phases of the development, this will not be an optimal choice, since PMTs become inoperable in strong magnetic fields [Chr+95]. For that reason, an alternative has to be developed in order to continue these experiments at FIPPS. The new detector should meet the following conditions in order to be considered an effective replacement for a $LaBr_3(Ce)$ coupled to a PMT tube:

- Immunity to magnetic fields
- Similar or better performance compared to the $LaBr_3(Ce)$ coupled to a PMT.
- Compact-size

This section gives an overview of the three main pieces that conform the proposed detector: the scintillator crystal, the SiPM sensor chosen, and the electronic readout used to process the signals.

3.3.1 Scintillator of choice: $LaBr_3(Ce)$ crystals

Over the last decades, $LaBr_3(Ce)$ scintillator crystals have replaced the traditional BaF_2 crystals used since the origin of the fast-timing $\beta\gamma\gamma(t)$ technique [MGM89]. Although BaF_2 crystals have an excellent time resolution, down to 120 ps at ^{60}Co energies, the main limitation comes from the energy resolution; being around a 9% at 662 keV from ^{137}Cs [Cer+04].

$LaBr_3(Ce)$ crystals combine a fast time response ($\approx$100 ps or more at ^{60}Co energies) with an excellent energy resolution (3-4% at 662keV from ^{137}Cs), making them an ideal choice for the fast timing technique [Ved+; Ved+17]. Good energy resolution is an advantage in fast-timing techniques, since nuclei studied with this technique may have complex decay level schemes with several γ-rays of similar energies. The capability to distinguish between these gammas, and all that derives from it, makes the $LaBr_3(Ce)$ crystals the preferred choice for this application. The performance of this crystal comes from several factors; such as the size, shape and the internal crystal structure itself. The structure of the crystal determines the amount of photons per keV produced as well as the lifetime of the excitation inside the crystal, affecting the decay time of the scintillator. Another parameter to take into account is the amount of Ce doping that the crystals have, since it's proved to influence the time and energy resolution of these detectors [Glo+05] up to a certain degree [Dro+08]. Table 3.3.1 shows the properties of both the $LaBr_3(Ce)$ and BaF_2.

Commercially available $LaBr_3(Ce)$ crystals come in different size and shapes. Crystals of larger sizes have a better detection efficiency than smaller ones, but due to internal reflections on the crystal, the energy and time resolution worsen. During

Scintillators	Specific Gravity	Wavelength of maximum emission (nm)	Refractive Index	Decay time (μs)	Light Yield (Photons/MeV)
CsI(Na)	4.51	420	1.84	0.46, 4.18	39000
BaF_2 (fast)	4.89	220	1.56	0.0006	1400
BaF_2 (slow)	4.89	310	1.56	0.63	9500
$LaBr_3$(Ce)	5.29	380	2.05-2.10	0.026	63000

Table 2: **Properties of BaF_2 and $LaBr_3$(Ce) inorganic scintillators, data taken from [Kno10]**

the tests performed with the SiPM readout a truncated cone geometry has been employed, since it has been proven to improve the light collection on the crystal while maintaining a good compromise between the energy resolution, the efficiency and time response [Ved+; Ved+17].

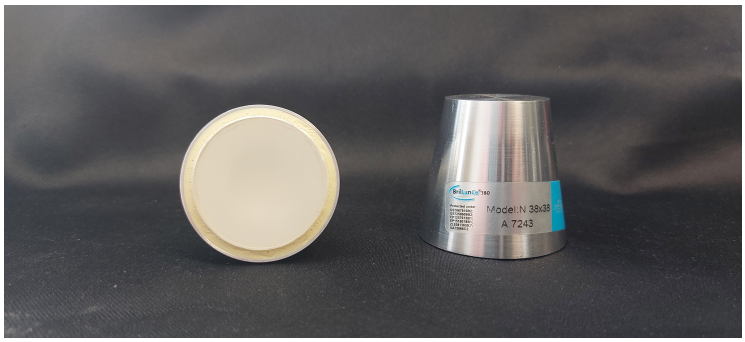

Figure 12: Conical $LaBr_3$(Ce) used on the characterization of the SiPM arrays

Measurements reported on this thesis come from a truncated cone $LaBr_3$(Ce) crystal coupled to the SIPM arrays under study. The crystal, displayed in 12, is 1.5" in height and has diameters of 1" and 1.5" on the small and big bases, respectively. The same crystal has been coupled to a R9779 PMT to perform a full performance comparison. During the timing measurements, the detectors were put against a reference detector, which consists of a cylindrical $LaBr_3$(Ce) with 1" in height and diameter coupled to a R9779 PMT.

3.4 The sensor: from single photo-detection sensors to array-based readouts

As previously discussed, SIPM can be purchased from different companies such as Hamamatsu Photonics (Japan), onsemi (previously SensL or ON semiconductor from Ireland), Broadcom (US).... During the first stage of the development Hamamatsu and onsemi sensors were selected. The goal of this stage was to develop a simple electronic scheme in order to process the signal and to test the energy resolution of each sensor in different placements of the $LaBr_3$(Ce) crystal. Sensors under

testing during this phase are displayed in Table 3.

Sensor	**Company**	**Active surface area (mm^2)**	**Spectral Response (nm)**	**PDE (%)**	**Gain**	**Fill Factor (%)**	**V_{bias} (V)**
13360-3050CS	Hamamatsu	3.0 x 3.0	450	40	$1.7x10^6$	74	53 ± 5
13360-6075CS	Hamamatsu	6.0 x 6.0	450	50	$4.0x10^6$	82	53 ± 5
J30035TSV	onsemi	3.07 x 3.07	420	30-38	$1.9x10^6$	62	25 ± 5
J60035TSV	onsemi	6.07 x 6.07	420	30-38	$1.9x10^6$	75	25 ± 5

Table 3: **Individual properties of the SiPM prior to the array development**. Each of the individual sensors first tested were single SiPM sensors with a similar active area. Data taken from [ONS21d; Ham21]

All the sensors are n-p, which gives a spectral response peak at 420-450 nm, which is near the 380 nm where the $LaBr_3(Ce)$ emits its peak. The values in Table 3 are where the maximum detection is achieved but the detection range goes from 300 up to 900 nm[ONS21d; Ham21].

Since the single onsemi detectors were welded in a SMA board [ONS21d], studying the placement of the SiPM with this sensor was not optimal. For that reason, a readout for the Hamamatsu detectors was developed. The first version of this detection device was a 3x3 array made of 13360-3050Cs sensors. This circuit allowed the implementation of 4 13360-6075CS sensors at the cost of removing 6 13360-3050Cs sensors but increasing the effective covered area.

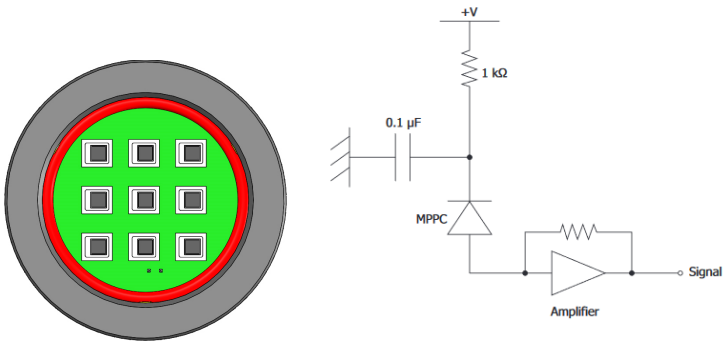

Figure 13: **Left: Array made of Hamamtasu 13360-3050CS sensors.** The array was built in order to study the signals and the energy response of the $LaBr_3(Ce)$ crystal in different places of the crystal. The distance between two sensors is equal to the size of a 13360-6075CS sensor, being able to swap two of the 3050CS sensors with one 6075CS in order to cover more area. **Right: basic electronic readout for single SiPM**: biasing and readout for any SiPM including the processing of the signal by employing an operational amplifier

Since the goal of this array was to study the energy response dependence with the placement of each sensor on the crystal, an independent channel electronic readout was implemented. This type of readout is the most straightforward way to obtain

individual information of every sensor in the array. In this case we end up with a 1:1 readout, since each of the SiPM will have its on amplification and data acquisition channel. The goal of this readout is to distinguish multiple interactions or scatter in the array, which makes them a reasonable choice of readout where position sensitivity is a key parameter such as PET imaging or TOF measurements at the expense of the large number of channels. A vertical cut of the first array is displayed on Figure 14 right, while the electronic used for the array can be seen in Figure 14 left.

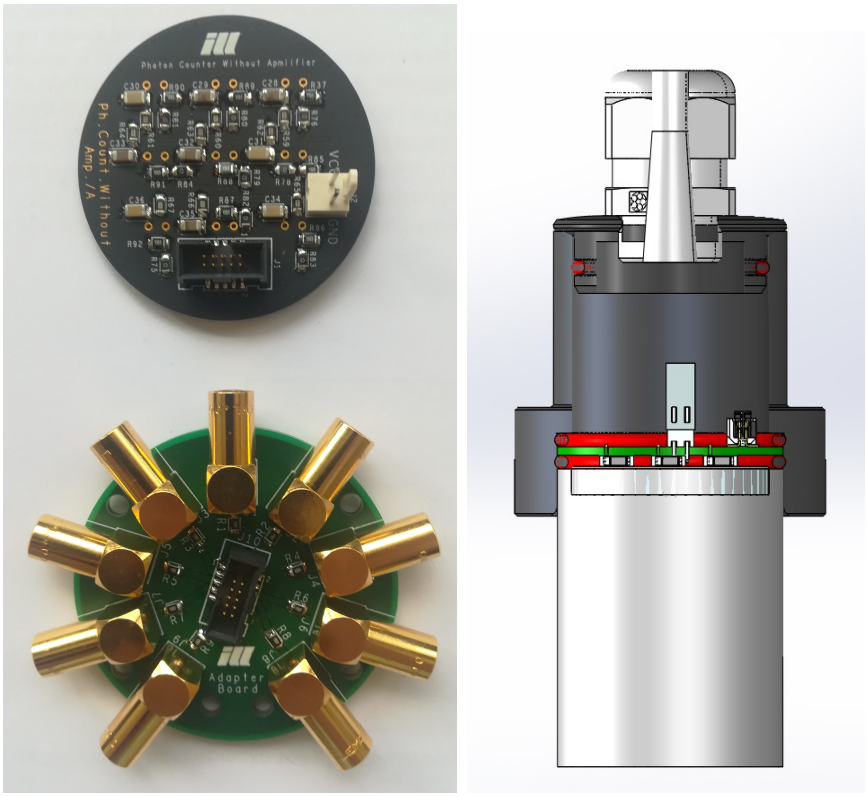

Figure 14: **Left: Electronic readout for the Hamamatsu array.** It is an independent channel readout, each of the signals goes from the readout (black piece on the top) to an intermediate signal that connects the sensors to the digitizers with lemo cables. **Right: vertical cut of the Hamamatsu array.** The signal from the sensors placed on the crystal go through the readout (in green, on the left image it's the top piece) to an outside piece before being processed into the digitizers (down piece on the left image).

Each of the signals is processed individually by an operational amplifier, see Figure 13 for a basic biasing and readout electronic scheme. A procedure to study the placement of the sensors on the crystal coupled to the scintillator was applied, no clear difference on energy resolution was observed during testing. Each of the 13360-3050CS sensors covered a small fraction of the crystal (≈3%) giving an energy resolution of 15.2% at 662 keV for a ^{137}Cs source. In order to study the energy resolution dependence with the surface covered of the crystal each of the individual

signals was summed up with an operational amplifier. The result, plotted in Figure 15 shows that covering larger fractions of the area improve the energy resolution. In order to increase the surface area for the plot the 13360-3050CS sensors were swapped for the 13360-6075CS.

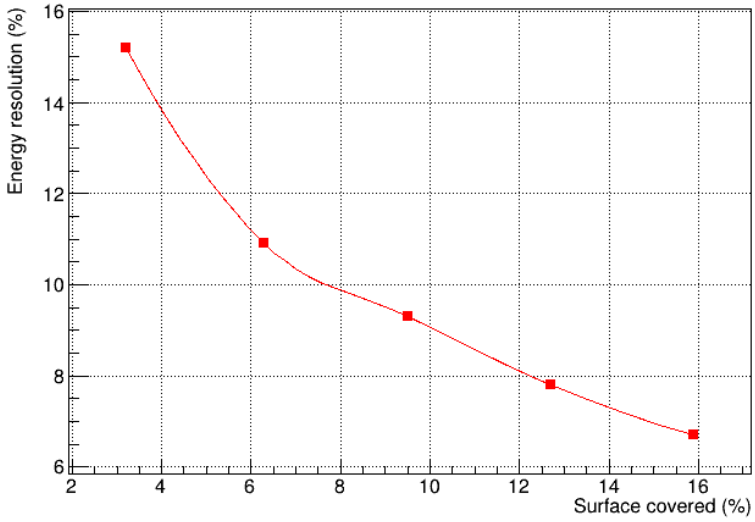

Figure 15: **Energy resolution dependence with surface covered of the crystal**. Energy resolution corresponds to ^{137}Cs energy resolution with a SiPM biased at 29V.

On light of the preliminary results, a larger array needed to be developed since the performance of the array on energy response were not competitive with the PMT value (4.0% at 662 keV for a ^{137}Cs source with an R9779 which is focused on fast-timing measurements). Timing testing was performed giving a convoluted time resolution (CRT) of ≈650 ps for ^{22}Na energies, against a 160 ps value for the PMT tube.

For the new version of the array the Onsemi conductors were chosen as a suitable replacement for the Hamamatsu detectors. Two reasons made Onsemi sensors stand out from the rest of the brands: the fast output and commercially available readouts. Each Onsemi sensor has two outputs: the "standard output" and a "fast output", the former one is a slower signal while the latter one is a faster signal result of the internal switching of microcell in response to photon detection. This fast output is unique to Onsemi detectors, and the main difference between both signals is the capacitance, being much lower on the fast (roughly 1 pF) than the standard (around 100 pF) [ONS21d]. The idea behind implementing sensors into the array comes from trying to give a similar work flow as the PMT tube used in fast-timing experiments: the lower signal being used for energy measurements while the fastest signal will serve to perform timing measurements. The other thing that made Onsemi a more attractive solution is the commercially available electronic readouts for the signals, although those are not optimized for fast-timing experiments [ONS21d].

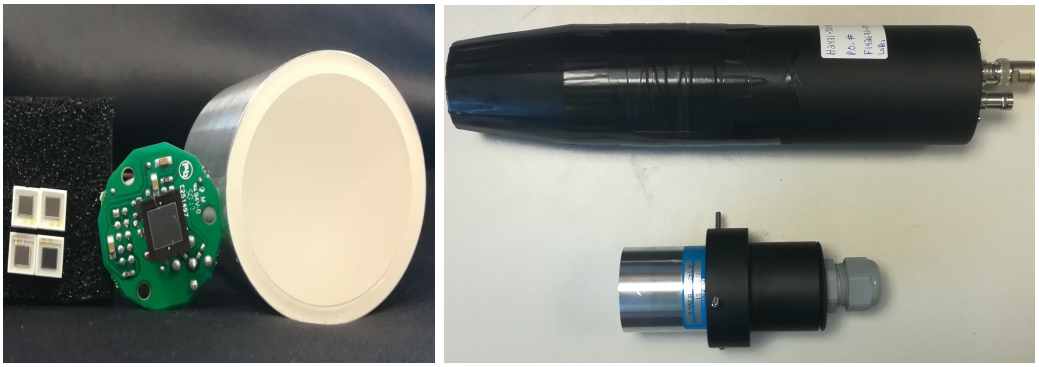

Figure 16: **Left:** Individual Hamamatsu sensors compared to a $LaBr_3(Ce)$ crystal. **Right:** Size comparison between a PMT tube and the hamamatsu array.

The chosen sensors for the new array development were two: the MicroFJ-30035-TSV and the MicroFJ60035-TSV. Both of the sensors have similar capabilities as the Hamamatsu sensor previously tested which are displayed in Table 3. In particular, the 30035-TSV sensors were integrated into ArrayJ-30035-64P commercially available. It's an 8x8 array, as can be seen in Figure 17, that covers approximately 65% of the crystal (Figure 17 (b)). While the custom-made MicroFJ-60035-TSV array is a 6x6 sensor square array without the corners and covers mostly all the crystal, as can be seen in (Figure 17 (c)). Both arrays are displayed in figure 17 (a).

Nowadays, creating large arrays with minimal dead space between SiPM is a well-developed process, making custom-built SiPM arrays a good option to cover the needs of the user. The custom-made array has been built following the instructions indicated by Onsemi in [ONS21b], taking care that no sensor is damaged in the welding process. In order to be able to implement future electronic updates, the sensor array and the electronics are separated in two different printed circuits, connected by DF17(3.0)-80DS-0.5V(57) connector in case of the custom-made array, and DF17(2.0)-80DS-0.5V(57) for the ArrayJ-30035-64P.

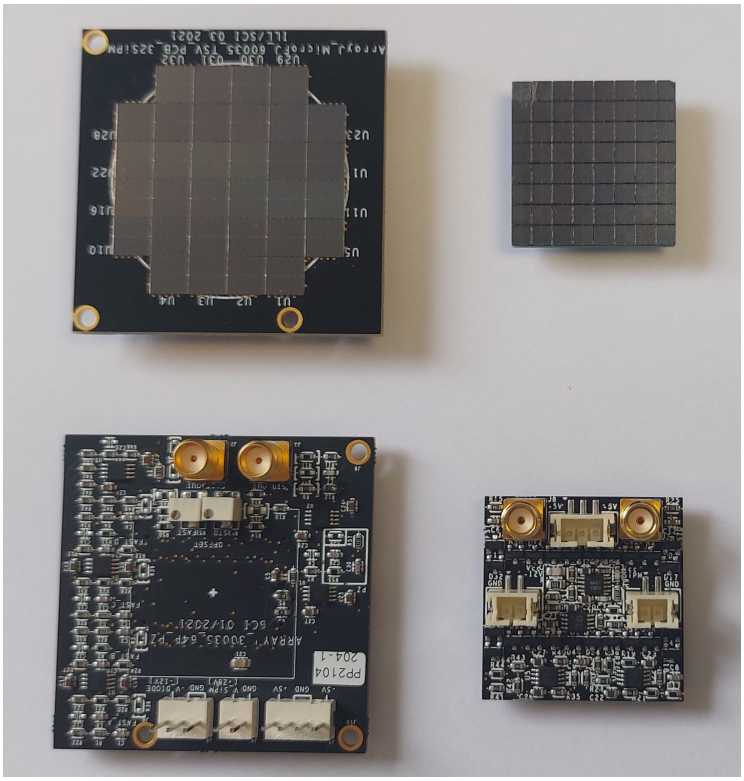

(a)

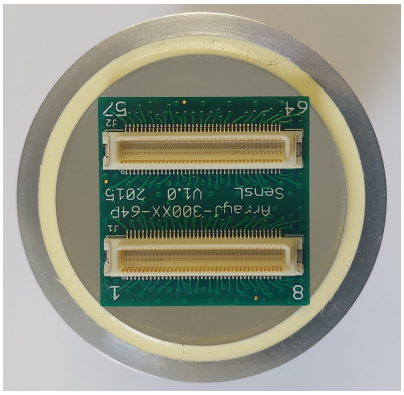

(b)

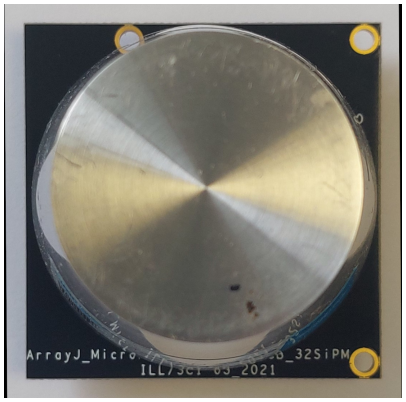

(c)

Figure 17: **(a)** On top, MicroFJ-60035-TSV custom-made array (left) and Arrayj-30035-64P (right), electronic readout for each of the arrays is located down. **(b)** Coupled $LaBr_3$(Ce) to the Arrayj-30035-64P. **(c)** Coupled $LaBr_3$(Ce) to the custom-made MicroFJ-60035-TSV array.

3.5 Electronic readout for large arrays

The idea behind the proposed readout is similar to the PMT tube working principle in fast-timing experiments: the slower signal will go for energy measurements while the fast one will go for timing measurements. In PMTs, only two signals come out of each device and it's simple to implement into analogue modules to perform fast-timing measurements. For the proposed SiPM array this is not an optimal option since each sensor provides 2 signals per sensor, making 64 and 32 signals from each output for the 60035-TSV and 30035-TSV respectively. Implementing the independent channel readout is not a realistic option since the amount of electronics required for each of the signals would require a large amount of space and would be costly. In fast-timing experiments the position where the scintillating light coming from the same crystal gives no valuable information, hence this channel readout was discarded.

Since the purpose of each signal coming out of the sensors is different, the proposed readout processes each signal differently. In case of the standard output, a passive method has been implemented by summing all the signals in order to get the best energy response possible. On the other side, this cannot be done for the fast output signals coming out of the sensors since the goal of the readout is to obtain the fastest signal in order to get the best time response possible. For this reason, an active approach has been developed for the fast output, which consists in grouping the SiPM signals using Schottky diodes and summed the faster signal of each group using wideband amplifiers. This method is the most effective way to optimize the electronics for a simple structure, reducing the signal-to-noise ratio of the sensor. A block diagram for the proposed readout is displayed in Figure 18. Both of the arrays have been grouped the same way; each is divided into 4 equal size sections corresponding to the corners of each array. This makes each group have 8 and 16 sensors for the 60035-TSV and 30035-TSV array respectively.

The bias voltage (V_{bias}) on this design has been chosen to be positive, following the instructions from [ONS21c] in order to get a better timing performance from the fast output.

All the standard outputs are added up and only one resistor is used for all the array and coupled directly to ground, ensuring DC coupling. The summed signal passes through 2 shaping phases made with AD80066ARMZ and AD8012ARMZ. The first one is a dual voltage feedback amplifier which offers a high performance at 145MHz bandwidth and a slew rate of 180 Vμs. On the other hand the AD8012ARMZ is a dual current feedback amplifier that combines low power capable of providing 350 MHz bandwidth and has a slew rate of 2.25kV/μs. While AD80066ARMZ uses up to 6.4 mA while AD8012ARMZ uses only 1.7 mA per amplifier, making them an optimal choice for this application. Both of the amplifiers have been biased at $\pm$5V.

This cannot be done to the fast-output of all the sensors. When each channel is summed up, the capacitive load of each channel adds up, worsening the rise time

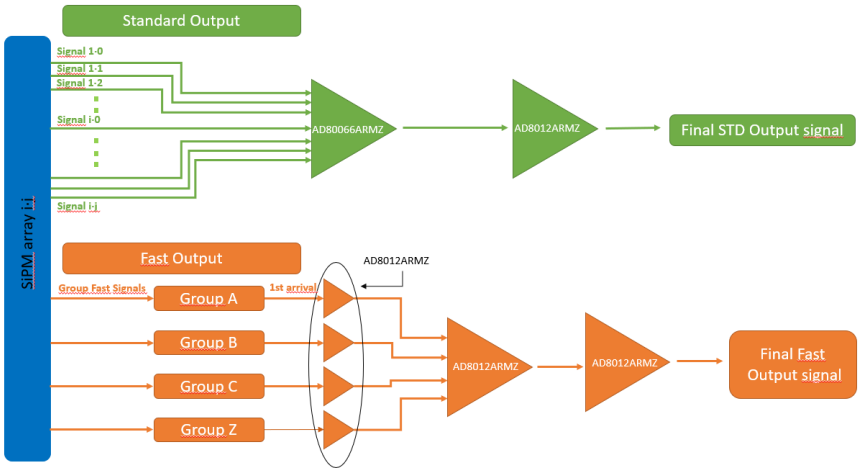

Figure 18: **Flow diagram of the proposed SiPM readout.** Both of the characterized arrays have the same electronic readout, just varying in the cells forming each group. In green, all the standard output signals to study the energy response while in orange, the first arriving signal of each group is summed in order to perform timing measurements

of the signal as well it's height. For this reason, an alternative method has been implemented on the fast output signal path. This method consists of an active approach, dividing the arrays in four groups of cells and adding the fastest signal out of each group. Each group is DC coupled with an extra capacitor per group, in order to filter interference between standard and fast signals on the readout. A block scheme of the proposed readout is presented in Figure 19.

In order to get the fastest signal from each group a proposed method by ON semiconductor [ONS21b] has been implemented into the readout. This method relies on the use of Schottky diodes which are produced by the junction of semiconductor and a thin metal layer [Ahm07]. These diodes have been used for over 25 years due to a very low forward voltage (≈300 mV) drop and switching speeds (≈100 ps) making them ideal for working at very high frequencies (GHz) [Mic; PN87].

Each array is divided into 4 groups, each made of 16 sensors (in case of the 30035-TSV array) or 8 sensors (in case of the custom-made 60035-TSV array). All the fast outputs from the sensors on each group are connected to individual diodes in series, and each of the cathodes from these diodes are connected in parallel. This is done so when the Schottky diodes are biased, defined as V_{diode}, the first signal of each group will block the other diodes, providing the fastest signal from each group. Due to the isolation from the rest of the fast outputs, the fast signal from each group will be the only one contributing to the capacitive load. With this method, the signal-to-noise ratio is improved while maintaining the bandwidth of the signal. Each fast signal will go through three more stages, each consisting of passing through an AD8012ARMZ operational amplifier before the final output; on the first stage each signal is increased by a factor of three. After this stage, the four signals are

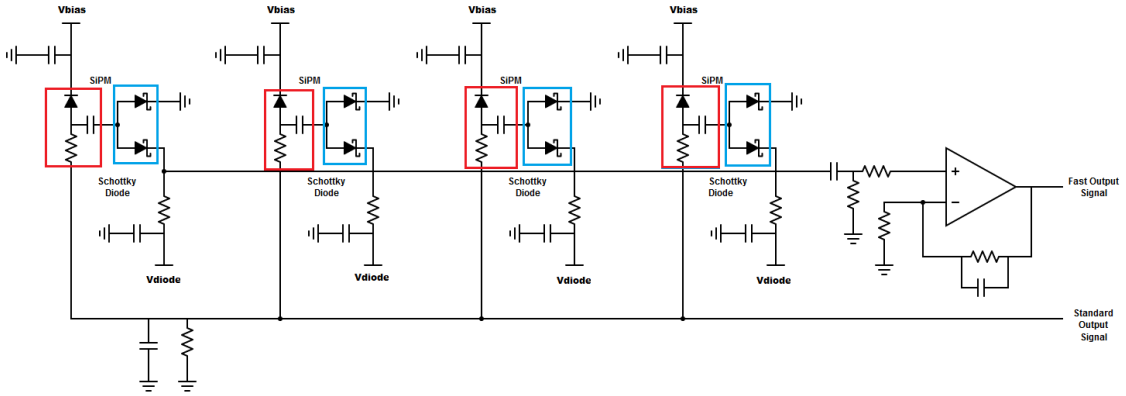

Figure 19: **Simple diagram for the extraction of the first arriving signal for a group (example with a group of 4 SiPM).** Squares in red denote a ONsemi cell and surrounded in blue are the Schottky diodes, connected in series in order to extract the fastest signal from each group.

added in a summing inverter amplifier phase. The polarity of the final fast signal comes from the last phase, where an inverter amplifier with gain 1 makes the final signal positive.

At the end of the circuit both signals display a positive polarity, in order to adjust the offset of the two signals a potentiometer is placed at the output. The crystal coupled to the arrays and the readout is encased into a black PLA (PolyLactic Acid) structure, as can be seen in Figure 20.

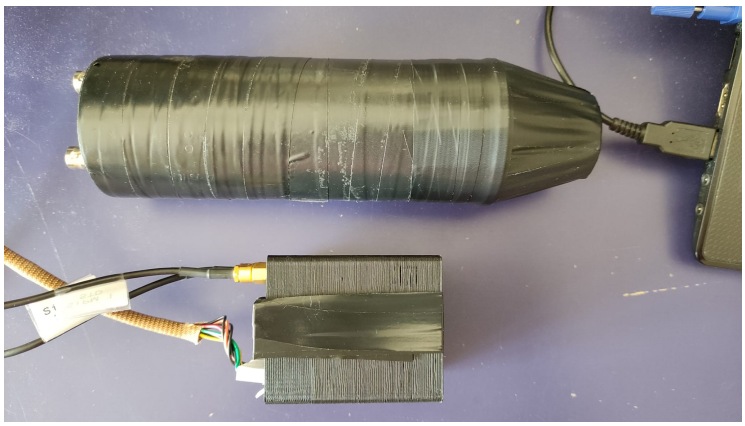

Figure 20: **Size comparison between the PMT (top) and the SiPM based detector (down).**

While the standard output of the signals display a rise time of 20 ns of both arrays (the fast-output differs slightly, as can be seen in Figure21. On the 30035-TSV array, the rise time is 14-16 ns, while the 60035-TSV one is 18-20 ns. Since the time response of a detector is related to the rise time of the signal, we can expect a

faster response from the 30035-TSV array. On the other hand, both of the standard outputs are 15-30 μs long, due to the capacitance addition of every standard output signal from the sensors plus the long decay selected (on the ms range) for the first version of the detector. A digitizer has to be chosen carefully so the length of the final standard output does not hinder the performance of the detector. Nonetheless, in this version of the detectors dead time effects will occur, affecting the performance of the detector. In future versions of the arrays a shorter decay time will be applied, at least below the μs range, in order to avoid such problems.

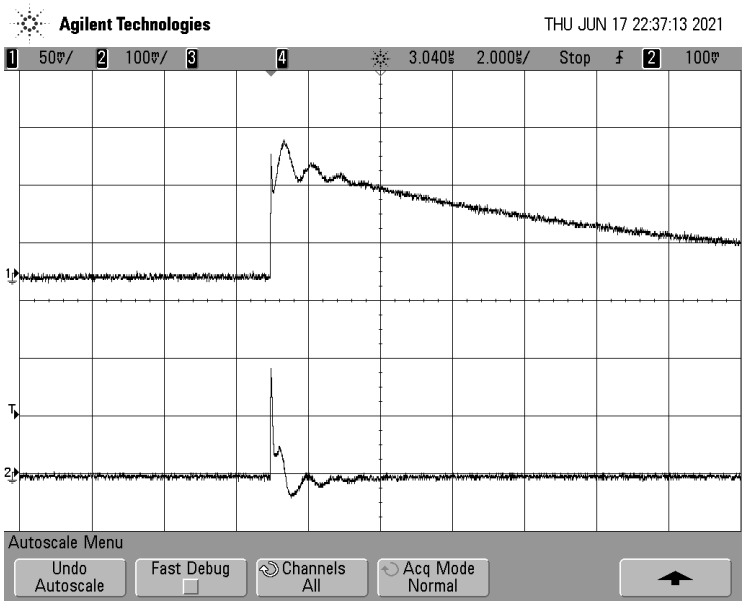

Figure 21: **Signals coming out of the 60035-TSV array.** The standard signal is displayed on top, while the shorter signal is the fast-ouput signal at the end of the electronic readout. Similar behaviour occurs in 30035-TSV array.

3.6 Spectroscopic features

This section focuses on the spectroscopic features of $LaBr_3$(Ce) scintillator crystals coupled to the SiPM arrays described in previous sections. The crystal coupled has a truncated cone shape, giving a reasonable energy resolution combined with a good fast-timing response. In order to perform a realistic comparison, the crystal has also been coupled to a Hamamatsu R9779 PMT. This PMT has been optimized for timing applications at the expense of a slightly worse energy resolution [Ved+; Ved+17].

Both of the signals coming out of the array could be used in order to study the spectroscopic features of the detectors, but only the standard output of the arrays and the dynode signal from the PMT have been used. The fast-outputs and the anode signal from the PMT have not been used since their sole purpose is to study

the time response. Caen DT5720B desktop digitizer has been employed on all the testing. This digitizer is used for energy characterization since it can trigger up to 130 μs signals with a 250Msamples/s. All testing has been performed in a 27-31V bias voltage range.

3.6.1 Energy resolution

One of the main parameters to evaluate when testing detectors is energy resolution, which is defined as the ability of a given detector to accurately distinguish between two close energy γ-rays. In fast-timing measurements, this characteristic favours the selection of the proper decay branch under study and contributes to the time correction due to Compton background. This parameter varies depending on the sensor and the crystal coupled to it, or what is referred to as a detector.

In this thesis, the energy resolution has been studied as the ratio between the full width at half maximum (FWHM) of the γ-ray full energy peak (FEP) and its energy E_{peak}. A distinction must be made on the units where both the FWHM and the E_{peak} are measured, if the values are considered in channels instead of keV, one obtains the *apparent* energy resolution. Depending on the linearity f the crystal, the real energy resolution comes when the spectra are calibrated in keV.

Since energy resolution is energy dependent, all values have been reported at 662 keV from a ^{137}Cs source, which is a standard reference.

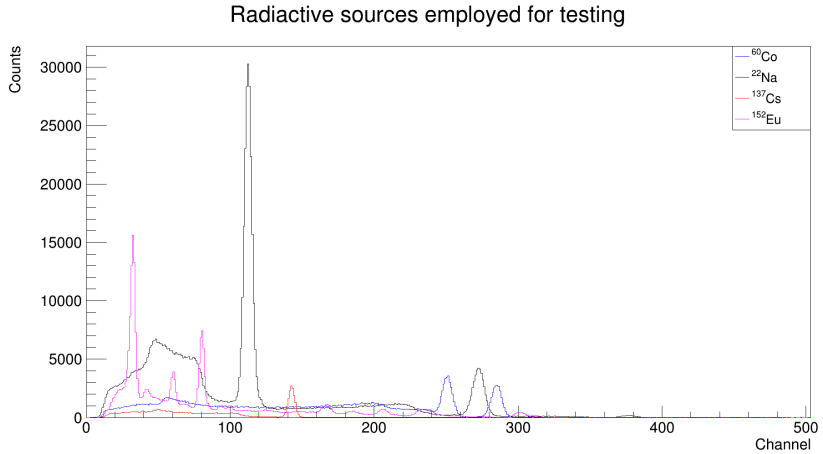

Figure 22: **Spectra from radioactive sources employed for characterization of the SiPM based arrays.**

3.6.2 γ-ray detection efficiency

One of the most important parameters in the construction of fast-timing arrays is γ-ray detection efficiency, which is defined as the probability that a quantum of radiation incident on the detector will produce a recorded pulse. The way to obtain

the photo-detection efficiency is the ratio between the number of events that have deposited their full energy in the crystal and the total number of emitted γ-rays.

The absolute full-energy peak efficiency has been obtained for the two SiPM arrays. This was done by measuring the energy spectra from an absolutely calibrated ^{152}Eu source placed at several distances (5,10,15 and 20 cm).

3.6.3 Energy linearity

The energy linearity is an important factor to the fast-timing method. This parameter measures the proportionality between the output quantity given by a certain detector and the input. A non-linear response will affect the energy resolution, since it needs a different correction, making harder the selection of the decay branch. The crystal used on the characterization, $LaBr_3$(Ce), may display non-linear behaviour due to its high photon-yield which derives into a pulse height non-proportionality.

In order to study this feature, several sources have been used, such as ^{152}Eu, ^{137}Cs and ^{60}Co in order to cover a suitable range of energies, which can be seen in Figure 22.

3.7 Time response

Time response of a detector is given by the time needed to generate an output signal for a given input. In nuclear spectroscopy, the time response will include the time since the crystal has collected the radiation emitted until the sensor produces a signal that, eventually, is fed into the DAQ.

The size and shape of the scintillator crystal are important parameters when performing timing measurements, since it needs to keep a balance between a good timing resolution combined with a reasonable energy resolution and γ-ray efficiency. In this case, testing has been performed using $LaBr_3$(Ce) in a truncated cone geometry, since it helps with light collection and γ-ray efficiency while maintaining a fair time and energy resolution [Ved+; Ved+17] and allow for the construction of compact arrays.

On SiPM array sensors the performance varies with the V_{bias} since electrons jump easily to the conductive band, responding faster to the light emitted by the scintillator. For that reason, testing has been performed by increasing the V_{bias} from 29V up to 32V. This range is given by the properties of the fast output as well as the input signal entering into the analogue chain that will define the time difference between signals. Lower voltages do not give a high enough response to be discriminated from background noise, while larger values than 32 V makes the signal too noisy. This noise comes from the dark current inherent to SiPM detectors, where thermally excited electrons will jump to the conductive band generating false signals.

As said, signal processing plays an important role on the time resolution of each instrument. The preferred option for fast-timing experiments is the combination

of the analogue constant fraction discriminator (CFD) with a time to amplitude converter (TAC) modules. While the second does not affect the time response of the detector itself, the analogue CFD has an impact on timing measurements. This module, further explained in the next section, discriminates the signal based on two parameters: the external CFD delay and the zero-crossing value (Z). Although the Z parameter does not affect the time resolution of a detector, it does affect the time walk which is an important parameter to control during experiments. In order to optimize this, first CFD delay has been optimized and then an adjustment to Z has been performed by an iterative method.

3.8 Experimental setup for time characterization for SiPM arrays

The time response performance of the detector has been characterized by measuring time differences between the SiPM based array and well-tested $LaBr_3(Ce)$ coupled to a PMT that acted as a reference. The reference detector has a 10% nominal Ce doping and is a 1-inch cylindrical crystal. The crystal is coupled to a Hamamatsu R9779 PMT, similar to the one used on the truncated cone, with a bias voltage of -1300V. This combination has been properly tested and characterized by Victoria Vedia for her PhD thesis [Ved], giving an energy resolution of 4.0% at 662 keV and 107(2) ps of time resolution at ^{60}Co energies [Ved+; Ved+17].

Both detectors, the reference and the one under study, were fixed to an aluminum frame aligned and close to each other, with the radioactive source between both of them. Figure 23 shows the experimental set-up as well as the signal processing of the signal.

The standard output (in case of the SiPM arrays) and the dynode signal (in case of the PMTs) are fed directly into the DRS4 Evaluation Board V5 digitizer [San+19]. The timing signals, the anode and the fast output (from the PMT and the SiPM array respectively) are fed into an ORTEC935 Constant Fraction Discriminator. Measurements have been performed with the digitizer with a 5Gsamples/s sampling rate with a precision of the time stamping of 0.2ns.

The ORTEC935 Constant Fraction Discriminator plays an important role since it determines the precise arrival time of incoming signals based on the same rise time fraction. This analogue module only allows negative signals, for that reason a ZX60-3018G-ST pre-amplifier is used to invert the fast output of the SiPM arrays. Each signal that arrives into the module is split into two pulses; the first one is attenuated and delayed by a fixed factor, while the second one is inverted and retarded by the CFD delay. After this, the attenuated and the inverted signals are added together, resulting in a bipolar pulse whose zero crossing indicates the time of arrival of the signal. There is only one instance where the analogue CFD module will not use the CFD method to discriminate signals, and it is when the CFD delay is less than a nanosecond. In this case, the module will trigger the signal using the leading edge discriminator, which is based on the height of the signal, instead of the fraction of

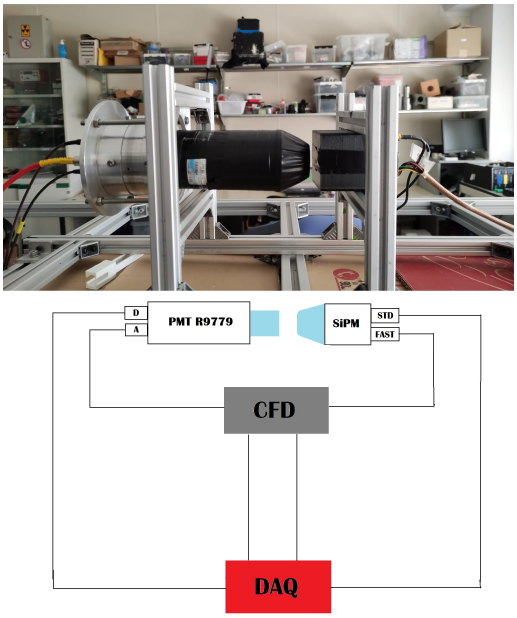

Figure 23: **Electronic setup for timing measurements.** For the time difference measurements, the dynode signal from the PMT and the standard output out of the SiPM array are directly fed into the digitizer and used for energy measurements. The fast output from the array, passes through a pre-amp, so it gets inverted. Both the negative signal from the PMT (coming from the anode) and the fast output of the SiPM array are fed into the ORTEC 935 (CFD). Both of the signals coming out of the CFD are fed into the digitizer, where the arrival time difference between both signals is obtained in the offline analysis.

the rise time. The main advantage of the CFD triggering method over the leading edge one resides on the minimization of problems such as time walk, drifts and time jitter that have an impact into the time response of a detector.

In the experimental setup used to measure time response of the detectors, both of the outputs are fed straight into the digitizer. Data taken from the measurements is sorted in an ROOT-based event builder. The arrival time of the signals comes from the signals out of the CFD output, while the energy response of the detector comes from the standard output or dynode signals.

Two sources have been measured to study the time response of the detector: ^{60}Co and ^{22}Na. In order to see the time difference, an offline energy gate has been selected on each detector. The ^{60}Co γ-ray source emits only two γ-rays after β-decay to ^{60}Ni. The 1173 keV γ-ray feeds the first 2^+ state in ^{60}Ni which decays by a 1332 keV γ-ray in a short half-life(1.5(6) ps which can be considered prompt for own purposes).

In order to obtain the time distribution to study the time response of the detectors a gate on the 1173 keV γ-ray has been placed on the reference detector, the projection obtained in the SiPM-based array shows the 1332 keV γ-ray in coincidence (Figure 24). The Compton continuum results from the 1332 keV γ-rays and thus the

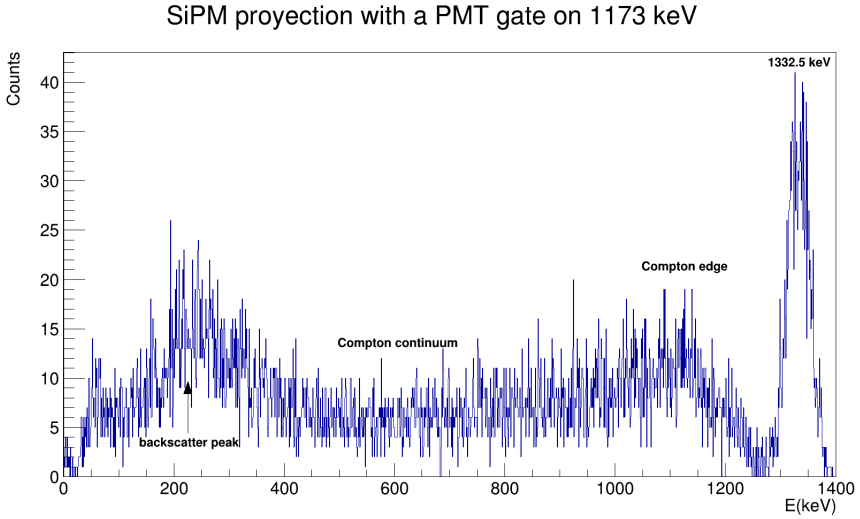

Figure 24: **Coincident γ-ray spectrum of ^{60}Co source obtained by gating the PMT detector on the 1173 keV full energy peak**.

time distributions obtained by gating on it should be prompt. Consequently, there are two time distributions that can be calculated, the one described above and the reversed option: a gate selection on 1173 γ-ray on the SiPM based-array and the 1332 keV γ-ray on the reference PMT. This does not happen when using the ^{22}Na source where one time distribution is obtained since the 511 keV γ-ray comes from the pair production process.

The FWHM values obtained for both sources correspond to the convoluted or coincidence resolution time (CRT), and it takes into account the contribution between the reference detector and the detector under study. In order to get the intrinsic time resolution for each of the detectors under test the value from the reference detector has to be deconvoluted from the CRT.

3.9 Performance evaluation

In this section, a performance review for both arrays is presented. The objective of these tests is to obtain the best parameters for each array and perform a comparison against a well tested PMT, and to assess its possible application for a potential experiment at FIPPS.

3.9.1 Spectroscopic feature: Energy resolution

The energy resolution is obtained by measuring the ^{137}Cs spectra. This source has a single γ-ray making it an excellent pick as a reference. The energy resolution given is defined as the ratio between the FWHM of the full energy peak and its corrected energy (when needed). Best values for energy resolution are 3.7% and 3.9% for the 60035-TSV and 30035-TSV arrays respectively. These values are slightly better than

the ones reported with the R9779 PMT, which is around 4% when biased at -1300V. These values, however, are far from the 3% quoted by the manufacturer when using a Hamamatsu R6231PMT, designed specifically for energy measurements. Table 4 show best energy resolutions obtained as well as the energy resolution for best time response voltage.

Detector	**Type**	$\mathbf{V}_{bias}$ **(V)**	$\mathbf{E}_{res}$ (%)
R9779	PMT	-1300	4.0(1)
R6231	PMT	-1000	3.3(1)
30035 array	SiPM	30	3.9(1)
		32	4.3(1)
60035 array	SiPM	29	3.7(1)
		32	4.1(1)

Table 4: **Relative energy resolution**. Values displayed correspond to the best energy resolution obtained through a voltage sweep of 0.5V and the one that gives best time resolution. Values for the PMT R6231 has been obtained from [Ved]

In addition, energy resolution for both arrays has been measured at several energies, which can be seen in Figure 25. As expected, due to light losses, energy resolution from the 30035-TSV array is worse than the 60035-TSV array.

Also, it can be seen that energy resolutions at low energies are worse than the ones referenced for the PMT tube (approximately 8% at 122 keV and 5.5% at 244 keV), this comes from not being able to resolve the X-rays at those energies properly, being resolved at 31V and 32V.

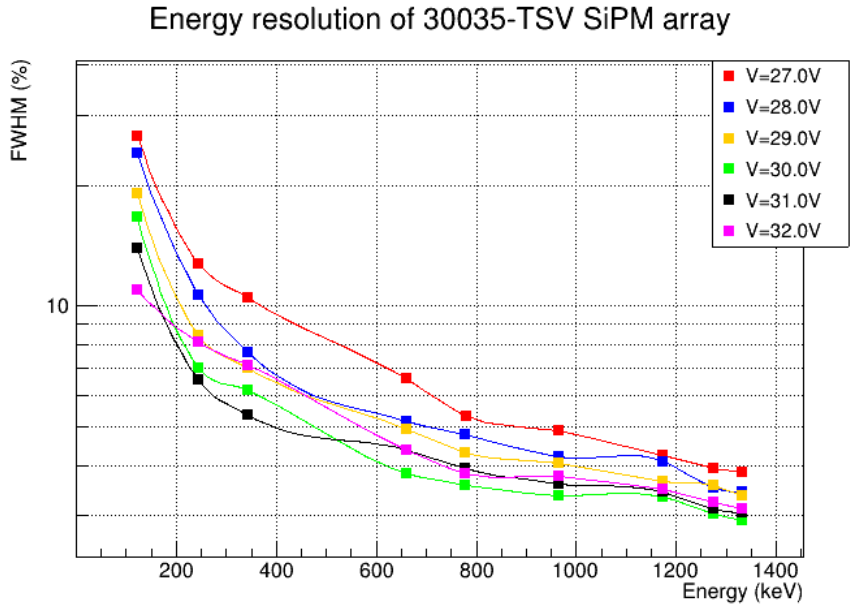

(a)

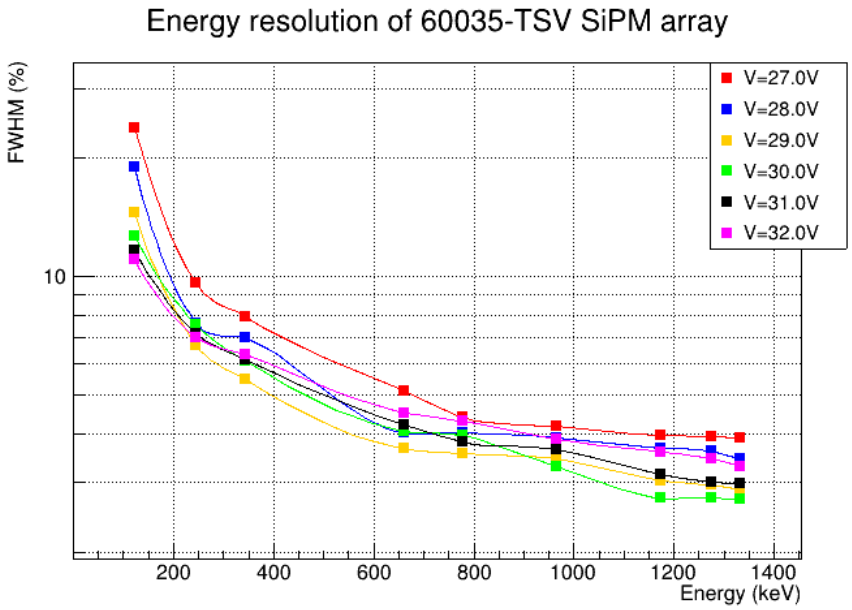

(b)

Figure 25: **Relative energy resolution of SiPM-based arrays as a function of energy**. **(a)** Relative energy resolution for the 30035-TSV array as a function of the γ-ray energy. **(b)** Relative energy resolution for the 60035-TSV array as a function of the γ-ray energy. Sources employed for these measurements were ^{22}Na, ^{137}Cs, ^{60}Co and ^{152}Eu. The uncertainty in the measurements is 0.1%.

3.9.2 Gain and linearity

Both of the arrays are linear over the bias range between 27-30V on the 120-1408 keV range from the ^{152}Eu source. Since the behaviour of both arrays is similar, Figure 27 displays the linearity for the both SiPM-based arrays. As can be seen, deviations start to occur around 30.5V, since the dark current starts to be dominant. In order to illustrate the linear behaviour, only the first 3 points of each data set were linearly fitted up to a channel upper limit (25 channels above the position of the 148keV γ-ray from ^{152}Eu) for each bias voltage. It should be underlined that 60035TSV and 30035TSV arrays have the best energy resolution and linear response at 29V and 30V respectively, making them an interesting choice for spectroscopic experiments.

The gain of each array has also been studied. As expected, both arrays have similar behaviours, and only the 60035-TSV is displayed in Figure 26. A ^{137}Cs source has been employed to see clearly how the spectra moves to the right in a non-linear dependency as the bias grows. It can be noted that the 662 keV on the spectra at 32 V is located roughly at the middle of the spectra (which is 512 channels) for both of the detectors. This makes the dynamic range of the detector at that voltage approximately 1500 keV, not being optimal for experiments with higher energies under study.

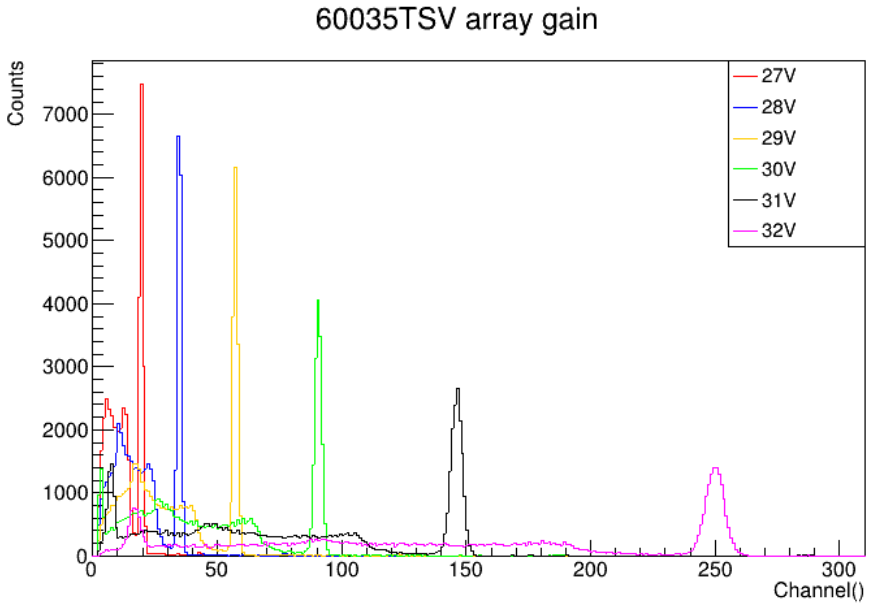

Figure 26: **Gain shift dependence with the V_{bias}.** ^{137}Cs radioactive source spectra, showing the peak placement by increasing the V_{bias} given to the SiPM-based array. The same behaviour is found on the 30035-TSV array.

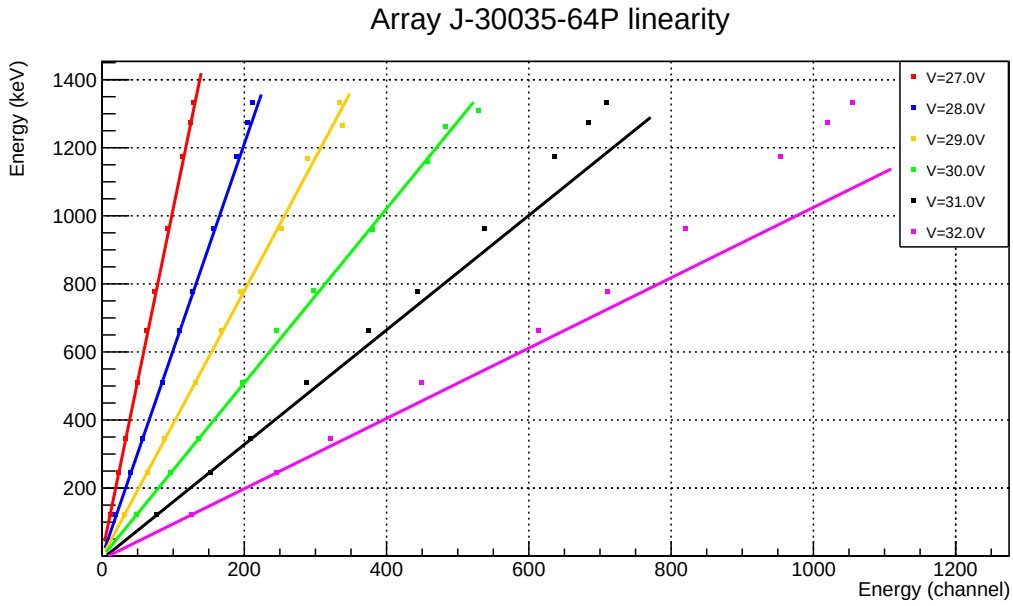

(a)

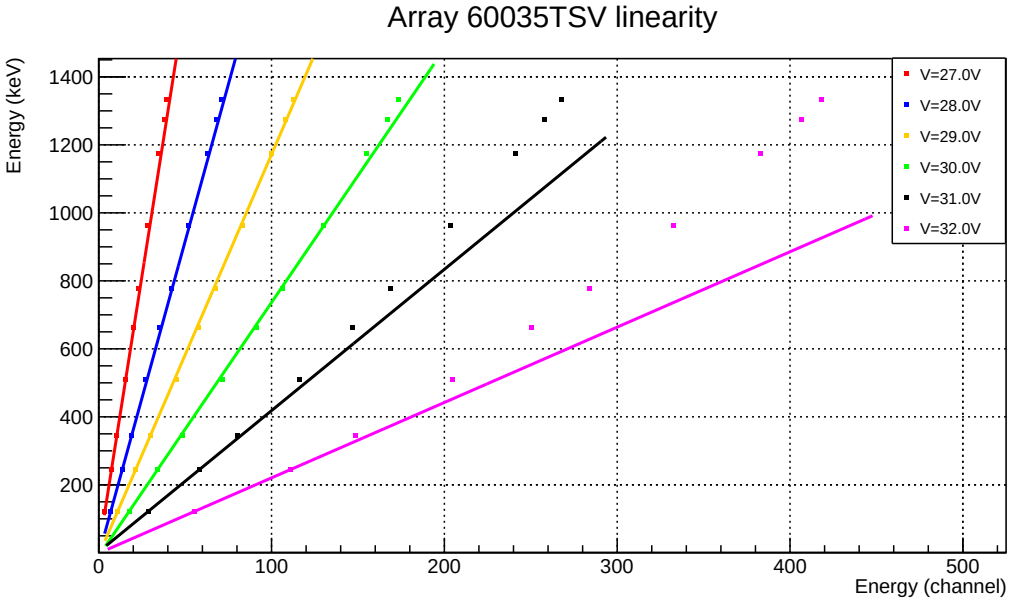

(b)

Figure 27: **Relation between the peak position and the γ-ray energy for 60035-TSV array**. **(a)** 30035-TSV linearity on the 120-1408 keV energy range on a 27-32 V V_{bias} range. is given by the relationship between the energy of the γ-ray and its position. **(a)** 60035-TSV linearity on the 120-1408 keV energy range on a 27-32 V V_{bias} range. Linearity is given by the relationship between the energy of the γ-ray and its channel position.

3.9.3 Spectroscopic feature: γ-ray detection efficiency

The γ-ray detection efficiency has been measured for the detectors in 0.5 V steps from 27 V up to 32 V in 4 different distances from the source (5, 10, 15 and 20 cm). For this testing, an absolutely calibrated ^{152}Eu source has been used in order to cover an energy range from 120 up to 1408 keV. Since the result for every voltage measured is almost identical, within the uncertainty limits, the efficiency is displayed for the values where the best energy resolution and linearity are achieved for both arrays. Efficiency from both arrays can be seen in Figures 28 and 29.

Both of the detectors yield a similar detection efficiency and behaviour. 60035-TSV array has a higher efficiency due to full coverage of the crystal. Nonetheless, these results yield a similar behaviour and values as the R9779PMT at a fixed distance of 10 cm reported by V.Vedia at [Ved]. This, altogether with the rest of the spectroscopic features, makes both of the arrays well suited for γ-ray spectroscopy measurements.

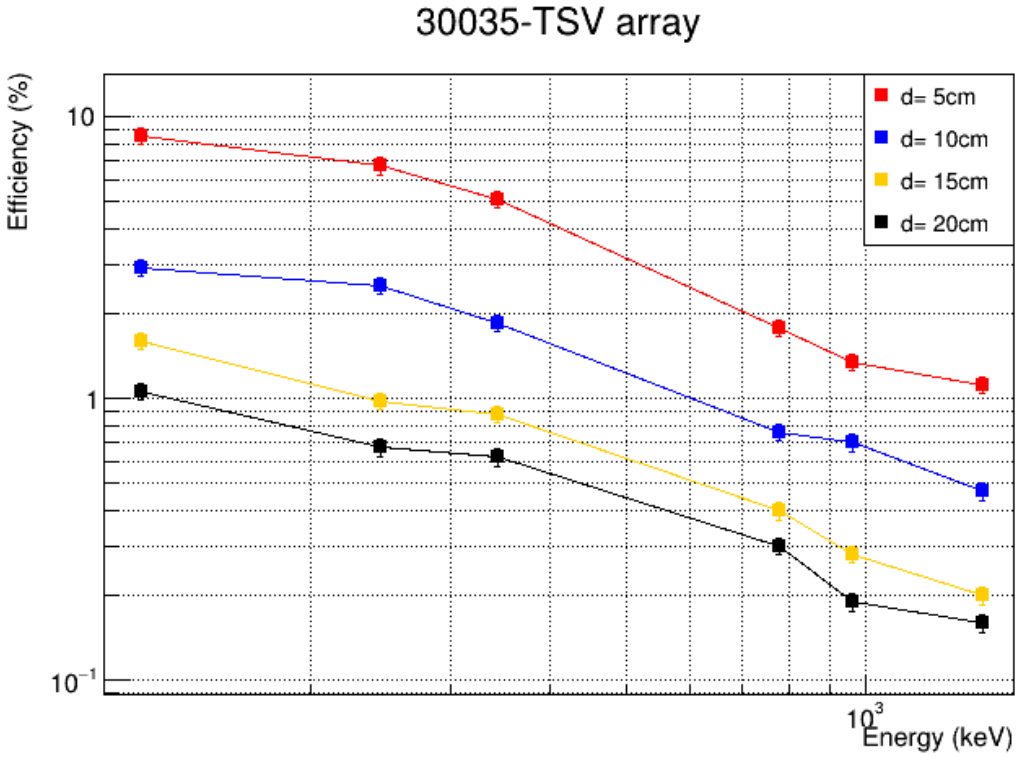

Figure 28: **γ-ray detection efficiency for 30035 array**. The detection efficiency measured at several distances in the range from 122 to 1408 keV from an ^{152}Eu source. Detector was biased at 30 V where the best energy resolution and linearity are achieved

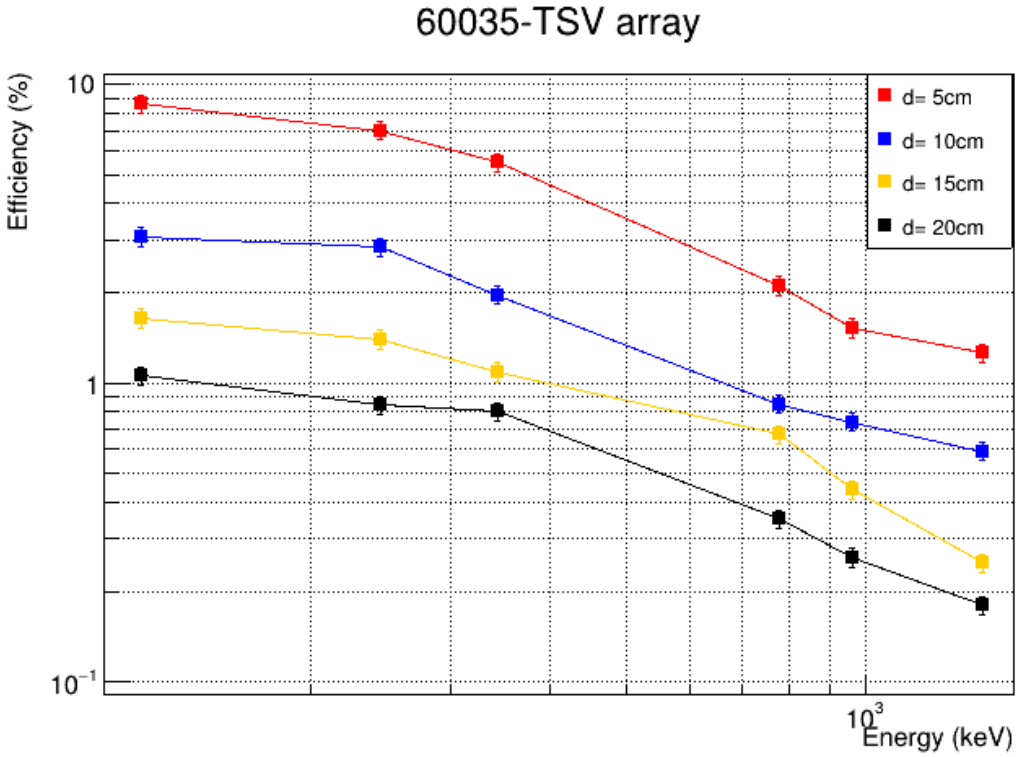

Figure 29: **γ-ray detection efficiency for 60035 array**. The detection efficiency measured at several distances in the range from 122 to 1408 keV from an ^{152}Eu source. Detector was biased at 29 V where the best energy resolution and linearity are achieved

3.9.4 Time response: Time resolution

Several tests have been performed in order to improve and optimize the time response of the detectors. The first testing was to study the dependence between the bias voltage of the Schottky diodes and the time response. As can be seen in Figure 30, the voltage applied to the Schottky diodes does not affect the time resolution of the array. All measurement are within the uncertainty, and differences may be related by temperature variation or external light collection (which SiPM are extremely sensible to).

The other optimized component is the CFD delay, with a range from 2 ns up to 7 ns. This comes from the use of the ORTEC CFD analogue module for testing. This module recommends the use of delay values between a 10% and 40% of the signal rise time for optimal parameters. Having rise time of 15 and 20 ns, for 30035-TSV and 60035-TSV arrays respectively, the test has been performed in 1 ns delay steps. Both of the arrays behave similarly, the dependency of the time response against the CFD delay can be seen in Figure 32 (a), where the best result is obtained at

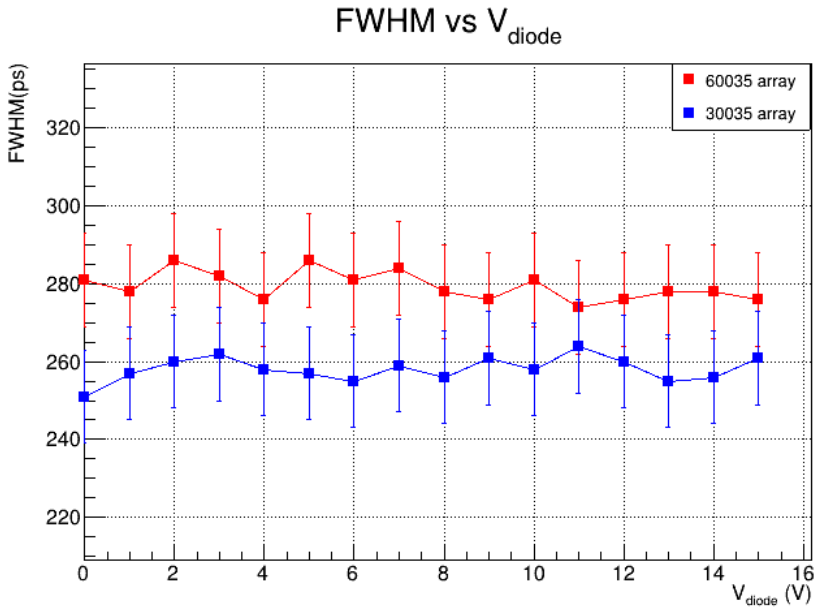

Figure 30: **Time resolution of SiPM arrays as a function of V_{diode}.** Time resolution as a function of the voltage supplied to the Schottky diode. Testing was performed in steps of 1 V from 0 V up to 15 V, maintaining zero crossing at 2.5 mV.

32V and 6 ns of delay, while for the 60035-TSV array these values are 32 V and 5ns delay.

Both of the SiPM arrays achieve the best timing when saturation occurs at 32V. The best convoluted time resolution are 275 and 255ps for 60035-TSV and 30035-TSV detectors respectively. By de-convoluting the obtained time distribution, the intrinsic time resolution for each detector are 256(13)ps for the 60035TSV array and 235(15)ps for the 30035TSV.

Detector	**Type**	**V_{bias} (V)**	**CFD Delay (ns)**	**FWHM ^{60}Co(ps)**	**FWHM ^{22}Na(ps)**
R9779	PMT	-1300V	1.6	110(3)	158(3)
30035 array	SiPM	32	6	235(15)	-
		32	6	271(12)	451(12)
60035 array	SiPM	32	5	256(13)	386((12)

Table 5: **Intrinsic time resolution for both of the arrays and the PMT R9779 at ^{60}Co and ^{22}Na energies**. The 30035-TSV array was damaged under testing and lost a sensor, so no measurement was performed for the ^{22}Na with the full array.

Intrinsic time resolution at ^{60}Co energies from the SiPM-based arrays differs 120(10) ps for the 30035TSV and 150(10) ps for the 60035TSV from the R9779 PMT value, but the differences are relatively small. This comes from the rise time of the signal, while the PMT has an 8 ns rise time, SiPM-based arrays have 15 and

20 ns, 30035-TSV and 60035-TSV respectively, rise time which degrades the time resolution.

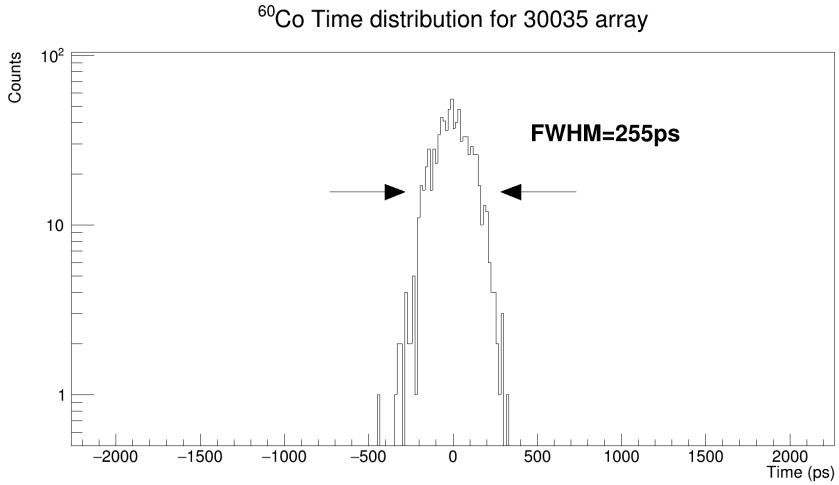

(a)

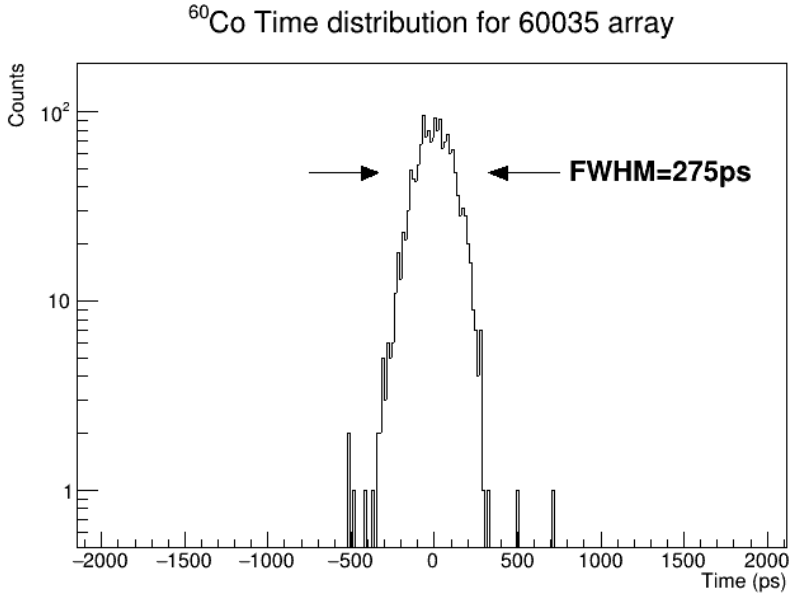

(b)

Figure 31: **Convoluted time resolution (CRT) of a SiPM based-array against a 1-inch cylindrical $LaBr_3$(Ce) detector**. **(a)** Time spectrum from array 30035-TSV biased at 32 V with a delay of 5ns against 1-inch $LaBr_3$(Ce) detector biased at −1300V and a 1.6 ns delay. The FWHM of 255 ps is the convolution from 98 ps from the 1-inch cylindrical $LaBr_3$(Ce) coupled to the PMT tube and 235 ps coming from the array. **(b)** Time spectrum from array 60035-TSV biased at 32 V with a delay of 6 ns against 1-inch $LaBr_3$(Ce) detector biased at −1300V and a 1.6 ns delay. The FWHM of 275 ps is the convolution from 98 ps from the 1-inch cylindrical $LaBr_3$(Ce) coupled to the PMT tube and 257 ps coming from the array

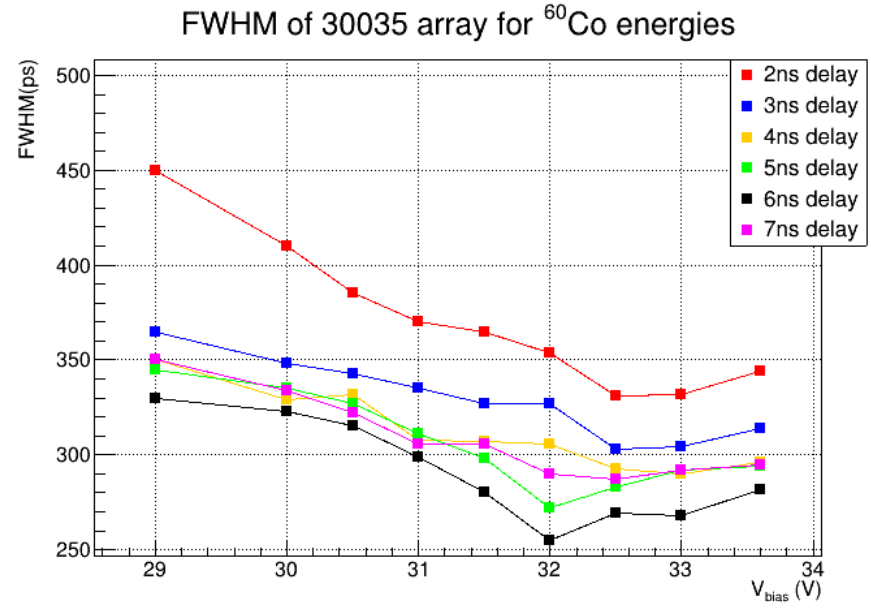

(a)

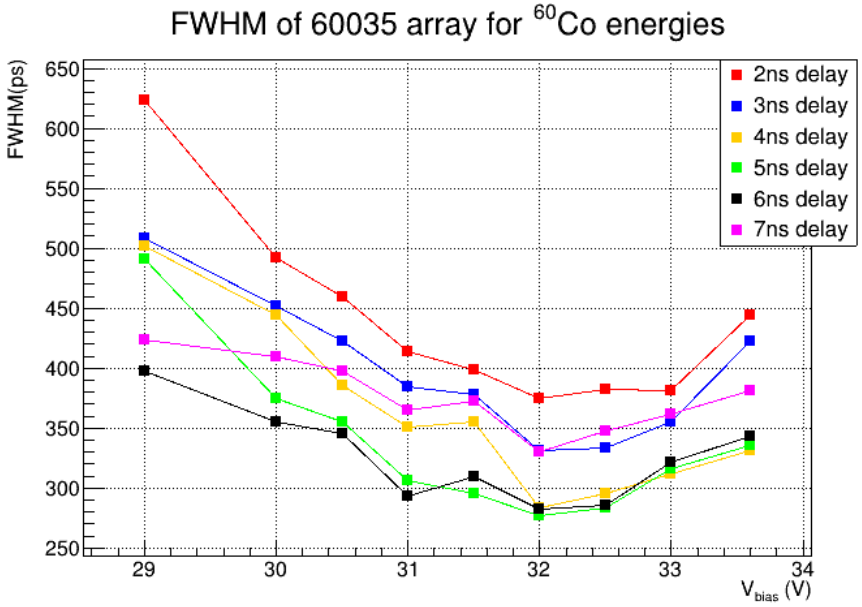

(b)

Figure 32: **Convoluted time resolution of 60035 array as a function of CFD delay**. **(a)** Time resolution of the 30035-TSV array as a function of the CFD delay and the bias supplied. **(b)** Time resolution of the 60035-TSV array as a function of the CFD delay and the bias supplied.

As previously stated, several energy response features are hindered at this voltage, such as linearity and energy resolution. Although energy resolution against a R9779 PMT is rather similar with a 4%, the linearity of the detector needs to be taken into account as well as the dynamic range.

3.9.5 Time response: Time walk

Adjusting the zero crossing potentiometer on the analogue 935 CFD module does not affect significantly the time resolution of the detector. This value, however, affects the time walk, which needs to be corrected in a real life experiment in a wide range of energy.

The analysis has been repeated for zero crossing values from 0 mV up to 2.5 mV showing similar zero crossing values and behaviour for both SiPM-based arrays. Best time resolution has been measured at 2.5 mV. In order to characterize this parameter, a ^{60}Co source has been employed to study the Compton walk of each detector. In order to study the SiPM based-array walk a fixed gate at 1332 keV γ-ray is selected on the PMT tube while varying the SiPM gate on the Compton continuum in 50 keV wide gates in steps of 50 keV from 200 up to 950 keV energy range. 33 shows the shift on the centroid position as a function of the energy for Compton events arising from the 1173 keV gamma from ^{60}Co source for both detectors.

Both detectors behave similarly over the energy range covered, growing from the back-scatter peak (approximately at 200keV, Figure 24) before having a smooth decay up to the zero reference of the detector, located at 1173 keV. From the graph the smooth time walk curve can be taken care of it during measurements. At the optimal Z value to obtain the best time resolution, 2.5mV, the Compton walk is over 200 ps over 900keV which is excellent in experimental conditions.

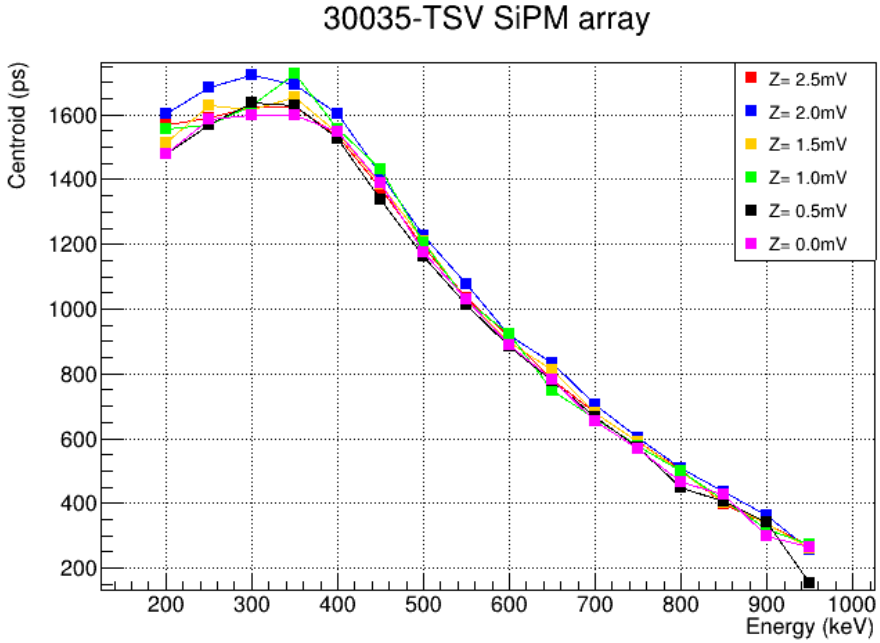

(a)

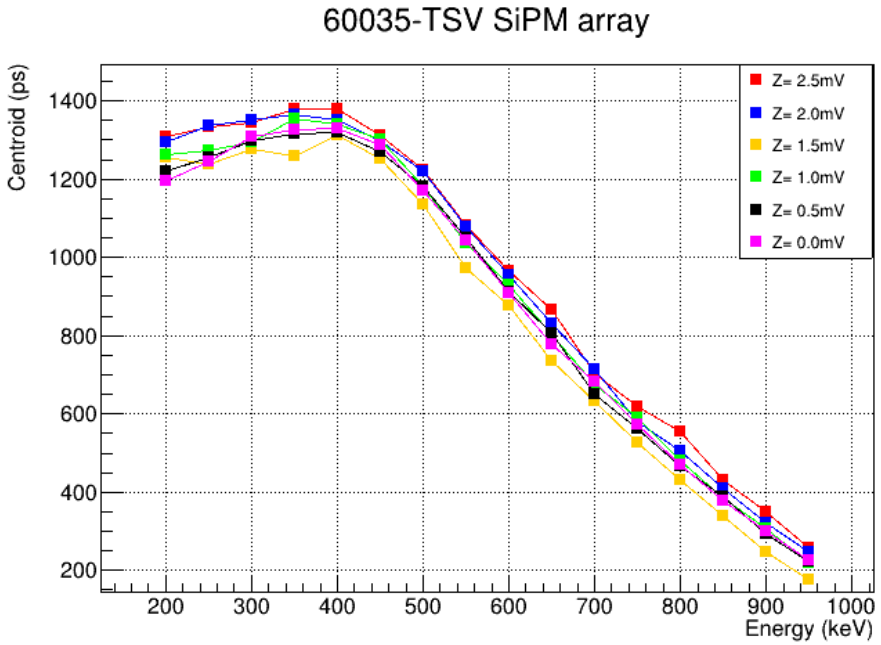

(b)

Figure 33: **Compton time walk for SiPM-based arrays**. **(a)** 30035-TSV array time walk when powered at 32 V for best time resolution and the CFD delay has been set at 5 ns. **(b)** 60035-TSV array time walk when powered at 32 V for best time resolution and the CFD delay has been set at 6 ns. The zero time reference has been given by the position of 1173 keV full energy peak.

3.10 Conclusions and future perspectives

Silicon photomultipliers (SiPM) are increasingly becoming an alternative to the Photomultiplier tubes (PMTs) in fields such as medical imaging or astrophysics to name a few. These sensors have a similar gain and operate on lower voltages, but what makes them unique is their high tolerance to magnetic fields. For this reason, these sensors are seen as a replacement for the PMTs in nuclear spectroscopy, specially at the Institut Laue Langevin (ILL). A γ-ray spectroscopy array, named FIPPS (FIssion Product Prompt γ-ray Spectrometer), is currently being developed and one of the stages will involve the installation of a gas filled magnet spectrometer rendering the conventional PMT a non-optimal choice for fast-timing measurements.

For this reason, two SiPM based-arrays have been developed with their magnetically compatible readout each. Each of the arrays is made of Onsemi 30035-TSV and 60035-TSV sensors. One of the main advantages of these sensors against others is the output of two signals; the standard and the fast output. The proposed readout treats each type coming out of the sensors with a different approach: all the standard outputs coming out of the sensors are added in order to obtain the energy-related information such as energy resolution, efficiency, linearity and gain from the overall array. On the other hand, the fast output of each sensor is grouped in order to obtain the fastest signal, before adding the four first arriving signals coming out of the array. This is done by connecting the fast output to a Schottky diode in series. These diodes, made of the junction between a semiconductor and a metal, have a fast switching speed and allow the pass of the fastest signal arriving into each group.

The performance review has been done by coupling each of the detector to a well tested $LaBr_3$(Ce) truncated cone crystal. This scintillator combines a fast time response with a good energy resolution, making them ideal for fast-timing measurements. The performance of the SiPM based-arrays has been tested against a R9779 PMT coupled to the same scintillator. The PMT is a good choice for fast-timing experiments since it favours a fast response ($\approx$130 ps for ^{60}Co energies) while maintaining a good energy resolution (4.0%) [Ved+17] at ^{137}Cs source energies. In order to characterize the energy response of the detectors, an analog-based experimental set up has been employed to obtain the time distributions from each of the detectors. Each of the detectors has been put against a reference 1 inch $LaBr_3$(Ce) detector.

The characterization of the detectors has been divided into energy and time response. Energy response of the SiPM based-arrays have a similar performance as the R9779PMT tube. From 27 V up to 30 V both arrays display a good linearity while slightly improving the energy resolution. Values of 3.7% and 3.9% were achieved at 29 and 30 V for the 60035-TSV array and 30035-TSV array respectively. After 30V saturation occurs, energy resolution worsens up to 4.3%. The difference on energy resolution comes from the difference on the surface covered by each of the arrays, where the 60035-TSV covers the full area of the crystal while the 30035-TSV only covers up to 65 % of the crystal 17. Both of the arrays display a similar γ-ray

photo-detection efficiency and together with the rest of the performance review completed it can be said that both of the arrays are well suited for γ-ray spectroscopy measurements

Time resolution values are reported and are still far from the one that the crystal coupled to a PMT offers. In order to study the time response of the detectors, a basic electronic set-up has been employed. Each of the detectors has been tested against a well known 1 inch cylindrical $LaBr_3$(Ce). The fast output of the SiPM based-arrays and the negative signal from the PMT are fed into the ORTEC 935 CFD analogue module for a more precise arrival time determination. The time difference has been performed with a fast digitizer [San+19]. Two radioactive sources have been employed during testing: ^{60}Co and ^{22}Na. In order to test the proposed readout several parameters have been optimized. There is no dependence between the V_{diode} and the time resolution, as can be seen in Figure 30. The time walk (Z) and the CFD delays have been optimized by an iterative method. Best intrinsic time resolution is achieved at 32V in both arrays, yielding values of 235(12) and 256(12)ps for 30035-TSV and 60035-TSV arrays respectively. These values are far from the 110(3)ps value obtained when using a fast-timing dedicated PMT tube, but the SiPM detectors cannot be dismissed as a fast detector since yielding a time response of $\approx$ 250 ps can be considered fast. At last, the suggested operating voltage for both of the SiPM based readout has to keep a balance between the energy and time response, which is achieved at 30-31 V. Both of these voltages make the SiPM based-readout perform slightly worse than the best value obtained for the energy response characteristics (3.7% and 3.9% at 29V for 30035-TSV and 60035-TSV arrays respectively) while maintaining a good time response in comparison to the best one obtained for each of the arrays (255ps and 275ps CRT at 32V for 30035-TSV and 60035-TSV arrays respectively).

Although the time and energy resolution results show a promising start for SiPM based-detectors, there is still an area where the detector must be tested: temperature dependency. One of the main drawbacks in semiconductor detectors is the thermal noise generated when thermally excited electrons jump the valence band and generate false pulses, known as dark noise. For this reason, other semiconductor detectors such as HPGe are cooled down to low temperatures, in order to minimize this issue. For a SiPM sensor, this won't be a solution since the goal is to obtain a compact detector with a similar size to the PMT tube. For that reason, a possibility could be to integrate a Peltier [LFA00].

As for the future of this detector, several updates may improve the performance presented on this thesis. As a first version, results show that on the energy response the SiPM is competitive against the PMT. However, the length of the signal derives into dead time and pile up effects hindering the potential of this detector. Making the final standard output shorter should be a priority in the near future. The length of the signal comes from the added capacitance load of every signal summed in parallel added to a long decay time. Since the first reason cannot be changed, the second is the more possible way to fix the problem. Reducing the decay time on the operational amplifiers will reduce the decay time of the signal below the 1μs barrier,

reducing the dead time and pile up effects. Although the fast output coming of the arrays is shorter (500 ns, Figure 21), a shortening of the signal would reduce the dead time issues.

The main focus of upgrading the fast output is the rise time of the signal, being 16 and 20 ns for the 30035-TSV and 60035-TSV respectively, since it's slower than the PMT tube (≈8 ns). For this update, several operational amplifiers are being looked into, with a similar bandwidth and power consumption as the ones used currently but with a better slew rate in order to better preserve the incoming signal rise time. Although this should not be a problem, increasing the gain by a negative factor would help discriminate better the fast output from background noise, allowing a better discrimination when inserted into the CFD delay. This would increase the size of the signal as well as change its polarity, not needing a pre-amplifier in future cases.

Lastly, as can be seen from the review, covering the total crystal surface might not be needed in order to get a competitive energy response but it's paramount in order to improve energy resolution. On the other hand, using smaller SiPMs, which results in a lower capacitance, provides a better time resolution which is paramount for the future of fast-timing techniques. Future updates of this detector could involve manufacturing a custom-made quasi-circular array with the 30035-TSV sensor in order to cover the full area of the crystal while maintaining the time response and improving the energy response.

The developed SiPM-based detectors do not need to be used exclusively to measure γ-rays, but also can detect other radiation such as β radiation. As an example, currently at the Isolde Decay Station (IDS), two SiPM based-arrays with a similar electronic readout are used as β-detectors in order to increase the β-detection efficiency of the experimental setup. The possibility of having β detectors in combination with fast scintillators would give FIPPS access to clean information from the β decay fragments coming out of the fission reaction. Characterizing the coupling of the developed arrays with an organic scintillator could be a way to help scientists arriving into ILL.

4 The FIssion Product Prompt γ-ray Spectrometer at ILL

Thermal-induced fission, which is possible at Institut Laue Langevin (ILL), provides important data for nuclear structure studies and nuclear reactor physics. Many experimental nuclear physics studies take advantage of highly efficient gamma spectroscopy setups based on HPGe arrays. The combination with complementary/ancillary detector systems opens up new possibilities for gamma spectroscopy and nuclear structure research. In 2012, a nuclear spectroscopy campaign was launched at ILL. This campaign, by the name of EXILL (EXogam at ILL) [Jol+15], combined one of the most intense cold neutrons source available with a high efficiency germanium array (EXOGAM) coupled to an ancillary device made of 16 $LaBr_3$ detectors [Jen+17; Bla+13].

Based on the successful EXILL gamma spectrometer campaign at the Institut Laue Langevin (ILL), work on a permanent HPGe array was started as part of the laboratory ENDURANCE program. The idea was to develop the Fission Product Prompt γ-ray Spectrometer (FIPPS) [Mic+18] consisting of a high-resolution HPGe array coupled to a recoil spectrometer based on a gas-filled magnet. The final goal for this instrument is to help with the investigation of nuclear structure of neutron-rich nuclei and the study of the fission process itself.

The ^{130}I studied in this thesis was produced during the 2020 experimental campaign at FIPPS. During this campaign the neutron capture of ^{129}I produced the ^{130}I, observing the decay from the entry level into the ground state. This chapter describes the experimental set-up used to measure the nuclear structure of ^{130}I. FIPPS was configured for fast-timing measurements, employing the 8-segmented HPGe detector array coupled to an ancillary device made of 16 $LaBr_3$(Ce) scintillator detectors. The HPGe detectors are used in the construction of the level scheme of the nucleus as well as provide branch selectivity in order to perform lifetime measurements between $LaBr_3$(Ce) detectors. The lifetime measurements of excited states have been extracted via fast-timing methods (explained in Chapter section 2). In order to reduce the amount of electronic modules needed to implement fast-timing methods a multiplexed-start/multiplexed-stop set up has been implemented, allowing FIPPS to measure lifetimes down to the tens of picosecond range.

4.1 Insitut Laue Langevin (ILL):the H22 neutron guide and FIPPS

Located in Grenoble (France), the Insitut Laue-Langevin (ILL) is an internationally financed research center funded in 1967. The center focuses its research on neutron science and technology. ILL provides one of the most intense neutron sources in the world and the most intense continuous neutron flux worldwide, making it the center for neutron related studies. Neutrons at ILL are fed to 40 state-of-the-art instruments covering a wide range of topics such as molecular, atomic and nuclear structure and dynamics.

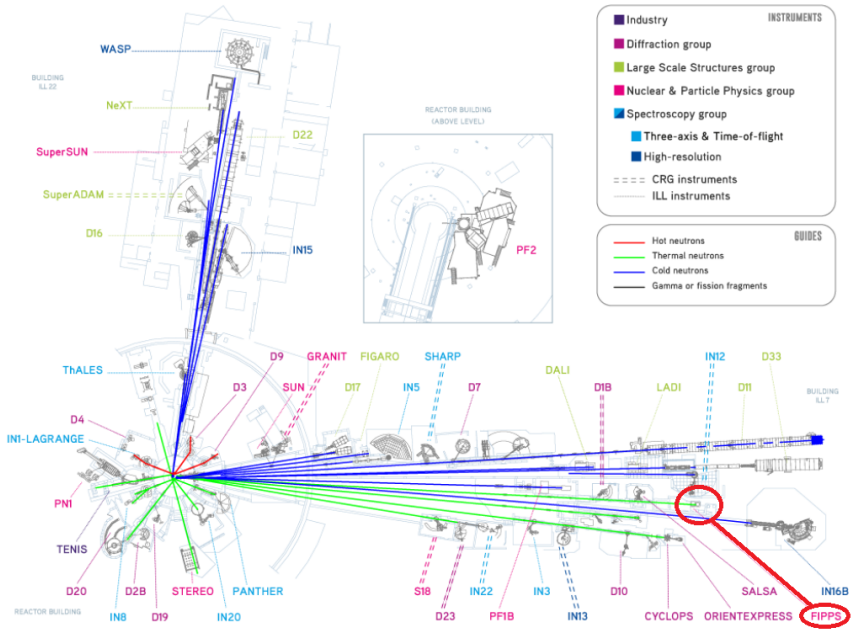

Figure 34: **Instrument distribution at Institut Laue-Langevin**

Data analysed in this thesis was taken during the experiment 81849 carried out in January 2019. The goal was to populate the excited states of ^{130}I via a neutron capture reaction. This fission reaction consisted of the bombardment of a PbI_2 target, and to analyse the fission products using the FIssion Product Prompt γ-ray Spectrometer (FIPPS). This instrument is located at the end of the H22 thermal neutron guide, where the measured flux at 58.3MW reactor power is $7{\cdot}10^8$neutrons$\cdot$cm^{-2}s^{-1} with a diameter of 2cm [Mic+18].

FIPPS is not directly located at the end of the H22 line, since the neutron beam can damage the HPGe detectors. For this reason, the beam must be collimated before arriving at the instrument. The collimation system (which can be seen in Figure 35) corresponds to a series of apertures (10mm, 4x12mm) made from high neutron absorbing materials such as boron carbide. In order to avoid γ-ray background from boron in all apertures, 5 cm lead absorbers are also installed. At the

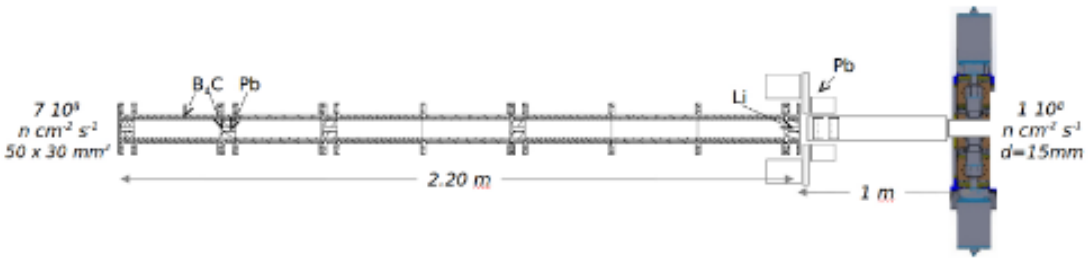

Figure 35: **FIssion Product Prompt γ-ray Spectrometer (FIPPS) setup and collimation system**

end of the line, and close to the experimental set-up, an enriched ^{6}LiF aperture is used to reduce the amount of back-scattered neutrons. The collimation system is inserted in a round vacuum tube system, which is coated with 1 cm-thick borated plastic. The thermal neutron flux at the end of the collimated system is approximately $1{\cdot}10^8$neutrons$\cdot$cm^{-2}s^{-1} with a diameter of 1.5 cm.

4.2 The FIssion Product Prompt γ-ray Spectrometer (FIPPS)

Operational since December 2016, the FIssion Product Prompt γ-ray Spectrometer (FIPPS) allow users at Insitut Laue-Langevin to study nuclear fission and nuclear spectroscopy experiments, in particular the study of neutron rich isotopes. This instrument, located in hall 7 at the end of the H22 neutron guide, is part of the ENDURANCE program. This program is dedicated to improving the performance and long-term potential of the ILL instrument suite. About 30 projects have been delivered or are nearing completion. They include neutron guide systems, new and upgraded instruments, sample environment and data and software services, offering new opportunities and perspectives for science.

The construction of FIPPS is divided into three phases. Phase one, already finished, consisted on the development of an HPGe detector array mounted symmetrically around the target position. During this phase the reaction chamber, the anti-Compton shields and the detector frame has been built. The frame is a non-magnetic structure able to hold 8 HPGe detectors in a vertical plane with angles of 45 degrees with respect to each other. The frame also allows the option to add ancillary detectors (such as $LaBr_3$, X-ray or neutron detectors) to grant the users access to different experimental configurations. The frame can also be coupled to two half spheres in order to hold up to 16 HPGe plus the auxiliary detectors. An image of the FIPPS experimental set up at the end of the phase 1 is displayed at 36.

Currently, FIPPS is on phase 2 of its construction, where the HPGe set up will be complemented with a recoil spectrometer based on a gas filled magnet [Arm+76;

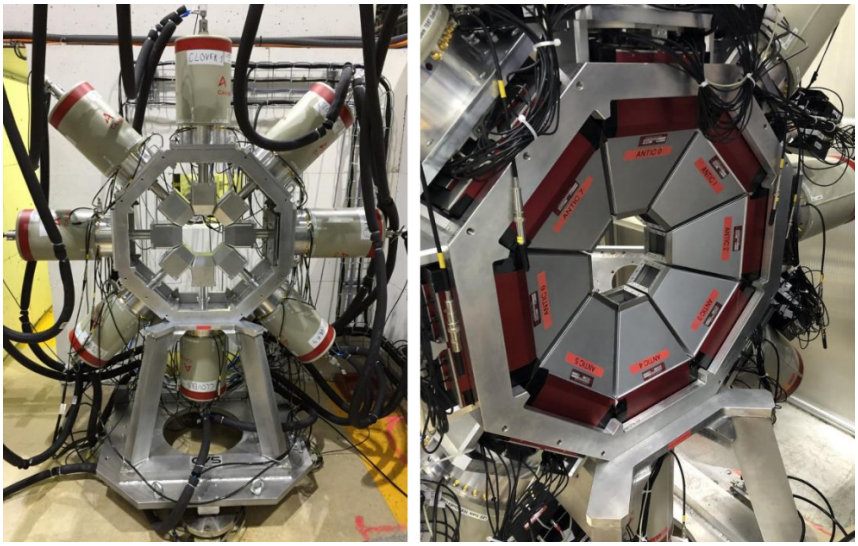

Figure 36: **FIssion Product Prompt γ-ray Spectrometer (FIPPS) setup during phase 1.** Left:Position of 8 HPGe clovers for FIPPS's first experimental campaign during phase 1, image from [Mic+18]. Right: Image of the anti-Comptons set up for FIPPS.

Che+16]. This will increase the sensitivity and selectivity for fission products and nuclear spectroscopy. For fission studies this upgrade will enable to study the correlation between the kinetic energy, the excitation energy and the angular momentum, while for γ spectroscopy it will allow the identification of mass-separated fission fragments, allowing the study of both neutron-rich nuclei and the fission mechanism. The final design will include a 1/r field and a Thales cricle-shaped magnet entrance/exit edges [Kim+20], as it can be seen in figure 38, and is based on magnetic field calculations and Monte-Carlo simulations. Mass resolution is expected around 2% with an acceptance of 3% after the gas filled magnet [Mic+18].

The last phase of the development will consist in a relocation to a new place further down the line H22, since with the addition of the recoil spectrometer the current placement is not an optimal choice. Although FIPPS is currently on its phase 2 of development, measurements of (n,γ) reactions as well as fission measurements are being carried out.

4.2.1 High resolution γ-ray spectroscopy: HPGe detectors

The core of FIPPS is made of 8 HPGe clovers. Each clover was manufactured by CANBERRA and made of 4 High Purity n-type Germanium Crystals with a common cooling device. Each germanium crystal of the clover is 50mm in diameter and 80mm in length before tapering. Each clover is placed in a vertical plane with an angle of 45 degrees among each other.

Anti-Compton shields (ACS) are coupled to each of the clovers and have a modular design that consists of a separated front, side and back shields covering

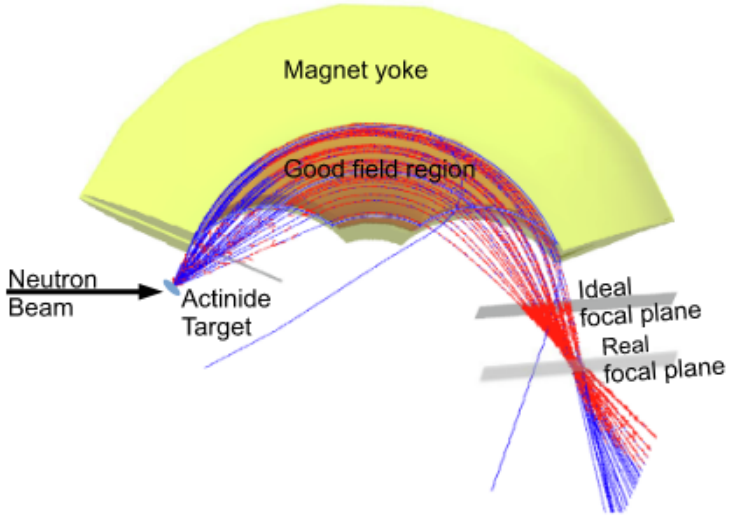

Figure 37: **Simulated trajectories inside the gas filled magnet.** Image taken from [Kim+20]

the full HPGe clover. The front and side crystals are made of Bismuth Germanate (BGO) while the back one is made of cesium iodide (CsI). The front and side BGO are read with Photo-Multiplier Tubes (PMTs) and the back one is read by 4 Onsemi ARRAY-J 60035(4)-PCB (the same as the ones employed to develop the SIPM-based array described on Chapter 3). The design of these ACS allows keeping the configuration of the FIPPS array, and lets the instrument be used in two different experimental set-ups: i) Full suppression mode where all the ACS modules are in use and ii) efficiency mode using only the ACS modules on the side and back. Using the later mode the distance between the Ge-detectors is reduced to 9 cm to the center of the array (at the point of implementation), giving better geometrical efficiency than in the suppression mode.

The full array energy resolution at 1408keV from an ^{152}Eu radioactive source is 2.3keV with a 3kHz count rate per detector, with an efficiency of 3% at the same energy from the singles from ^{152}Eu. The total energy range goes up to 8MeV which is key in fission and neutron capture studies.

4.2.2 Fast-timing measurements at FIPPS: $LaBr_3$(Ce) detectors

In order to perform fast-timing measurements at FIPPS an ancillary device made of 16 $LaBr_3$ detectors has to be integrated into the set-up. These scintillators are similar to the ones described in Chapter 2 but two different geometries were employed: cylindrical and truncated cones. All the crystals were 1.5 inches in height, the diameter of the small bases for the truncated cones ones were 1 inch while the diameter for the big base of the truncated cone and the cylindrical are 1.5inches both. All the crystals were optically coupled to R9779 PMT tubes via silicon grease

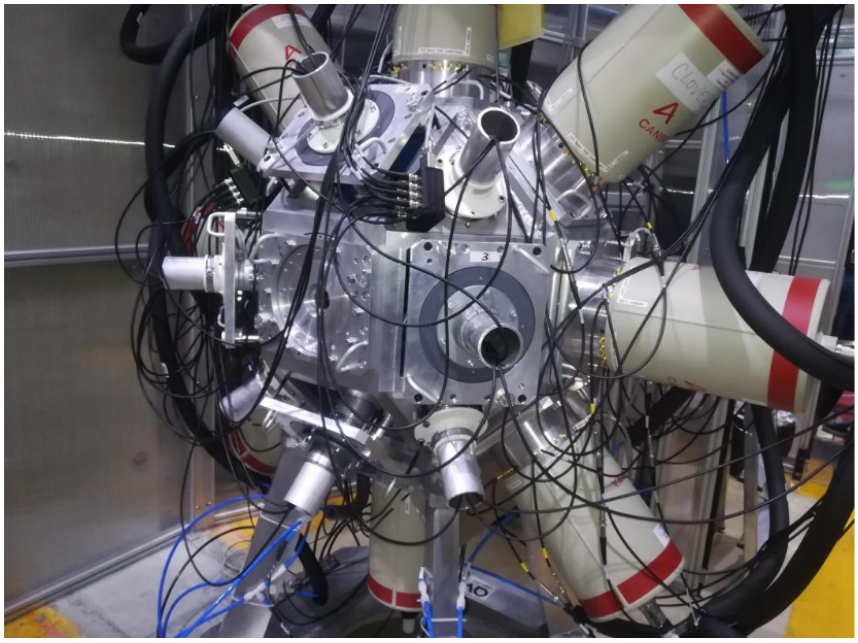

Figure 38: **Experimental set up for fast-timing measurements at FIPPS.**

and wrapped into opaque tape to avoid any outside light. This PMT combines a fast response with a good energy resolution, making it an optimal choice for fast-timing measurements nowadays. Each of the $LaBr_3$ detectors produces 2 signals; a positive signal from the dynode (DY) and a negative signal from the anode (SIG).

4.3 Electronics

The electronic scheme at FIPPS can be divided into two branches: energy and time. The first branch, related to the energy information coming from each detector, carries the signals from the HPGe array into the digital acquisition system. The other one is the timing branch, where the information from the 16 $LaBr_3$ and the timing set up end into the digitizers.

4.3.1 Energy Branch

The energy branch is quite straightforward each of the energy signals are treated prior to entering the digital acquisition system (DAQ). Signals coming from the HPGe clovers are preamplified before arriving into the DAQ, offset and gain are adjusted on this stage. Each of the HPGe clovers is coupled to Anti-Compton shields that are made of 3 modular BGO and CsI crystals as previously described. ACS signals are also preamplified, gain and offset adjusted, before arriving into the DAQ.

The energy information coming from the $LaBr_3$(Ce) detectors come from the dynode (DY) signal. Each of the 16 signals goes straight into the digitizers without

any pre-amplification stage.

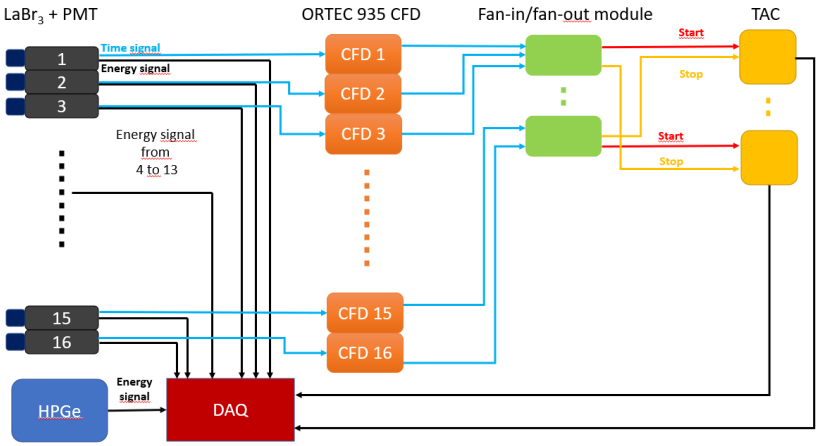

Figure 39: **Simplified electronic scheme for FIssion Product Prompt γ-ray Spectrometer (FIPPS) timing branch**

4.3.2 Time Branch

This branch entails the processing path for the negative signals coming out of the $LaBr_3(Ce)$. The signals are directly fed into an analogue ORTEC 935 Constant Fraction Discriminator (CFD), where the arrival time of every signal was determined by the constant fraction triggering method. The CFD parameters were optimized for the threshold (T) and the zero crossing (Z), setting them at -507mV and +2.0mV respectively. The delay was set up at 2ns for every PMT n the set up. This decision aims to obtain a more stable time walk distribution with the best timing performance.

For large timing arrays, the basic approach for fast-timing measurements is not a realistic choice, since for every combination of two $LaBr_3(Ce)$ a Time to Amplitude Converter (TAC) is needed. For this reason the total amount of channels would be 120 channels which is impractical and cost-intensive. For this reason, the solution adopted was the multiplexing start-stop signals using fan-in/fan-out modules [Rég+16; RDJ18]. The idea behind this method is to divide the detectors into a few groups. Signals coming out of the CFD are grouped and fed either on the start fan-in/fan-out module and other four on the stop fan-in/fan out, as can be seen in Figure 40. The first arriving timing signals into the fan-in/fan out module connected will be the start (i index) for the TAC. The first given timing signal of the other detectors then provides the logic output pulse that is delayed and connected to the stop input of the TAC (j index).

With this technique the signal distribution for each TAC implemented for the analysis is displayed in Table 6. As can be seen on the table several combinations are repeated, these combinations can be excluded during the offline analysis. At

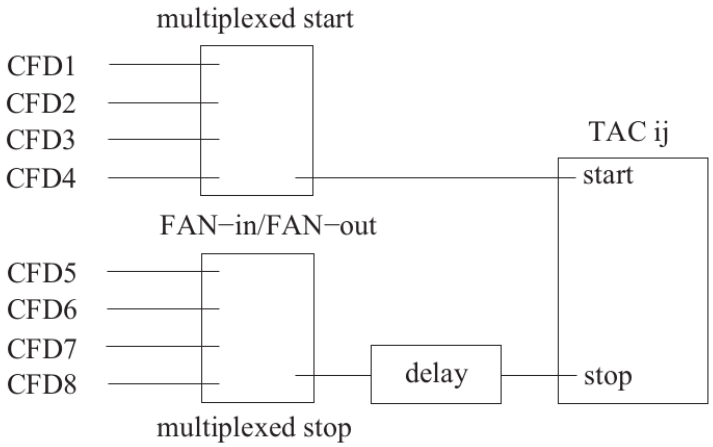

Figure 40: **The multiplexed-start and multiplexed-stop analogue electronics circuitry for large arrays.** Image taken from [RDJ18]

the end, the number of TAC modules employed with this technique is reduced to 8, plus 3 fan-in/fan-out modules, making this approach an excellent way to perform fast-timing measurements in any large timing set up. For this experiment there was no HPGe detector timing set up, for that reason in Table 6 the IDs for those detectors do not appear.

Start input	Stop input	TAC number
0,1,2,3	4,5,6,7	0
0,1,2,3	8,9,10,11	1
0,1,2,3	12,13,14,15	2
4,5,6,7	8,9,10,11	3
4,5,6,7	12,13,14,15	4
8,9,10,11	12,13,14,15	5
0,1,4,5	2,3,6,7	6
8,9,12,13	10,11,14,15	7

Table 6: **$LaBr_3$(Ce) signal grouping employed for multiplexed start-stop technique.** Each of the numbers on the start and stop input corresponds to the number assigned to the $LaBr_3$(Ce) detectors

Output signals coming out of the TAC modules is a quasi-trapezodial pulse whose height corresponds to the time difference between the start and the stop signals. Each of the start-stop combinations can be selected by imposing a condition into the $LaBr_3$(Ce) detectors. The TAC energy signals are fed into the DAQ for their posterior analysis.

Card Channel	Card 1	Card 2	Card 3	Card 4	Card 5	Card 6	Card 7
0	HPGe 0-0	HPGe 4-0	—	ACS 0-1	ACS 4-1	$LaBr_3$ E1	TAC 1
1	HPGe 0-1	HPGe 4-1	—	ACS 0-2	ACS 4-2	$LaBr_3$ E2	TAC 2
2	HPGe 0-2	HPGe 4-2	—	ACS 0-3	ACS 4-3	$LaBr_3$ E3	TAC 3
3	HPGe 0-3	HPGe 4-3	HPGe 7-3	ACS 1-1	ACS 5-1	$LaBr_3$ E4	TAC 4
4	HPGe 1-0	—	—	ACS 1-2	ACS 5-2	$LaBr_3$ E5	TAC 5
5	HPGe 1-1	HPGe 5-1	—	ACS 1-3	ACS 5-3	$LaBr_3$ E6	TAC 6
6	HPGe 1-2	—	—	ACS 2-1	ACS 6-1	$LaBr_3$ E7	TAC 7
7	HPGe 1-3	HPGe 5-3	—	ACS 2-2	ACS 6-2	$LaBr_3$ E8	TAC 8
8	HPGe 2-0	HPGe 6-0	—	ACS 2-3	ACS 6-3	$LaBr_3$ E9	—
9	HPGe 2-1	HPGe 6-1	—	ACS 3-1	ACS 7-1	$LaBr_3$ E10	—
10	HPGe 2-2	HPGe 6-2	—	ACS 3-2	ACS 7-2	$LaBr_3$ E11	—
11	HPGe 2-3	HPGe 6-3	—	ACS 3-3	ACS 7-3	$LaBr_3$ E12	—
12	HPGe 3-0	HPGe 7-0	—	—	—	$LaBr_3$ E13	—
13	HPGe 3-1	HPGe 7-1	—	—	—	$LaBr_3$ E14	—
14	—	HPGe 7-2	HPGe 5-2	—	—	$LaBr_3$ E15	—
15	HPGe 3-3	—	HPGe 3-2	—	—	$LaBr_3$ E16	—

Table 7: **Signal distribution during the experiment 81849 carried out at FIPPS.**

4.4 Digital acquisition system: CAEN 1725 digitizer cards

The information from every signal coming from the HPGe, the ACS, the $LaBr_3$(Ce) and TACs go into the digital acquisition system (DAQ). The DAQ consists of six V1725 digitizer cards linked optically. Input signals are read by a Flash ADC, 14-bit resolution and 250MS/s sampling rate, which is well suited for fast signals like the ones coming out of scintillators coupled to SiPM or PMTs. These cards are also good for slower signals such as the ones from the HPGe detectors. The cards are equipped with a Field Programmable Gate Array (FPGA) that allows a more complex online digital pulse processing (DPP).

Each of the cards has 16 channels and the acquisition can be channel independent and it is possible to make coincidence/anti-coincidence measurements among different channels. The 6 digitizer cards are optically synchronized in order to have a common time of arrival for every measurement. Signals are digitized by a trapezoidal filter [JK94; Jor+94] whose parameters have been optimized for each of the signals.

As can be seen in Table 7 the first 3 digitizer cards allocate the information regarding the HPGe array while the next two focus on the anti-Comptons (ACS). The last two cards are focused on the $LaBr_3$ positive signals which will provide the energy information (hence the Ei assignment) and the TAC time distributions. Data recorded during the experiment is arranged in a list-mode structure containing information about the pulse amplitude, arrival time and detector type.

4.4.1 SOCOv2

Data analysis for 81849 experiment was performed using the SOCOv2 package, developed at the Institute of Nuclear Physics of Cologne (IKP) by N. Saed-Samii [Sae]. It is a C++ based program that allows the analysis of large amounts of data (up to 50TB). It is a command scheme program that allows a full detailed analysis for γ-ray spectroscopy. This program is an open source software and can be updated in order to perform the analysis any user requires.

Some of the capabilities of SOCOv2 are listed below:

- **Timestamps offsets:** since the experimental setup is made of different detectors (HPGe, ACS, PMTs) and each signal has a different electronic path to follow until it reaches the DAQ, the signals arrive at different times to the DAQ. In order to carry out the analysis it is necessary to measure the time offsets between the incoming signals before sorting the events. SOCOv2 includes a tool that measures that time difference between every detector and a reference detector.

- **Event Builder:** in SOCOv2 an event is defined as a set of hits having occurred within a time window. For this reason, a valid configuration of channels as well as several calibrations need to be performed to build the events. Some of these calibrations include timestamp offsets, shift gain tracking and the time coincidence window.

- **Multiplicity:** the definition of the time windows where the event will be based upon. A small window will contain few true events while a large window will include too many random hits. The time window used for this experiment is 200ns for the construction of the different events used on this analysis.

- **Detector gain shifts:** detectors that carry out long period experiments may suffer from gain shifts as a consequence of electronic shifts, temperature changes and high count rates. This affects the energy calibrations, being usable for a few runs. HPGe detectors do not show a significant drift along this type of experiments, the spectra may shift 1 or 2 channels, since they are cooled for the whole duration of the experiment. However, this is not true in case of the $LaBr_3$(Ce) detectors, where gain shift tracking is an important key for the analysis. For this reason SOCOv2 is equipped with a shift-tracker that studies the drift of each single spectra of every run at a fixed position.

- **Gated spectra:** Coincident spectra provide the information that allows the study for the level scheme of interest. By knowing the level scheme of the desired nucleus, gating conditions to measure lifetimes can be placed to obtain nuclear lifetimes. This tool of SOCOv2 provides the projection of every channel given any of the gating conditions.

- **Matrices:** SOCOv2 offers two types of matrices: GG and FT. The first one is a γ-γ matrix that can be used to study the level scheme of interest. Unlike

the gated spectra, add-back reconstruction and Compton suppression conditions cannot be done on the matrix, while on the gated spectra it is possible. The other matrix is the Fast-Timing matrix (FT matrix), which contains the information about the coincident $LaBr_3(Ce)$, and detectors is used to measure the lifetimes from excited levels. This tool's output gives two matrices called "start" and "stop", which correspond to the delayed and antidelayed time distributions described in Chapter 2

The tools described above need several inputs to work which are:

- **Channel configuration file:** this configuration file takes into account the global ID of each detector and their type and corrects the timestamp offset
- **Calibration configuration file:** Every calibration for any given detector employed are described in this file, SOCOv2 allows polynomial calibrations of any degree. For the experiment under the analysis the HPGe, $LaBr_3(Ce)$ detectors and the TAC calibrations are implemented
- **Gate configuration file:** gating conditions are placed here. There are three forms; the detector ID gate file, where gates can be selected to individual detectors, the detector gate file, where all the detectors of one type are gated with the same condition (for this to work a good energy calibration is needed), which is displayed in Table 8. The last type is the add-back reconstruction type.

Gate type	**min**	**max**
HPGE	6015	6023
LABR	184	184
TAC		

Table 8: **Gate configuration file for the detector type gate.**

- **Requirement configuration file:** configuration file that defines the event that needs to be created for the analysis.
- **TAC shift configuration file**: provides the shifts for TAC alignment
- **Exclude configuration file:** contains the detector combinations that should be excluded

5 Nuclear structure of ^{130}I

Neutron rich nuclei with a number of protons and neutrons close to magic numbers are the ideal testing ground for shell model calculations. One of the most interesting regions on the nuclide chart is the one near the doubly magic ^{132}Sn. Nuclei on the region may provide input on the modifications of the shell structure and sudden collective phenomena. This chapter summarizes the investigation of the nuclear structure ^{130}I (Z=53, N=77), since it provides important information of proton-neutron coupling when approaching shell closure. This odd-odd, spherical on principle, can provide key information on collective effects in similar nuclei on the region that come from enhanced quadrupole E2 transitions. The reduced transition probabilities are derived from the lifetimes measured during the analysis.

The experiment under analysis was realized at the FIssion Product Prompt γ-ray Spectrometer (FIPPS) at ILL and populated the ^{130}I excited structure via ^{129}I(n,γ)^{130}I reaction. Thermal neutrons coming from the P22 neutron guide bombarded a PbI_2 target in order to produce both ^{128}I and ^{130}I. The analysis has taken advantage of the 8 high-resolution HPGe detectors from the FIPPS configuration and lifetimes measurements were performed via $\gamma\gamma$ and $\gamma\gamma\gamma$ coincidences between $LaBr_3$(Ce) detectors.

5.1 Previous Work

Not so much is known about the ^{130}I nuclear structure since the main mechanisms populating it are the (n,γ) and the (d,p) reactions, being the ^{129}I the target which is radioactive.

Previous knowledge from these nuclei comes from the work performed by Shakarov et al. [Sak+89] where the nucleus was studied by γ and electron spectroscopy. The ^{130}I was studied in both (n,γ) and (d,p) reactions. The experiments took place in the 80s and were done in several locations such as the Insitut Laue Langevin, Gatchina and the tandem accelerator of the Munich University. The target for all the experiments was a 49 mg KI target 90% enriched with ^{129}I.

A full review of the nuclear structure was obtained via $\gamma\gamma$ coincidences between Ge(Li) detectors allowing the reconstruction of the level scheme from the 10-100

Level energy (keV)	$T_{1/2}$ (ns)	Level energy (keV)	$T_{1/2}$ (ns)
39.9	8.3(10)	606.5	<5
69.5	133(7)	678.4	<1
82.3	315(15)	682.2	<0.6
85.1	254(4)	699.2	<0.8
82.4	66(8)	761.5	<0.6
353.7	<0.1	768.4	<0.8
374.6	<15	804.0	<6
378.3	<0.2	825.0	<4
437.6	<1	876.2	<2
480.7	<0.3	944.9	<6
54.9	<2	1079.0	<3

Table 9: **Lifetime measurements obtained reported in [Sak+89] for the (n,γ) reaction.** Values displayed in the Table come from [Sak+89]

keV range up to 6 MeV. Lifetime measurements were obtained via $\gamma\gamma$ delayed coincidences between the Ge(Li) detectors in the time range of 0-1000ns. Several new lifetimes were obtained for low-lying energy levels, as can be seen in Table 9 and a superior limit was given to higher excited states.

The proposed ^{130}I level scheme had 43 levels and 116 transitions and the parity of the levels was determined uniquely, partially displayed in Figure 41. Most of the (n,γ) levels had an 2-5 spin assignment since those are populated from the (3^+, 4^+) capture state while the levels populated on the (d,p) reaction were all observed in the (n,γ) reaction. At last, the identification of the levels, Table 10, as members of a multiplet was based on the (n,γ) reaction compared to nucleon transfer reaction.

Multiplet	J^Π	Level Energy (keV)	Multiplet	J^Π	Level Energy (keV)
$\pi g_{7/2}\nu d_{3/2}$	2^+	43	$\pi g_{7/2}\nu h_{11/2}$	2^-	–
	3^+	251		3^-	44
	4^+	262		4^-	92
	5^+	0		5^-	111
$\pi d_{5/2}\nu h_{11/2}$	3^-	353		6^-	69
	4^-	296		7^-	180
	5^-	245		8^-	82
	6^-	85		9^-	–
	7^-	–	$\pi g_{7/2}\nu s_{1/2}$	3^+	94
	8^-	–		4^+	49

Table 10: **Excited state identification for particle-hole multiplets**. Data obtained from [Sak+89]

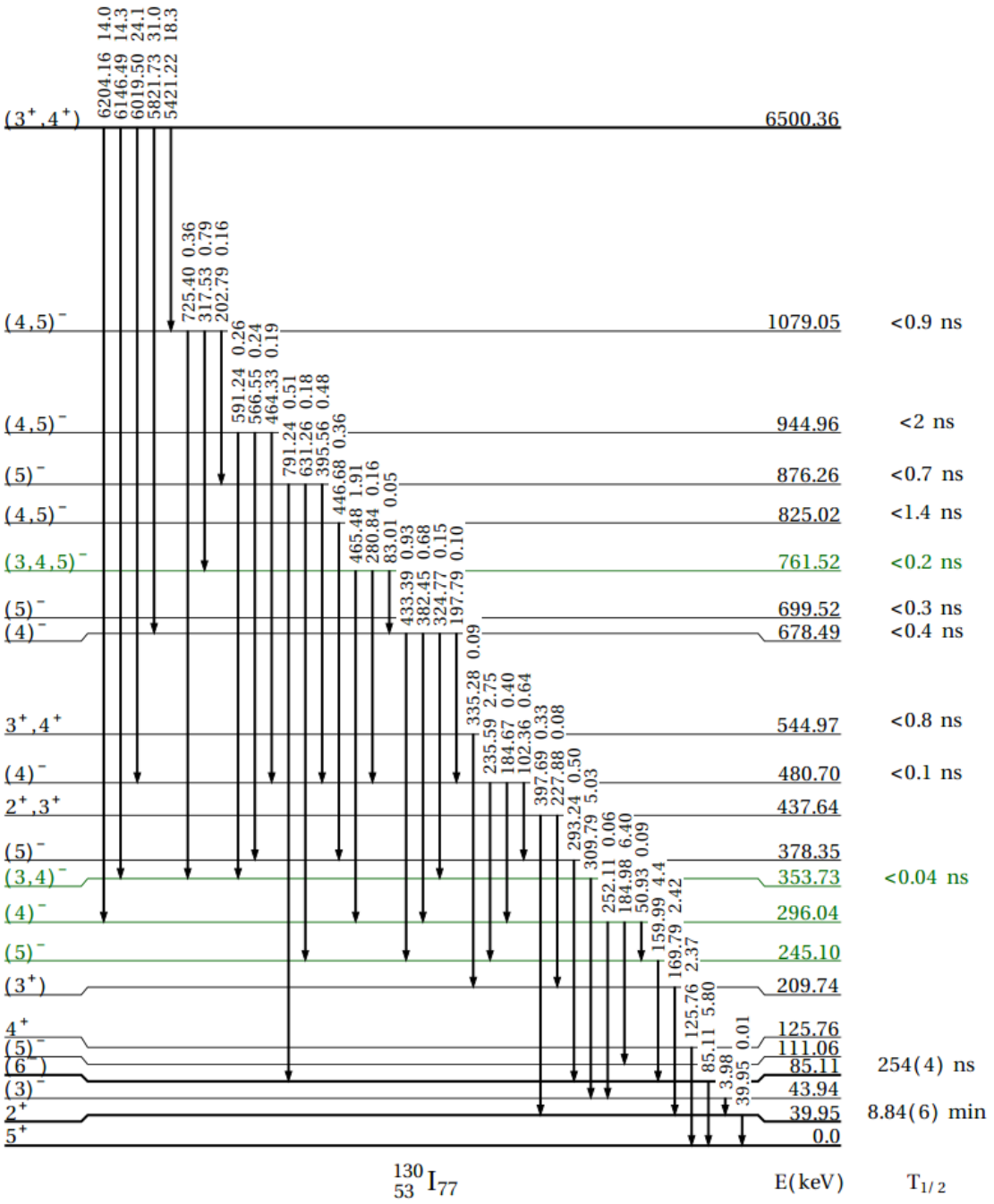

Figure 41: **Partial level scheme of ^{130}I populated in the neutron capture reaction of ^{129}I.** Partial level scheme populated on the ^{129}I(n,γ)^{130}I reaction. Not all the levels or γ-rays are displayed on the figure. The excited states in dark green are the ones with new lifetimes obtained in this work. The first value after each γ-ray corresponds to the energy, while the second number is the intensities per 100 n-captures. Data was taken from [Cen; Sak+89].

5.2 The PbI_2 target

The study of the doubly odd-nucleus ^{130}I nuclear structure is the goal of the experiment 81849. On this experimental campaign ^{130}I was populated via an (n,γ), where the neutron beam impacted into a PbI_2 target. The ideal target would have been a I_2 target but this was ruled out due to its radiological hazard, volatility and reactivity. For that reason, the PbI_2 was considered as a good compromise since lead has a low capture cross-section and the compound is mechanically more stable. The production of the target is described in [Nog+06], and the final product has a complex mass composition involving: natural and radioactive iodine (≈3% and 17% respectively), lead (≈54%), oxygen (≈15%), sulfur (≈6%), nitrogen (≈1.2%), sodium (≈0.75%) and hydrogen (≈0.09%). The amount of iodine is divided into two isotopes being 20% ^{129}I and 80% made of ^{127}I. The (n, γ) cross-sections are 6.15 and 30.4 barn, respectively [Nog+06], therefore almost 80% of the captures will happen in ^{129}I and ≈30% in the ^{128}I.

5.3 The construction of the Prompt Response Difference (PRD) for fast-timing measurements

In order to study the lifetimes by using the centroid shift for $\beta\gamma$ or $\gamma\gamma$ the energy response of the system has to be studied which comes in the form of the Prompt Response Difference (PRD). The PRD curve is built by measuring the difference between the delayed and the anti-delayed time distributions. The delayed time distribution is obtained on the Time to Amplitude Converter (TAC) when the γ ray feeding the level is selected as the start and the stop is given by the γ-ray de-exciting the level. The anti-delayed distribution corresponds to the opposite situation, where the γ ray populating the level is placed on the stop and the de-exciting γ-ray is placed on the start.

In order to build the PRD curve well-known sources are needed. In this analysis the radioactive sources employed were the ^{152}Eu, ^{49}Ti and ^{187}W, each of these sources targets a specific energy range in order to have a wide energy ranged PRD curve. The ^{152}Eu source allows the calibration on the 240-1300 keV which often is sufficient for fast-timing experiments but for this analysis a higher energy must be studied, hence the ^{49}Ti radioactive source, which neutron capture allows for the 137-6760 keV range. To study the energy dependency at lower energies, the ^{187}W source has been proven to be rather effective since it uses low γ-ray energies [Rég+20]. Partial level schemes for the nuclei are displayed in Figure 42.

In order to construct the PRD curve, the first step is to set a fixed gate on a γ-ray populating or de-populating a given state, while the corresponding gating condition is set on coincident transitions of different energies. For every energy combination of coincident transitions, the centroid difference $\Delta C(E_\gamma)=C(E_\gamma)_{stop} - C(E_\gamma)_{start}$ is measured. If the excited level between the transitions has a well known lifetime the PRD centroid must be correct by $PRD=\Delta C(E_\gamma) - 2\tau$.

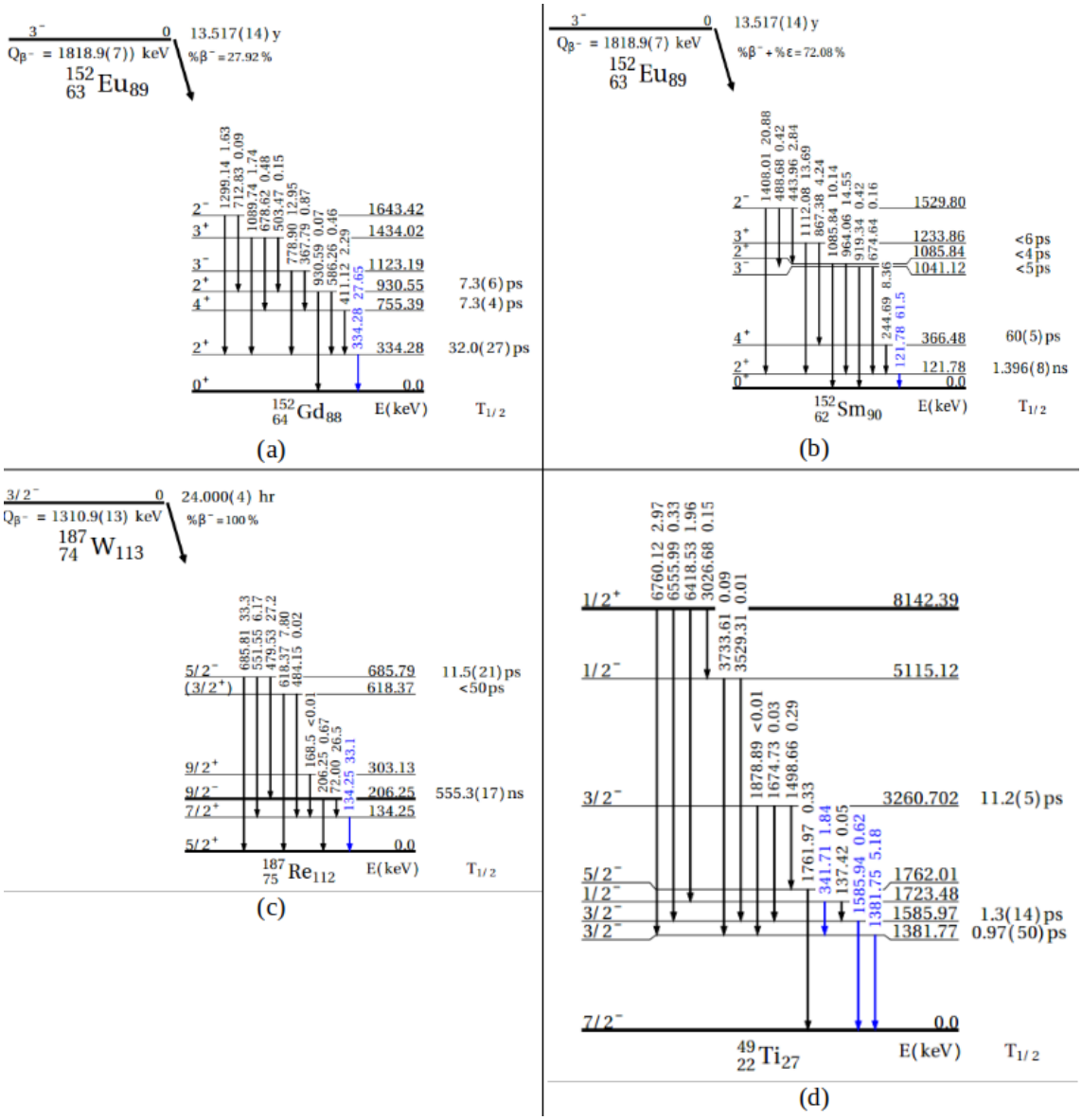

Figure 42: **Partial level scheme of the nuclei employed in the construction of the PRD.** Partial level scheme of nuclei used to construct the PRD curve. (a) and (b) represent the level scheme of ^{152}Gd and ^{152}Sm populated on the β-decay and electron capture of an ^{152}Eu source, respectively. (c) displays the level scheme of ^{184}Re, which is populated on the β-decay of ^{184}W. Lastly, (d) represents the level scheme of ^{49}Ti produced on ^{48}Ti(n,γ) reaction. Reference transitions for the construction are displayed in blue for all the nuclei. The first value after each γ-ray corresponds to the energy, while the second number is the intensities per 100 n-captures (in case of ^{49}Ti) or 100 parent decays (in case of ^{152}Gd and ^{152}Sm and ^{184}Re). Data was taken from [Cen].

The particularity of ^{152}Eu source is that has two decaying branches: the β-decay branch to ^{152}Gd and the electron capture to ^{152}Sm, as can be seen in Figure 42 (a) and (b) respectively. On the first decaying mode, the 344 keV γ-ray has been selected as the fixed gate since populates the ground state and it's in coincidence with 5 other γ rays that directly feed the first excited level. On the other hand, the 444 keV transition has been selected as the decaying branch in the electron capture to ^{152}Sm since at least three transitions are in coincidence. All the PRD obtained from the^{152}Eu decays must be corrected, since the excited levels that are selected have well known lifetimes. The 2^+ excited stated de-populated by the 344 keV has a lifetime of 46.2 (2.5)ps, while the (2^-)state de-populated in the electron capture has a lifetime of 1.6(2) ps.

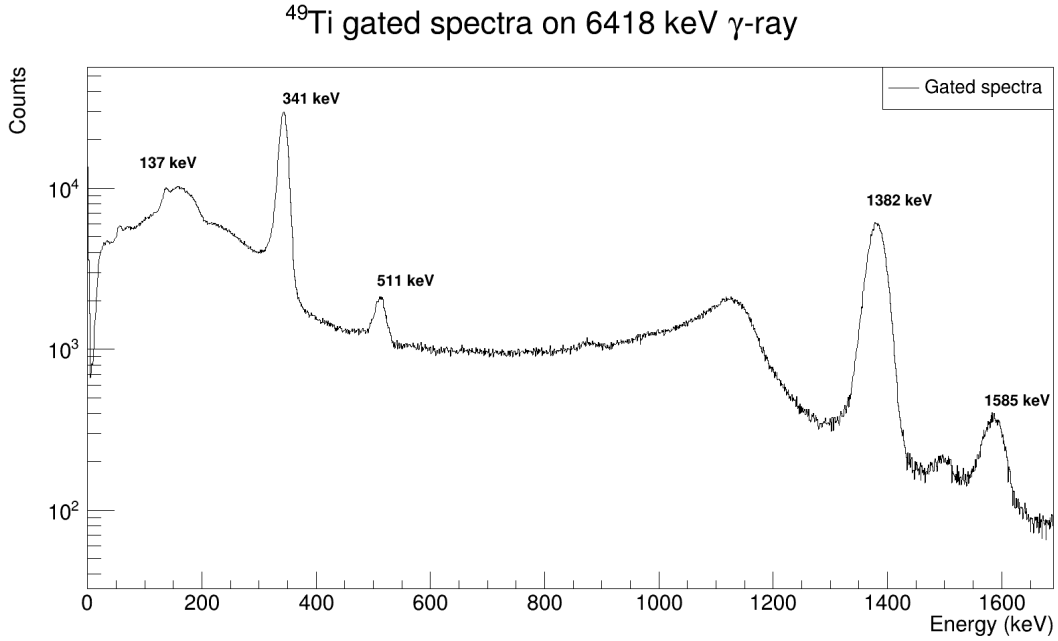

Figure 43: **Coincident $LaBr_3$(Ce) spectra of ^{49}Ti gated by placing a gate in the 6418-keV transition on the HPGe detector**. The relevant peaks, except the 511 keV, employed for the construction of the PRD curve with this source have been identified.

In order to achieve an energy-dependence calibration for higher energies, the ^{49}Ti nucleus is employed, which is produced in the ^{48}Ti(n,γ)^{49}Ti reaction. One of the advantages of using this nucleus is that only prompt levels are populated, so there is no need to apply any lifetime correction. Another thing in favour of the use of this source is the existence of an 342-keV γ ray which still serves as a reference for most of the gammas and provides a merging point with the PRD curve obtained with the ^{152}Eu data, which relies on the 344-keV γ ray. Contrary to ^{152}Eu, where only double $LaBr_3$(Ce)-$LaBr_3$(Ce) events are needed, the ^{49}Ti level scheme (Figure 42 (d)) requires the use of triple events by implementing a HPGe-detector coincidence

in order to allow for a better γ-ray selectivity. The 6418-keV γ ray has been selected for this procedure, allowing for a better gate selection for the 137- and 342-keV γ ray selection, making it possible to study the 137-1586 and 342-1382 keV cascades, as can be seen in Figure 43. By using double coincidences among scintillator detectors, a gate was selected on the 1382 and 1586 keV γ-rays in order to obtain the PRD values for the mid-high energy range γ rays that feed directly to those levels, fully covering the 1382-6760 keV energy range.

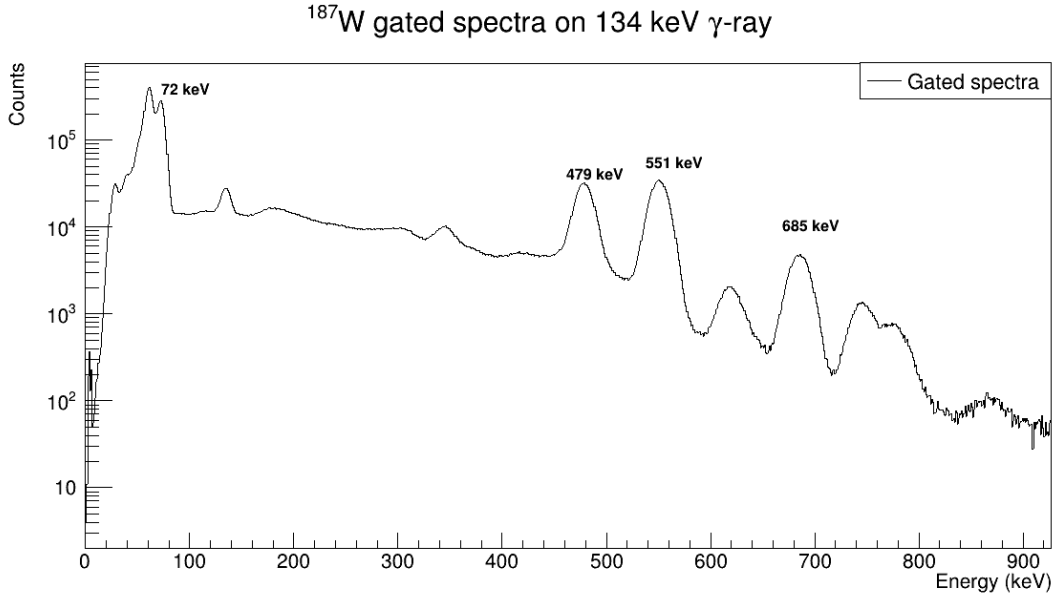

Figure 44: **Coincident $LaBr_3$(Ce) spectra of ^{187}W gated by placing a gate in the 134 keV transition on the HPGe detector**. The relevant peaks employed for the construction of the PRD curve with this source have been identified.

The other calibration source employed is ^{187}W, whose β decay populates ^{187}Re. The level scheme is also complex, but grants access to a lower energy range, from 70 up to 500 keV. The use of double $LaBr_3$(Ce)$-LaBr_3$(Ce) events to access the γ rays in the region is enough in this case. The transitions under study come from the decay of the 134-keV excited state, which is prompt and therefore does not require lifetime corrections.

Once the PRD curve is obtained, the PRD correction of any given γ ray can be obtained by interpolation or by a fit to a function. In the latter case, the centroid difference value of the PRD for a given γ ray under study is provided by the equation:

$$PRD(E_\gamma) = \frac{a}{\sqrt{b+E_\gamma}} + cE_\gamma + dE_\gamma^2 + e \tag{16}$$

where a, b, c, d and e are free fit parameters. The term $\frac{a}{\sqrt{b+E_\gamma}}$ takes into account the charge-sensitive time walk for low amplitudes <400 mV (amplitude dependent

slope of CFD signal at zero crossing). The next term is a polynomial to describe the time for larger amplitudes >400 mV. Often a linear term is sufficient, but in this case a higher order polynomial has to be used since the time walk at very large amplitudes >3 V becomes smaller, most probably due to the non-linear energy-amplitude relation we can observe in the region 3-8 MeV.

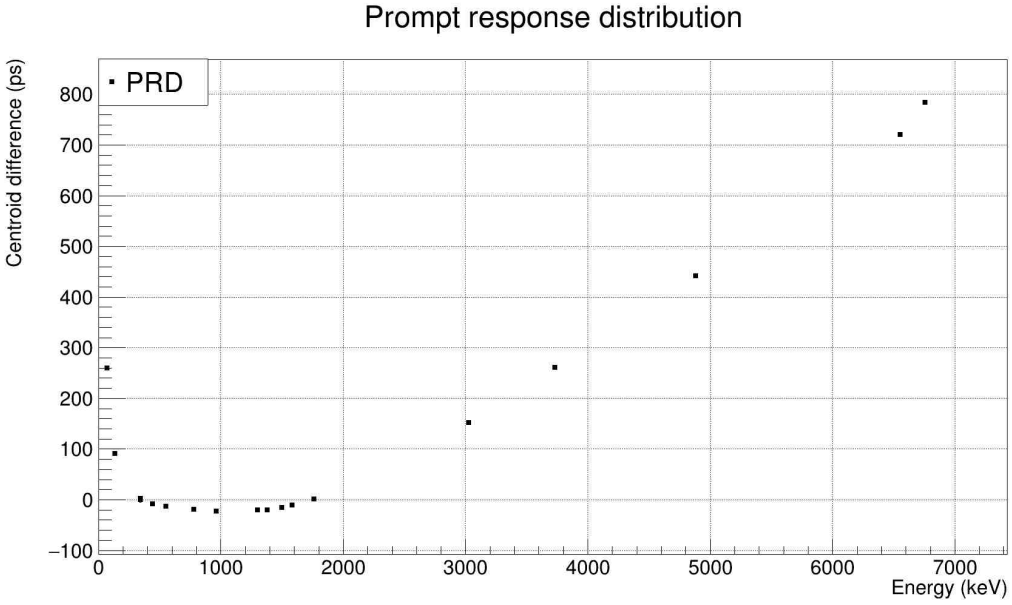

Figure 45: **PRD curve for the data analysis of ^{130}I.**

The PRD curve obtained from the analysis performed in this chapter is displayed in Figure 45. In order to extract the more precise values for the PRD, the data obtained has been fitted to equation 16 in two separate regions, from 70 up to 2 MeV (without the x^2 which is a term heavy influenced at high energies) and from 1MeV up to 6MeV, where the x^2 term is relevant. This is done since the fit is better for each region than when one energy range is used. Table 11 shows the calibration parameters employed for each of the regions.

Range	**a**	**b**	**c**	**d**	**e**
0 up to 1.5 MeV	1922(112)	-45.9(2.1)	$3.44\text{x}10^{-3}(4)$	-	-118.8(8.0)
1 up to 7MeV	$-2.47\text{x}10^{4}(4)$	$1.87\text{x}10^{5}(7)$	$7.06\text{x}10^{-2}(2)$	$9.65\text{x}10^{-6}(3)$	-87.6(1.1)

Table 11: PRD calibration parameters for the regions from 0 up to 2 MeV and from 1 up to 7 MeV

The overall PRD uncertainty is calculated with equation 17, where PRD_{exp} is the experimental-measured value and $\text{PRD}(\text{E}_{gamma})$ is the calculated value according to equation 16.

$$\sigma = \sqrt{\frac{1}{n-1}\sum(PRD_{exp} - PRD(E_\gamma))} \quad (17)$$

The overall PRD uncertainty is 10 ps for the 3σ limit. The PRD curve has been tested by (re)measuring the ^{152}Eu lifetimes. The lifetimes measured agree within a 10 ps uncertainty.

5.4 Lifetime measurements

The structure of the odd-odd nucleus ^{130}I (Z=53, N=77), in the vicinity of the ^{132}Sn (N=82) shell closure, is sensitive to the coupling of the proton and neutron single particle configurations, and to the evolution of proton orbitals above Z=50 when approaching the N=82 shell closure. The expected proton-neutron multiplets in ^{130}I arise from the shell-model configurations in the region, with neutrons below N=82 and protons above the Z=50 gap. Their origin is the coupling of the proton $\pi g_{7/2}$ and $\pi d_{5/2}$ configurations with neutrons occupying the $\nu s_{1/2}$, $\nu d_{3/2}$, and $\nu h_{11/2}$ single particle orbits.

The study of the level scheme of the ^{130}I has been performed via $\gamma\gamma$ and $\gamma\gamma\gamma$ coincidences, but it yields no new excited levels nor new transitions compared to the previously published work, where a similar population method was employed. For this reason, our focus has been to extract lifetimes from excited states in order to obtain reduced transition probabilities. Since the level scheme proposed by Shakarov *at al.* [Sak+89] is rather complex (partially displayed in Figure 41), the use of triple coincidences is mandatory in order to obtain clean spectra for lifetime measurements. For this analysis, only the HPGe-$LaBr_3$(Ce)-$LaBr_3$(Ce) coincidences have been employed, using the centroid shift difference method explained in Chapter 2. The most intense γ rays de-populating the entry level have been gated on the HPGe detectors, while the $LaBr_3$(Ce) have been employed to measure lifetimes below the $(5)^-$ excited state located 876 keV above the ground state.

5.4.1 Lifetime measurement of the (3,4,5)$^-$ level at 761 keV

The $(3,4,5)^-$ excited level is located at 761 keV excitation energy. The only γ ray that populates the state with 317- keV energy comes from the 1079-keV level. For this reason, a gate placed in the 5421-keV transition that populates the 1079-keV level has been selected on the HPGe detector. In order to extract the lifetime of the level, the depopulating γ ray can be chosen to be either the 280- or the 465-keV transitions. The latter has been chosen since with 280-keV γ ray is not clearly resolved in the triple coincidences, as can be seen in Figure 46.

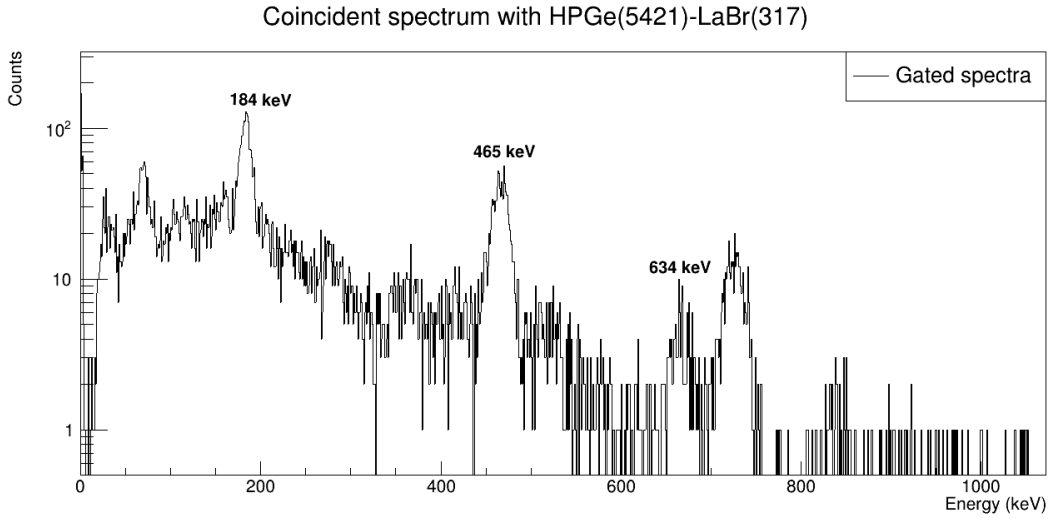

Figure 46: **Coincidence spectrum for HPGe(5421)-LaBr$_3$(317) combination.** The coincident spectrum represents the depopulation of the (3,4,5)$^-$ level at 761 keV. As displayed, the 280-keV transition depopulating the level is not resolved.

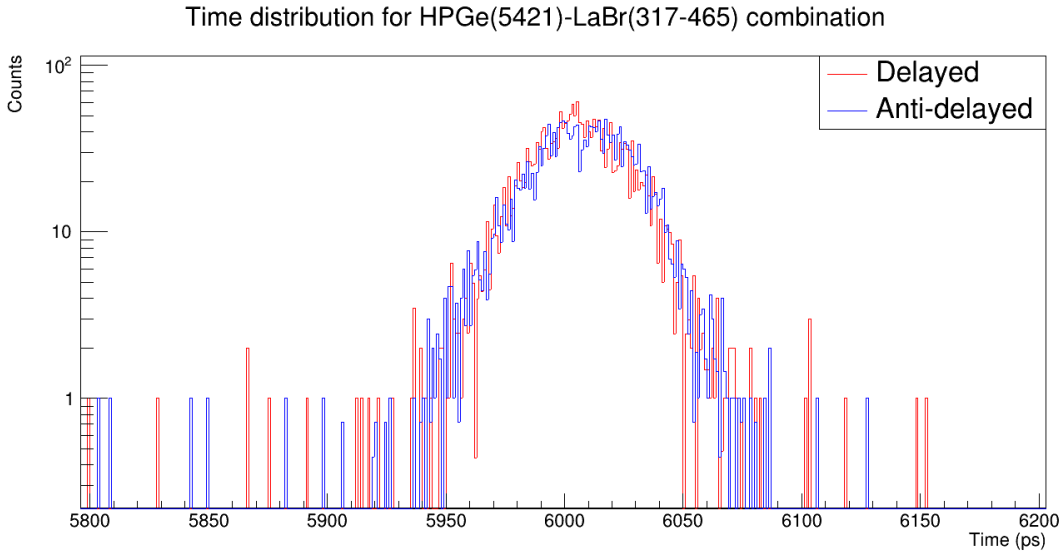

Figure 47: **Delayed and anti-delayed time distributions for the (3,4,5)$^-$ excited level.**

The delayed and the anti-delayed time distributions differ by few ps, as can be seen in Figure 47. Once the PRD is applied, the half-life obtained for centroid shift is T$_{1/2}$=10(12) ps, which is at the limit of the technique employed. For this reason, this half-life can be seen as a one-sigma upper limit of T$_{1/2}$ $\leq$21 ps.

HPGe (keV)	$LaBr_3$(Ce)-$LaBr_3$(Ce) (keV)	ΔC (ps)	ΔPRD (ps)	τ (ps)
5421	317-465	-9.6(8.4)	18(15)	14(12)
	317-280	280 keV is not resolved		

Table 12: **Lifetime measurement of the $(3,4,5)^-$ level at 761 keV.** A gate is placed on the HPGe detector in order to provide extra selectivity. The lifetime measurement comes from the $LaBr_3$(Ce)-$LaBr_3$(Ce) transition, where the first γ-ray is the feeder while the latter one is depopulating the level of interest.

5.4.2 Lifetime measurement of the $(3,4)^-$ level at 353 keV

The excited level located at 353 keV with a $(3,4)^-$ parity assigned could be studied from two different cascades. The first cascade employed is 5421-725 keV γ-rays, the 5421 keV has been selected by gating the HPGe detector and the 725 keV γ-ray has been selected in the $LaBr_3$(Ce). In order to extract the lifetime of the level, the second $LaBr_3$(Ce) gate has been placed in the 309 keV γ-ray, which is the only depopulating known transition, as displayed in Figure 48. Another way to study this lifetime is with the 5821-324keV cascade, by selecting the 5821 keV γ-ray that depopulates the entry level on the HPGe and gating in the scintillator $LaBr_3$(Ce) detector the 324 keV γ-ray that directly feeds the excited level. However, there are not enough statistics on this transition to extract the lifetime.

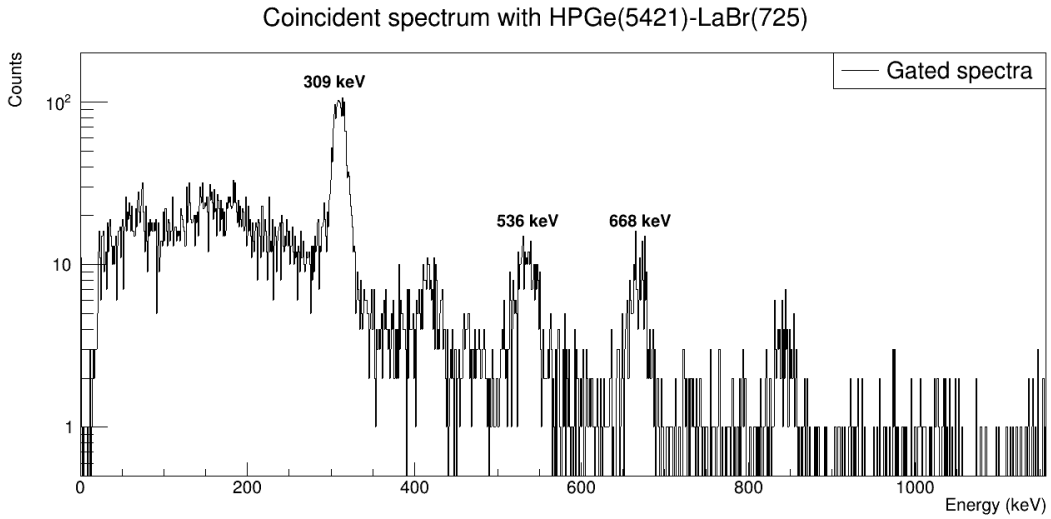

Figure 48: **Coincidence spectrum for HPGe(5421)-$LaBr_3$(725) combination.** The coincident spectrum represents the depopulation of the $(3,4)^-$ level at 353keV. The 309 keV γ ray is the only way to depopulate the level. 536 and 668 keV γ-rays come from the daughter nucleus ^{130}Xe, populated on the β-decay of ^{130}I

The delayed and the anti-delayed time distributions for the 5421-725 keV cascade is displayed in Figure 49. The final half-life provides a final value of $T_{1/2}$=23(10)

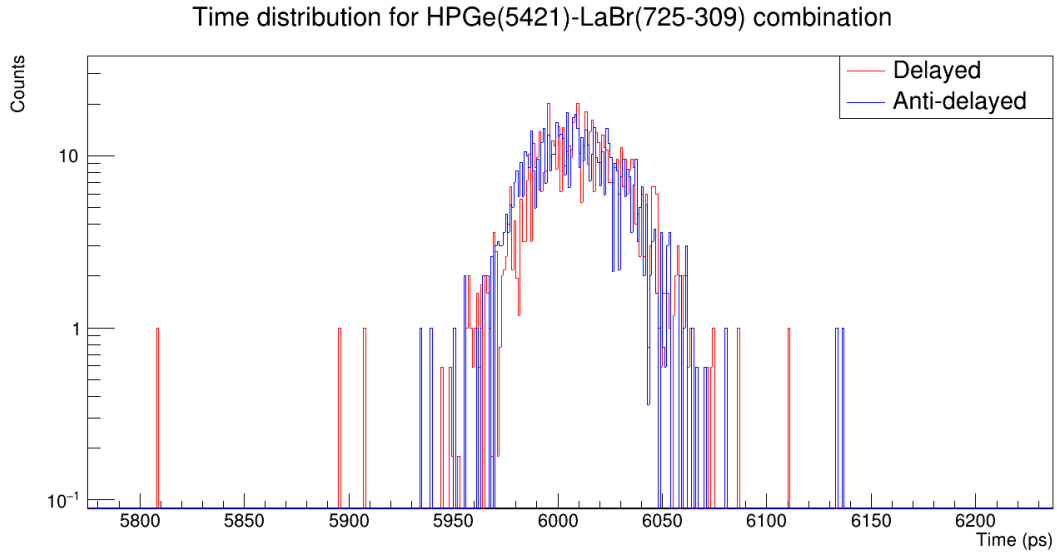

Figure 49: **Delayed and anti-delayed time distributions for the$(3,4)^-$ excited level.**

HPGe (keV)	$LaBr_3$(Ce)-$LaBr_3$(Ce) (keV)	ΔC (ps)	ΔPRD (ps)	τ (ps)
5421	725-309	36.7(14.0)	-30.3(14.3)	33.5(13.9)
5821	324-309	not enough statistics		

Table 13: **Lifetime measurement of the $(3,4)^-$ level at 353 keV.** A gate is placed on the HPGe detector in order to provide extra selectivity. The lifetime measurement comes from the $LaBr_3$(Ce)-$LaBr_3$(Ce) transition, where the first γ-ray is the feeder while the latter one is depopulating the level of interest.

ps, which is a new measurement for the excited level.

5.4.3 Lifetime measurement of the $(4)^-$ level at 296 keV

The $(4)^-$ excited level is located 296 keV from the ground state. The lifetime of this level has been obtained via triple coincidences between a HPGe detector (for γ selectivity only) and 2 $LaBr_3$(Ce) detectors. There are several transitions that populate this level, the most intense ones are the 317-465, 5821-382 and the 6019-184 keV cascades. The HPGe gate selection has been done for each of the cascades in the first γ-ray mentioned (317,5821 and 6019 keV respectively) and the first $LaBr_3$(Ce) has been placed on the 185 keV γ-ray that depopulates the level which is the most intense.

The delayed and the anti-delayed time distributions for the HPGe(6019)-$LaBr_3$(184-184) transition are displayed in Figure 51. As can be seen, the lifetime is long enough as to appear as a slope on the distribution. For this reason, the slope method has

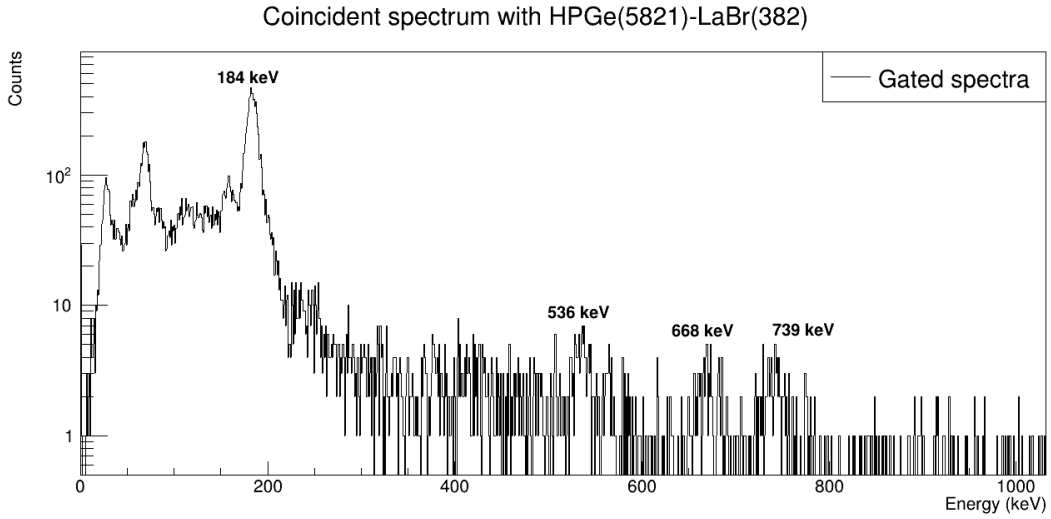

Figure 50: **Coincidence spectrum for HPGe(5821)-LaBr$_3$(382) combination.** The coincident spectrum represents the depopulation of the $(4)^-$ level at 296 keV. Depopulating γ-ray of 184 keV is clear, but the 204 and 252 keV transitions are not resolved.

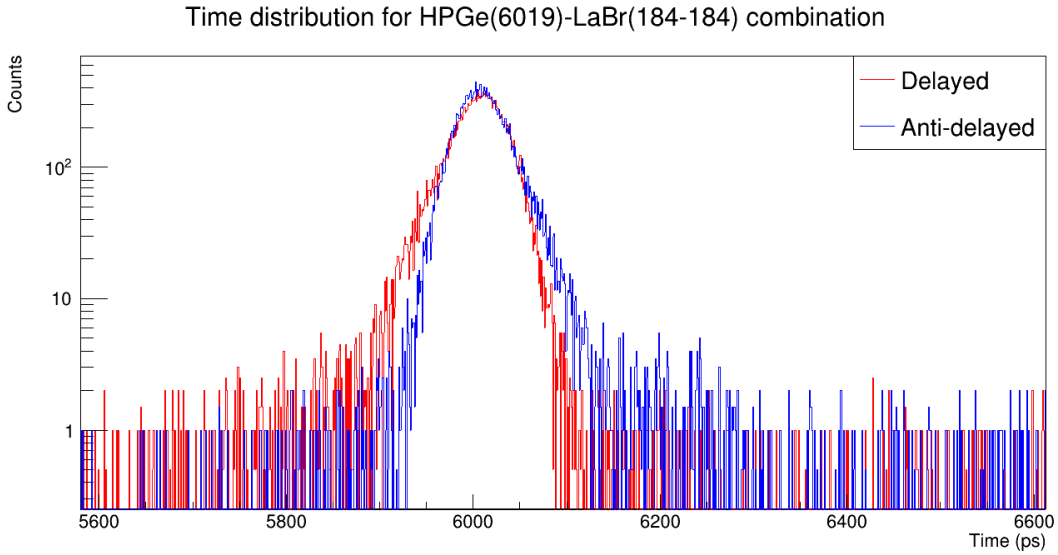

Figure 51: **Delayed and anti-delayed time distributions for the $(4)^-$ excited level.**

been employed. The final half-life is the weighted mean of all the half-lives obtained from the above mention transitions, for a final value of $T_{1/2}$=129(6) ps, which is a new measurement for the excited level.

5.4.4 Lifetime measurement of the $(5)^-$ level at 245 keV

The $(5)^-$ excited level is located 245 keV from the ground state. The two γ-ray that populate this level are the 235 and 433 keV γrays coming from the 678 keV level. In order to employ the first γ-ray, a gate on the 6019 keV γ-ray has been placed on the HPGe detector in order to populate the $(4)^-$ level that is depopulated by the 235 keV transition. In order to use the 433 keV γ-ray, a gate selected the 5821 keV transition that populates the 678.5 keV level has been selected on the HPGe detector. In order to extract the lifetime of the level, the de-populating γ-rays selected can be either the 153 or the 159 keV transitions. A wide gate with both of them has been employed to obtain more statistics, at the cost of an increased background.

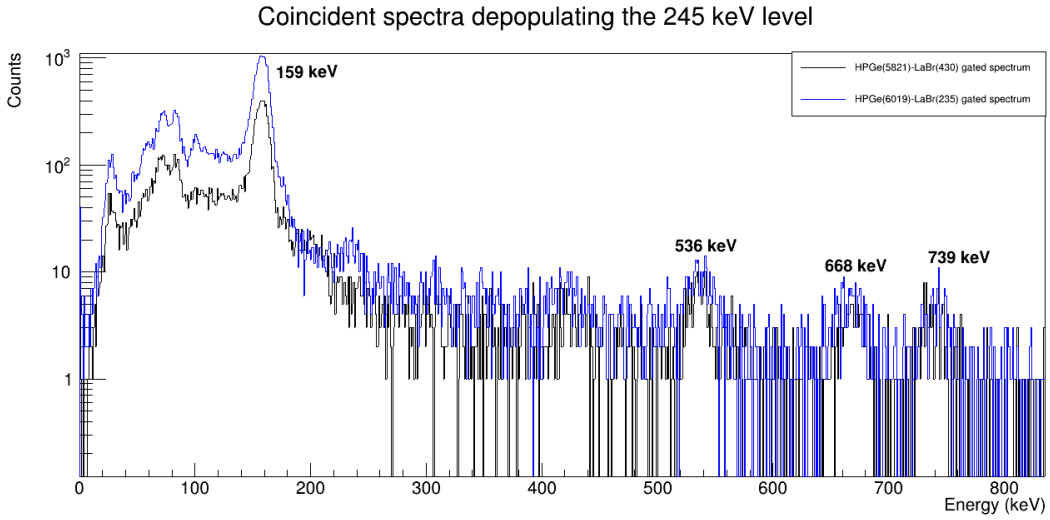

Figure 52: **Coincidence spectrum for HPGe(5821)-$LaBr_3$(430) and HPGe(6019)-$LaBr_3$(235) combinations.** The coincident spectra represent the depopulation of the $(5)^-$ level at 245 keV. As displayed, the 153- and 159-keV γ-rays depopulating the level are not resolved, for that reason, a wide gate has been selected.

HPGe (keV)	$LaBr_3$(Ce)-$LaBr_3$(Ce) (keV)	ΔC (ps)	ΔPRD (ps)	τ (ps)
5821	433-(153+159)	70.4(8.8)	-72.9(16.7)	71.7(13.3)
6019	235-(153+159)	53.7(4.7)	-37.8(17.6)	45.8(12.9)

Table 14: **Lifetime measurement of the $(5)^-$ level at 245 keV.** A gate is placed on the HPGe detector in order to provide extra selectivity. The lifetime measurement comes from the $LaBr_3$(Ce)-$LaBr_3$(Ce) transition, where the first γ-ray is the feeder while the latter one is depopulating the level of interest.

The delayed and the anti-delayed time distributions are displayed in Figure 53. The weighted mean half-life obtained from both lifetimes obtained via the centroid

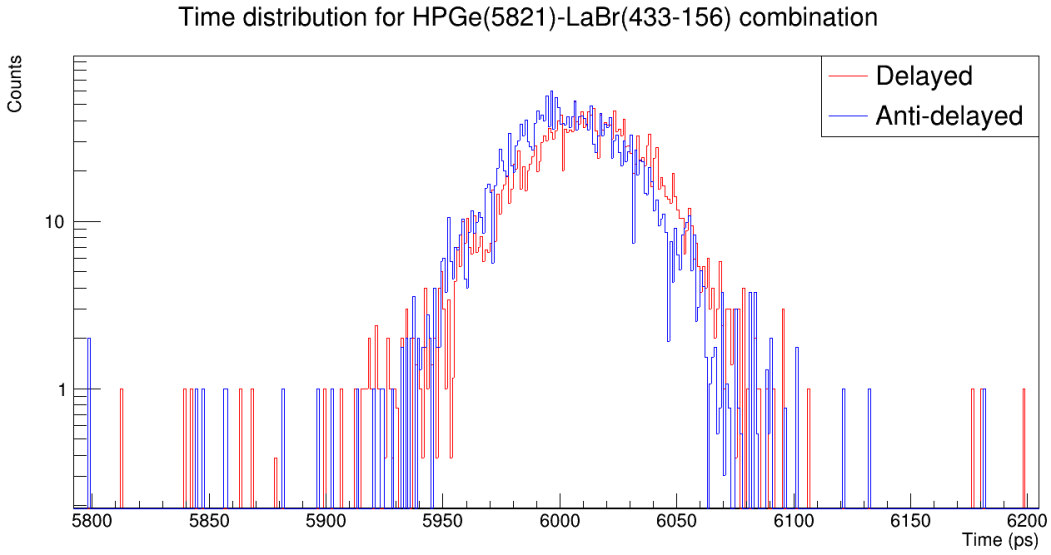

Figure 53: **Delayed and anti-delayed time distributions for the $(5)^-$ excited level.**

shift method is $T_{1/2}$=41(11) ps, which is a new value for the level.

5.5 Reduced transition probabilities

The corresponding B(Xλ) have been calculated for all ^{130}I lifetimes measured. Calculations are derived from the lifetimes obtained in this work and the branching ratios obtained in [Sak+89], as well as theoretical internal conversion coefficients, calculated using BrIcc [Uni]. Results are displayed in Table 15.

J_i^Π	E_i(keV)	$T_{1/2}$	J_f^Π	E_f(keV)	E_γ(keV)	I_γ(%)	Xλ	B(λL) (W.u.)
$(3,4,5)^-$	761.5	<10(12)	$(4)^-$	296.0	465.5	1.9(1)	M1	>1.94x10^{-2}
							E2	>5.90x10^{1}
$(3,4)^-$	353.7	23(10)	$(3,4)^-$	43.9	309.7	5.0(2)	M1	3.11x10^{-2}
							E2	2.13x10^{2}
$(4)^-$	296.0	129(6)	$(5)^-$	111.1	184.9	6.4(3)	M1	1.79
$(5)^-$	245.1	41(11))	$(6)^-$	85.1	159.9	4.4(3)	M1	8.68x10^{-2}

Table 15: **State half-lives and reduced transition probabilities in ^{130}I**. Intensities are given per 100 N-captures.

From the result, an M1 behaviour is more likely for the 465.5 keV transition, although the lifetime is below the precision of the technique employed to obtain the lifetime, so it is proposed as a limit to keep in mind for future measurements. Three new lifetimes have been measured and the reduced transition probabilities have been

calculated, the three decays display a M1 dominant behaviour. The three levels with new lifetimes are the 241.4, 296.0 and the 353.7 excited states are proposed to be part of the $\pi d_{5/2}\mu h_{11/2}$ in [Sak+89] multiplet, the M1 transitions obtained favour this decision.

5.6 Conclusions and future outlook

The focus of this chapter was to measure the nuclear structure of ^{130}I populated via ^{129}I(n,γ)^{130}I reaction. The experiment took place in the beginning of 2019 and a PbI_2 target was bombarded with thermal neutrons arriving at the H22 neutron guide.

The instrument employed to measure the product of the (n,γ) reaction was the FIssion Product Prompt γ-ray Spectrometer (FIPPS) . This high-resolution γ spectrometer is made of 8 HPGe detectors segmented in four clovers each that allows for precise γ spectroscopy measurements. The core of FIPPs was coupled to ancillary device made of 16 $LaBr_3$(Ce), in order to reduce the amount of analog module electronics, in order to per from fast-timing measurements, a multiplexed-start/multiplexed-stop set up was installed.

Prior investigations of the ^{130}I populated via (n,γ) and (d,p) reactions where performed in the 80s constructing the currently known level scheme and studying the lifetimes of excited states on the low energy region (10-100 keV) via Ge(li)-Ge(Li). This research, performed by Sakharov et al. [Sak+89] also gave upper limits for a wide range of levels (Table 9) that cannot be accessed via slow timing techniques as well as identifying memebers of the multiplets .

During the analysis performed on this chapter, no new γ-rays or exited states have been measured with double, triple or quadruple coincidences between the HPGe detectors. ON the other hand, three lifetimes have been extracted for the first time and one level has an upper limit. The lifetimes extracted from the data analysis come from the region between 49 and 876 keV, the higher region requires more statistics to be able to select the desired γ de-populating the entry level on the $LaBr_3$ detectors.

Three new lifetime measurements have been extracted from the analysis performed and a limit has been placed into another lifetime. The first new lifetime is from the $(3,4,5)^-$ level located 761 keV above the ground state. This half-life yields a value of $T_{1/2}$=9(12) ps, and has been extracted from the HPGe(5421)-317-280 keV γ-ray transition. This half-life value is on the limit of the technique employed,so its been set as an upper limit for the half-life of the excited level.

A new lifetime for the $(3,4)^-$ excited level at 353 keV has been obtained via centroid shift methods. Two cascades were employed in order to extract the lifetime of the level: HPGe(5421)-725-309 and HPGe(5821)-324-309. The final half-life for this level has been given the final value of $T_{1/2}$=24(9) ps coming from the weighted mean from the values obtained on both cascades.

The half-life of the $(4)^-$ excited level at 296 keV has been obtained for the

first time via the slope fit method. Three cascades where employed to extract this lifetime which are: HPGe(317)-465-185, HPGe(5821)-382-185 and HPGe(6019)-184-185. The final value for this half-life has been obtained from the weighted mean from each of the cascades and time distributions (6 in total) for a final result of $T_{1/2}$=129 (6) ps.

The half-life of $(5)^-$ excited level at 245 keV has been measured for the first time with the centroid shift method. In order to extract the half-life of this level, the two cascades under studied are the ones coming from the 5821 and 6019 keV cascades. Both of the cascades employed are HPGe(5821)-235-(153+159) and the HPGe(6019)-678-(153+159). The γ selected to de-excite the level is the combination of two (153 and 159 keV γ-rays)since the $LaBr_3$(Ce) detectors cannot resolve each of them. The final half-life has a value of $T_{1/2}$=45(13) ps.

Reduced transition probabilities have been obtained from the newly extracted half-lifes. The 245, 296 and 353 keV display a strong M1 transition which supports the theory that the three levels are part of the $\pi d_{5/2}\mu h_{11/2}$ multiplet as suggested in [Sak+89]. The limit placed into the 761 keV level suggest an M1 transitions as well.

The nuclear structure for the ^{130}I nuclear structure populated via ^{129}I(n,γ)^{130}I reaction has been performed, although the level scheme has not been expanded with new levels and transition from previous work [Sak+89], several lifetimes have been added to the level scheme. With those new half-lifes the reduced transition probabilities have been obtained and displayed a clear tendency towards M1 transitions, that indicates a more single particle behaviour of these nuclei.

5.6.1 Potential of investigating the β decay of ^{130}Xe to excited states in ^{130}I

The population of ^{130}I via the ^{129}I(n,γ) reaction using a long-lived ^{129}I target holds a very strong potential of the structure of the stable nucleus ^{130}Xe populated in the β-decay of ^{130}I, with $T_{1/2}$=12.36(1) h. The difficulty of studying the ^{130}I β decay stems from the populating mechanisms, which basically reduce to the neutron capture employed in this work, the (d, p) transfer reaction on ^{129}I and the (p, n) reaction on ^{130}Te. That is the reason why most of the available information on the level structure of ^{130}Xe comes from the work by Hopke *et al.* [Hop+73], where they measure the decay of ^{130}I, ^{130m}I and ^{130}Cs with a couple of Ge(Li) detectors.

It is worth mentioning that ^{130}I has found use in nuclear forensics and the nuclear fuel cycle due to the fact that it is strongly produced in fission, but its population can only take place directly and not from the β decay of other neutron-rich fission fragments, since the decay is blocked by the quasi-stable ($T_{1/2}$=$10^2$0 y) ^{130}Te isobar. This property can be used to assess fission yields for different systems, but then a thorough knowledge of the decay properties, including γ intensities will be required. In comparison to [Hop+73], a later publication [Mus+95] shows strong discrepancies in certain γ intensities.

The β decay of ^{130}I to ^{130}Xe has been recently investigated in [Mat+22] where

^{130}I was produced in a (p, n) reaction. Twenty-five new levels have been added to the previously known level scheme from [Hop+73; Mus+95] via γ-γ coincidences by employing 49 Compton-suppressed HPGe detectors. However, no lifetime measurements of excited states were performed. For this reason, a full review of the β-decay of ^{130}I to ^{130}Xe will be possible in the future with the available data from our work, with special attention to excited-level lifetimes, which will help to understand the structure of this stable nucleus. In particular, the 2_1^+-state lifetime has been reported to be τ=14.6(14) ps from a recent Coulomb excitation experiment [**Morrison2020**], and other state lifetimes may become accessible.

6 Experimental campaign IS610 at ISOLDE

One of the motivations behind this thesis is the study of neutron rich nuclei ^{130}Sn produced during the IS610 experimental campaign. During this campaign, the β decay of ^{130}In populating the tin nucleus has been studied. In order to study this reaction, the radioactive ion beam (RIB) made of ^{130}In was obtained via ISOL techniques. This method consists on the reaction between light particles (such as protons or neutrons) and a thick target, in this case made of UC_x. The exotic isotopes generated from nuclear reactions (such as fission, spallation or fragmentation) are extracted from the target chamber area via chemical reactions. After this, the RIB is accelerated and transported to the experimental area where it can be studied in detail.

The IS610 campaign had two experimental runs between 2016 and 2018 at ISOLDE (CERN) with the main focus of populating tin isotopes in order to study the area near the doubly magic nucleus ^{132}Sn. Data from the IS610 experimental campaign regarding the ^{130}Sn isotope is studied in this research. Calibrations performed by Dr. Jaime Benito [Ben] have been employed during this analysis. This chapter focuses on the ISOLDE facility and the IDS station technical decays, as well as the analysis procedure.

6.1 ISOLDE: from PSB to the IDS

The Isotope mass Separator On-Line facility (ISOLDE) is one of the experimental infrastructures within the CERN complex and focuses on nuclear and particle physics experiments. Experiments performed on this facility range from antiproton matter or hadronic structure studies up to neutron rich nuclei structure studies. At ISOLDE, radioactive nuclei are produced via spallation, fission, or fragmentation reactions. This is done by irradiating a thick target with a proton beam coming from the Proton Synchroton Booster (PSB) at an energy of 1.4 GeV with an intensity up to 2μA. Chemically selective mechanisms are used to release the nuclear reaction products from the high temperature target into an ion source where they are retrieved as a radioactive ion beam that frequently reaches the highest inten-

sities on the planet. Further selection is possible and, in some situations, a beam produced in a specific isomeric state is possible to produce when certain chemical elements are subjected to laser ionization. High intensity radioactive beams with a high isotopic and frequently isobaric purity are recovered from this one-of-a-kind production unit by use of strong mass separators. The wide range of species that are available enables the exploration of the atomic and nuclear characteristics of nuclei far from the stability line.

After the production phase, the isotopes thermally diffuse out of the target into the ion source. Different techniques are used to ionize radioactive materials as they move such as surface ionization, laser ionization, and electron impact ionization. One of the main features of ISOLDE is the Resonant Ionization Laser Ion Source (RILIS) [Fed+17]. RILIS is made of wavelength-tunable lasers that allow, in a multistep process, to ionize the desired elements before leaving the cavity giving RILIS a precise Z-selectivity. Thanks to this fine selectivity RILIS offers extremely efficient isobaric separation. These lasers allow RILIS to cover wavelength range from 210 to 950nm. The target's diffused atoms are effused in the direction to a hot cavity, where they are kept in a gaseous condition. This is maintained until the atoms are ionized.

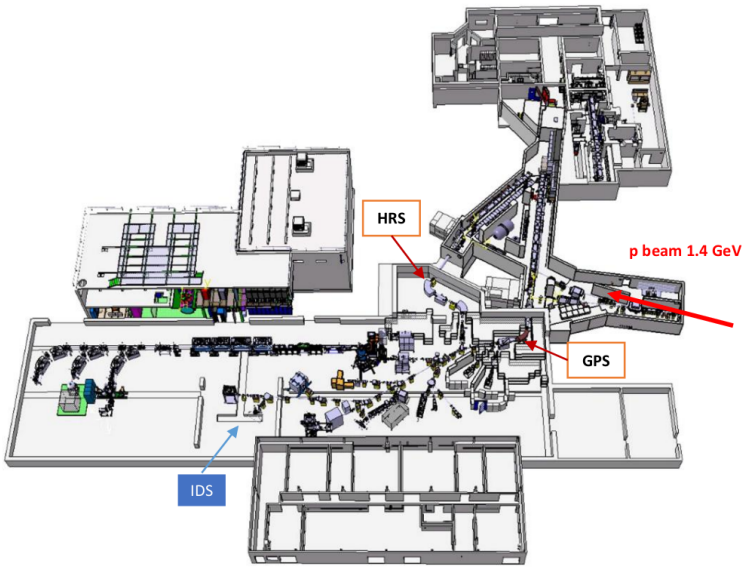

Figure 54: **Schematic layout of ISOLDE.** Image taken from [Cat+17]

Besides the element selectivity provided by RILIS, an isomer selectivity can also be implemented. This possibility results from the interaction with the angular momenta of the nucleus, which causes the hyperfine separation of the atomic transitions utilized for resonance ionization. To obtain such selectivity, the differences on the hyperfine structure must be greater than the width of the excitation resonances in the hot cavity in order to distinguish the isomers. Our experiment was one of the

first where RILIS was used to selectively enhance the ionization of a given isomer for a detailed spectroscopy study.

Once ionized and isobarically separated, isotopes are extracted into the beam line with a 30 to 60 kV potential applied between the target and the end point of the line. The transfer from the target to the beam line can be controlled by an electrostatic detector called the beamgate. While the beamgate is closed, it prevents ions from entering the beam line, and it is open it allows them to continue through the beam line. The beam gate's open time interval and the delay before opening are two factors that can be changed to increase the ratio between the desired isotope and its contaminants. To prevent the released short-lived isotopes from the target from entering the beam line, it may be held shut for a few milliseconds after the proton. From here, the ion beam goes through one of the isotope separators.

As showed in Figure 54, ISOLDE has two different isotope separators; the General Purpose Separator (GPS) and the High Resolution Separator (HRS). GPS consists of a double focus magnet of 70% with a 1.5 m mean radius curvature that enables three ion beams in the 15% mass range from the central mass to be selected and directed simultaneously to three different experimental locations. To either side of the beam line are two pairs of cylinder-shaped deflector plates. Mass selection is achieved by moving these deflectors parallel to the focal plane. These smaller beam lines are mostly employed in nuclear and solid state physics for ion collection or small experimental setups. On the other hand, the HRS is composed of two C-type dipoles (the first of 90° and the second of 60°), which deviate directly the beam in opposite directions. With this, HRS guarantees a resolving power higher than GPS, with an M/ΔM of 5000 (up to 10000) in working conditions.

The central beam line merges with the exit from the HRS beam line in a merging switch yard. After the merging, beam distribution resides on a 3-way or 5-way (depending on the separator employed) switchyards and quadrupole lenses. It's up to the users to tune and monitor the arrival of the beam into the desired instrument optimizing the path to lose the least amount of beam possible. In the case of this experiment, the beam is directed towards the Isolde Decay Station (IDS).

6.2 The IDS: ISOLDE Decay Station

The ISOLDE Decay Station (IDS) [IDS] began its operation in 2014 and it is a fixed set-up dedicated to decay studies using a radioactive ion beam from ISOLDE. Located in a low background area of the facility, the main set up of this instrument consists of up to six HPGe clover type detectors for γ-ray spectroscopy. Depending on the radiation under study, the IDS has the capability to couple auxiliary devices to provide a deeper understanding of different isotope decays or to address specific experimental needs.

The data analysed for this thesis was obtained during the IS610 experiment carried out in 2016, the first of the two campaigns of the experiment. For this campaign the IDS was using its fast-timing configuration, consisting of two $LaBr_3$(Ce)

detectors and a fast-plastic scintillator in order to perform lifetime measurements. The end goal of the IS610 experiment was to measure both sides of the doubly magic ^{132}Sn nuclei, populated by the β decay of ^{132}In.

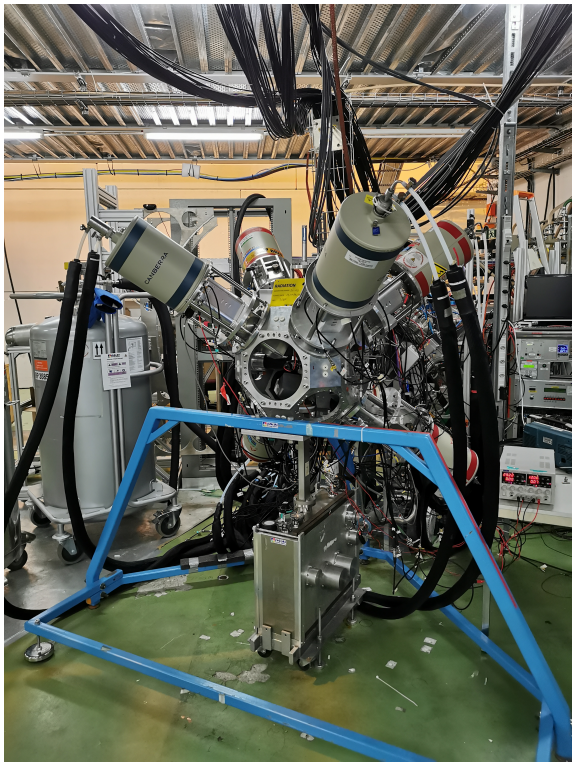

Figure 55: **IDS set up as of 2022.** The more recent set up involved on the IS610 was similar but without 2 HPGe-clover type detectors

A picture of the current setup can be seen in figure 55. The set of detectors forming the IDS are surrounding the implantation point in order to measure β and γ radiation coming from the indium decay. Inside a vacuum chamber, indium ions are implanted into an aluminized moving tape. The movement of the tape is controlled either manually or by a step-by-step motor system. This movement is crucial in order to prevent long-lived activity of daughter nuclei or contaminants. The IDS experimental set up can be divided into two branches: energy and time. The energy branch corresponds to the information carried by four HPGe clover type detectors in order to perform γ-ray spectroscopy. The time branch collects the information from both of the fast scintillator detectors and the beta detector, and its goal is to measure lifetimes of excited sates using the Advanced Time delayed $\beta\gamma\gamma$ and the Generalized Centroid Shift techniques.

6.2.1 γ-ray spectroscopy at IDS: HPGe detectors

At the time of the experimental campaign, four Canberra EUROGAM clover type HPGe detectors were the core of the IDS set up. This clover-type detectors are

used for high resolution γ-ray spectroscopy and are made of four HPGe crystals each. All the 4 crystals are inside a cryostat in order to control its temperature and reduce possible contaminants. In total, each detector is 70mm long and has a 50mm diameter.

These detectors yield an excellent energy resolution of 1.95(5) FWHM at 1332 keV, from a ^{60}Co source. Once add-back reconstruction is done, energy resolution goes down to 2.11(5)keV and the total relative efficiency is around 120%. On the time response side, HPGe detectors are rather slow to perform lifetime measurements in the ps range, since their time resolution is about 5 ns FWHM for each crystal at ^{60}Co energies besides suffering from a strong walk dependence. However, these detectors can be used for measuring lifetimes from the nanosecond up to the millisecond range.

For these reasons, HPGe detectors are used to obtain the spectroscopic information for the experiment via $\gamma\gamma$ coincidences and will be used to study longer lifetimes, in the order of the μs range. In addition, these detectors play a role in fast-timing measurements since a better selectivity can be achieved when a selective condition (also known as coincidence gate) is placed on a HPGe spectra.

6.2.2 Fast timing at IDS: Beta and $LaBr_3$(Ce) detectors

For fast-timing measurements, three detectors are employed: one beta detector and two $LaBr_3$(Ce) detectors. The combination of these detectors will provide the timing information necessary to study lifetimes of exotic nuclei. As previously mentioned (Chapter 3), $LaBr_3$(Ce) detectors are the standard detectors for fast-timing techniques since their development. With a better energy resolution than its predecessor, the BaF_2 detector, combined with a fast response, made these detectors an alternative to study lifetimes in exotic nuclei.

During the IS610 campaign two truncated conical LaBr3 (Ce) doped crystals were used for timing measurements. Both of the crystals are 1 inch in height and with diameter bases of 1 and 1.5 inches. This geometry has been chosen since it gives a better γ-ray efficiency while maintaining a fast time response. Testing was carried out by V. Vedia in [Ved+17]. Both of the crystals were optically coupled to R9779 PMT tubes. These phototubes are the standard choice for fast-timing experiments due to their excellent timing capabilities as well as spectroscopic features. Both of the $LaBr_3$ yield a 110ps intrinsic time resolution at ^{60}Co energies and have a 4% energy resolution at 662keV. Both detectors were placed at roughly 10mm from the implantation point at an angle of 86^{o} degrees in order to minimize the interference with the HPGe and β detectors.

Concerning the β detector, an ultra-fast EJ-232 plastic scintillator was used. The reason behind this selection is straightforward; β energy spectra is a continuum, hence, energy resolution is not a priority in fast-timing measurements although energy selection is of use. For this reason, the β detector has two purposes, on one hand it allows for a β gate on the γ measurements with the HPGe detectors allowing

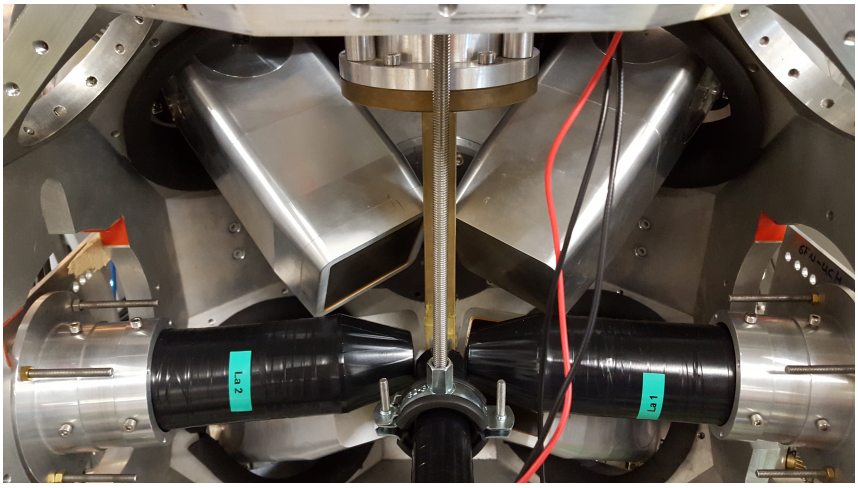

Figure 56: **IDS set up for fast timing measurements.** Close look into the IS610 experimental set up, the $LaBr_3(Ce)$ detectors are tagged as La1 and La2, with the cylindrical β detector facing towards the implantation point

an easier identification of γ-ray transition after the β decay, and on the other hand it can act as a starting time for the $\beta\gamma(t)$ events. For this reason, the choice of a fast β detector is paramount. The β detector employed during this campaign had a cylindrical shape with a thickness of 3mm and a diameter of 25mm, with a reported rise time of 350ps [Tec21]. The β plastic was coupled to to a Hamamatsu H6610 (R5320) PMT, which has a 0.7ns rise approximately [Ham]. This detector is placed in the direction of the beam, just behind the implantation point. The main drawback from it is position is a reduction on β detection efficiency since it's behind two layers of tape. The total β detection efficiency for the campaign is around 22%.

6.3 Electronics

Before arriving into the digital acquisition system, Nutaq , signals from each detector are processed by amplifiers and NIM standard modules. As stated, the electronic paths can be divided into two branches: the energy and the time branch, both displayed in Figure 57.

6.3.1 Energy Branch

On the energy branch, signals are treated separately before arriving into the digital acquisition system (DAQ). The signal treatment is independent and different for each detector on the experimental set-up. Each of the HPGe-clover detector signals are adjusted in a linear amplifier named GoBox before being fed to the Nutaq.

$LaBr_3(Ce)$ detectors give two output signals; a positive signal from the dynode (DY) and a negative signal from the anode (SIG). The first one is used to retrieve the

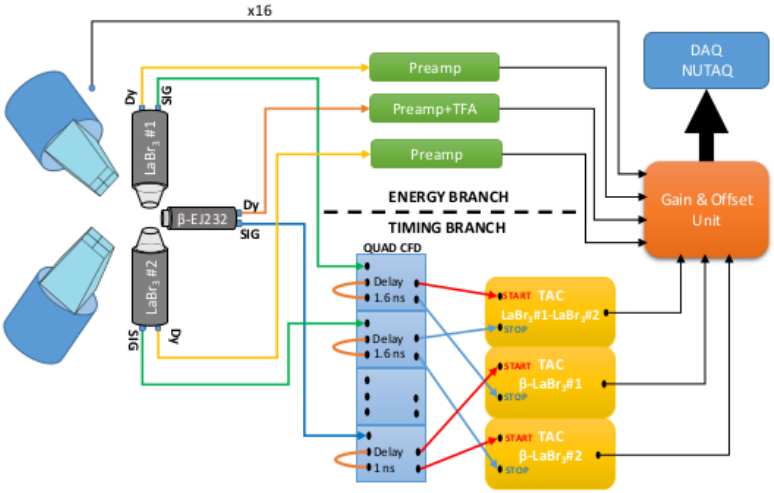

Figure 57: **IDS electronic set up scheme from IS610 campaign.** Image taken from [Ben].

energy information while the one from the anode is used for timing measurements. An ORTEC 113 Preamplifier with a 500 pF input capacity preprocesses the energy response. The signals are then sent to the GoBOX to have their gain adjusted before being entered into Nutaq.

Similarly to the $LaBr_3$(Ce)detectors, the energy signal for the EJ232 plastic is derived from the positive PMT dynode output. Before being sent to an ORTEC 474 Timing Filter Amplifier (TFA) in 2016, the signal was first passed through an RC integrator (that acts as a low pass filter). The ORTEC 474 TFA was set up with a coarse gain of 10, fine gain of 7.25, and integration duration of 200 ns. The GoBOX received the signal after the TFA, before arriving into Nutaq

6.3.2 Time Branch

Electronic fast-timing measurements are performed by analog electronics before being fed into the DAQ. Therefore, the goal of the timing branch is to obtain the time difference between each combination of scintillator detectors. For this experiment, a classic fast-timing set up was employed. Each of the signals coming out of the anode of each detector is fed into an ORTEC 935 Quadruple CFD. Each of the signals are treated on the same CFD module, using 1.6 ns delay for the $LaBr_3$(Ce) detectors, and 1 ns for the β detector. CFD parameters have been optimized for the threshold (T) and the zero crossing value (Z) setting them at -507 mV and +2.0 mV values respectively in order to have an optimal time response at the expense of a long time walk.

Two signals are taken from each detector from the CFD module. The time difference between the arrival of two signals is converted into an output signal with an amplitude proportional to their time difference by three ORTEC 567 Time to

Amplitude Converter (TAC) 200 MHz modules. When the two signals are sent to the TAC within the chosen time range, an output signal is produced whose height is proportional to the time difference between the signals. This output signal is generated after the arrival of the signal that is used as START, the TAC beginning to rise the voltage until the stop signal is received. Three TAC modules were employed in the IS610 experiment, two dedicated to measure time differences between the β detector with each of the $LaBr_3$(Ce) detectors, while the last TAC is used for coincidences between the lanthanum detectors. The outputs of each TAC are fed into the GoBOX before arriving into the Nutaq.

6.4 Digital acquisition system

Information from each detector, TACs and some extra logic inputs (such as the time of arrival of the proton on the target) are fed into the digital data acquisition system NUtaq [Nut]. This data acquisition system consists of three 14 bit digitizer cards with 16 channels each with a sampling rate of 100MS/s. Digitized data is processed by a trapezoidal filter, whose parameters are independently adjusted for every signal. Finally, information relevant to the pulse's amplitude, timestamp, and channel are transmitted to a computer and stored in list-mode files with a 2 GB maximum size.

The energy branch for the HPGe-clover type detectors is stored in the first 8 channels of the first 2 digitizer cards, while the energy branch of the $LaBr_3$(Ce) and the β detector is allocated on the third digitizer card. The time branch is allocated in the third card together with extra logic inputs such as the time of the arrival of the proton which is given by the T1 signal coming from the PSB, the signals of the TACs between the β and the scintillator detectors and the time when the tape starts moving and stops. The distribution of each signal is displayed in table 16.

Channel	Card 1	Card 2	Card 3
0	HPGe 1-1	HPGe 3-1	T1 Proton signal
1	HPGe 1-2	HPGe 3-2	TAC γ1-γ2
2	HPGe 1-3	HPGe 3-3	TAC β-γ1
3	HPGe 1-4	HPGe 3-4	TAC β-γ2
4	HPGe 2-1	HPGe 4-1	Beamgate closed
5	HPGe 2-2	HPGe 4-2	Tape start
6	HPGe 2-3	HPGe 4-3	Tape stop
7	HPGe 2-4	HPGe 4-4	-
8	-	-	-
9	-	-	-
10	-	-	β Energy
11	-	-	γ1 Energy
12	-	-	γ2 Energy
13	-	-	-
14	-	-	-
15	-	-	-

Table 16: **Signal distribution in the Nutaq digitizer cards**. γ1 and γ2 refer to $LaBr_3$ detectors 1 and 2 respectively

7 Nuclear structure of the even-even ^{130}Sn nucleus

The understanding of the evolution of shell structure far from the β-stability line is one of the top challenges in modern nuclear structure. Neutron-rich nuclei with a number of protons and neutrons close to magic numbers are an ideal testing ground for shell-model calculations. The structure of the even-even nucleus ^{130}Sn (Z=50, N=80), in the vicinity of ^{132}Sn (N=82) shell closure [Ben+20], is interesting from this point of view. The expected neutron-neutron couplings in ^{130}Sn arise from the shell-model configurations, with two neutrons holes below the N=82 gap.

In this chapter we report on the IS610 experiment carried out at the ISOLDE Decay Station (IDS) located at the ISOLDE facility at CERN, described in the previous chapter. The experiment was aimed at completing the known level scheme as well as measuring excited level lifetimes. The ^{130}Sn structure was populated in the β decay of ^{130}In, produced as a fission product of a UC_x target. We took advantage of the isomeric selection capability of the Resonance Ionization Laser Ion Source (RILIS) to enhance the ionization of the three known ^{130}In β decaying isomers to individually study their decay. The three ^{130}In isomers under study have (1^-), (10^-) and (5^+) spin and parity assigned to them, being (1^-) the ground state with a 0.29(2)s lifetime, the first long-lived isomer being the (10^-) located at 58.6keV from the ground state with a lifetime of 0.54(1)s and the (5^+) is second long-lived isomer placed 385.5keV above the ground state with a lifetime of 0.54(1)s. Gamma spectroscopy using high-resolution HPGe detectors was employed to construct the level scheme. For the measurement of level lifetimes the Advanced Time-Delayed $\beta\gamma\gamma$(t) method [MGM89] described in Chapter 4 was used. The knowledge of the level scheme and the half-lives allows us to extract transition probabilities that make it possible to compare with theoretical calculations.

The data analysis can be divided into two main branches: γ spectroscopy and lifetime measurements. The first one consists of the identification of the γ rays belonging to the desired nuclei and the construction of the level scheme. The second part of the study deals with lifetime measurements of excited levels of the desired nuclei. An extended level scheme of ^{130}Sn compared to the previous work [FHS81] has been obtained. Level lifetimes for some of the low-lying states have also been measured.

7.1 Previous work

The nuclei on the vicinity of the ^{132}Sn double shell closure have been of interest for the investigation of the evolution of shell structure and the development of collectivity in this exotic region of the table of nuclides. The decay of indium isotopes provides key information via the β decay into *magic* tin isotopes, with $Z = 50$. Among the nuclei close to ^{132}Sn, ^{130}Sn is interesting as an even-even nucleus where only two neutrons are removed from the full neutron shell, and should be sensitive to pairing effects. Expected neutron-neutron couplings in ^{130}Sn arise from the shell-model configurations in the region.

The ^{130}Sn isotope has been previously investigated in the β decay of ^{130}In. Early data from this decay dates back to 1980, when Birger Fogelberg *et al.* [FHS81] performed a complete study. The experiment took place in the OSIRIS isotope separator facility where indium isotopes were produced in the fission of a ^{235}U target. In the experiment the three isomeric states of ^{130}In were populated, and a β-decay study was performed to understand the ^{130}Sn nuclear structure.

The β-decay half lives of ^{130}In were measured in the experiment cited above [FHS81], yielding results 0.330(3) s for the ^{130g}In and a combined value of 0.530(3) s for both isomeric states, since they could not be separated. Lifetime measurements of excited states were also performed by electronic coincidences between a plastic scintillator and a small NaI detector using $\beta\gamma$ coincidences. The results from timing measurements are displayed in Table 17, and have not being reviewed until the present work, where we expect that the previous results could be verified and expanded.

J^{Pi}	Level (keV)	$T_{1/2}$	Transitions			Transition Rate
			Energy (keV)		$T_{1/2\gamma}$	B(Xλ)
(5^-)	2084.84	52 ± 3 ns	E1	89.23	83 ns	$(7.4\pm0.4)\times10^{-6}$ e^2·fm^2
			E2	137.96	139 ns	(81 ± 5) e^2·fm^4
			E3	863.60	<5.6 μs	$<6.1\times10^2$ e^2·fm^6
$(4^-,5^-)$	2214.67	<0.5 ns	M1	129.80	0.5 ns	3.6x10^{-2} μ_N^2
			E1	219.08	<18 ns	2.3×10^{-6} e^2·fm^2
(10^+)	2434.81	1.61±0.15 μs	E2	96.54	4.6 μs	(14.5 ± 1.4) e^2·fm^4
			E3	487.93	>47 μs	$>3.9\times10^3$ e^2·fm^6

Table 17: **Summary of ^{130}In half-life measurements performed in [FHS81].** Data taken from the source, [FHS81], which includes the calculated transition probabilities. $T_{1/2\gamma}$ refers to the partial half life.

Apart from the β-decay studies reported in [FHS81] and [Fog+85] there is not much information about the structure of ^{130}Sn. A microsecond isomer was identified, and later confirmed in the fission of ^{239}Pu and ^{241}Pu, with 1.6(1) μs half-life. In spite of being a very well produced fission product in the thermal neutron-induced fission of ^{232}Th, ^{235}U, $^{240}240$, ^{244}Cm and ^{245}Cm, and also in fast-neutron and particle-induced fission of actinide targets, ^{130}Sn has not been thoroughly studied in fission

until recently in the EXILL campaign at ILL (see brief description in Chapter 4).

The population of excited states in ^{130}Sn has also been reported from the β-n decay of ^{131}In [Dun+19; Ben22]. Other works concentrate on the high-energy dipole strength distribution above the one-neutron separation energy using Coulomb dissociation [Adr+05]. It is worth mentioning that a B(E2) of 1.2(3) W.u. is reported in [Rad+05] for the $0^+ \rightarrow 2^+$ transition from Coulomb excitation, which yields a 6.5(15)ps half-life for the 2^+ state in ^{130}Sn at 1221.3 keV.

7.2 Theoretical models currently employed in the 132Sn region

The nuclear shell model (SM) remains as one of the most fundamental approaches for a microscopic description of nuclear structure. This model successfully predicts experimental information obtained near closed-shell nuclei, such as the doubly-magic ^{132}Sn. The ^{130}Sn nucleus under study in this thesis is a singly closed nuclei, having Z=50 protons and N=80 neutrons. This *magic* nucleus, with two valence neutron holes, becomes a benchmark to study the nuclear structure below ^{132}Sn. In the case of this region in the vicinity of A=130, most of the available SM calculations [SW22; Dut+22] are performed using a single particle model space consisting of neutrons occupying $0g_{7/2}$, $1d_{5/2}$, $2s_{1/2}$, $0h_{11/2}$ and $1d_{3/2}$ orbitals. Owing to the pair of neutron holes in ^{130}Sn, the two-body interaction is expected to play an important in this case, which in principle makes it possible to study its dependence with the filling of neutron orbitals in the even-even Sn isotopic chain. Various model alternatives exist. One of them, described in detail in [Ter+15], employs a truncation method which comes as a solution to handle the huge dimension of the SM space in heavy nuclei with mass is above 100. The effective interaction employed in this particular method, coined pair-truncated shell model (PTSM), consist of single-particle energies and phenomenological two-body interactions (mainly monopole and quadrupole) plus a quadrupole-quadrupole interaction(QQ). The model is able to reproduce rather satisfactorily the nuclear structure of ^{130}Sn, as displayed in Figure 58 left, as well as the values for the B(E2) and B(M1) transition rates for Sn isotopes (from previous and this work), [Ter+15].

Another aspect, when studying the A=130 region, is the evolution of seniority levels. This appears in the form of isomeric states, in the ^{130}Sn the existence of the 10^+ state. In case of the even-even Sn isotopes the neutron-neutron part of the SM interaction is derived from the CD-Bonn renormalized G matrix [Bro+05]. Although this model accurately describes the high-parity states and the reduced transition probabilities, displayed in Figure 58, for lighter nuclei the differences between theory and experiment are typically larger than 100 keV [Isk+14].

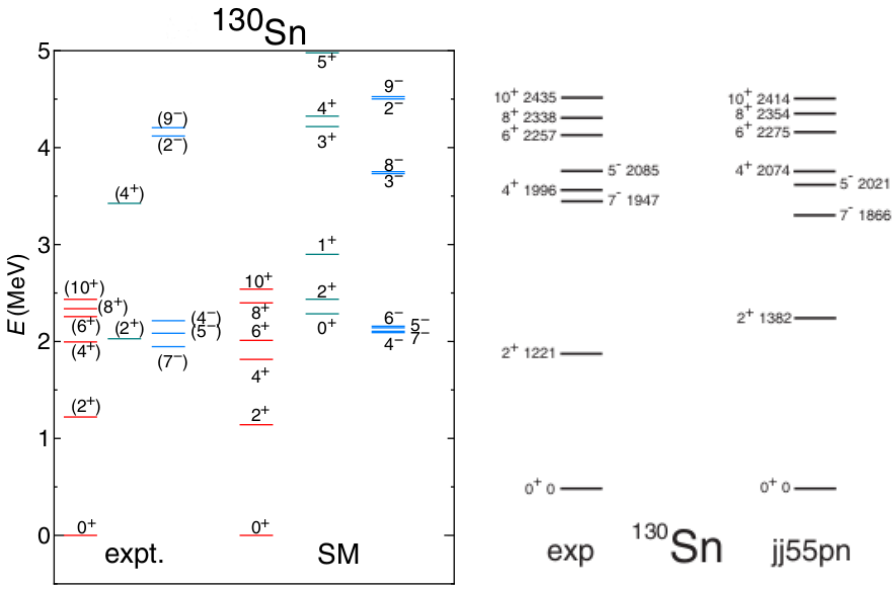

Figure 58: **Comparison between the experimental spectra and the SM results for ^{130}Sn for several SM calculations. Left:** Comparison between the experimental spectra (exp) and the SM results (SM) employing the PTSM, image taken from [Ter+15]. **Right:**Comparison between the experimental spectra (exp) and the SM results (SM) employing the jj55pn calculation, image taken from [Isk+14].

7.3 ^{130}Sn level scheme populated via β decay of ^{130}In

The ^{130}Sn nuclear structure studied in this analysis focuses on the β decay of the three ^{130}In isomeric states.

The total β-decay energies of the three isomers in ^{130}In were already discussed in [Fog+85] and are not discussed in this research. The masses of both ^{130}In and ^{130}Sn are known from measurements at various facilities, including ISOLTRAP [Sik+05], the Canadian Penning Trap mass spectrometer [Van+13] and JYFLTRAP [Kan+13], which give a Q_β value of 10225.7(2.6) keV. The neutron separation in ^{130}Sn is 7613(5) keV [Wan+21] and thus feeding of excited states up to this energy and above the S_n can be expected in this decay.

The β decay from ^{130g}In to ^{130g}Sn is rather complex due to the existence of isomeric states in both of the nuclei. There are three different isomeric states in ^{130}In, with spins and parity assigned by 1^-, 10^- and 5^+ for the ground and the two long-lived isomeric states, respectively [FHS81]. The 1^- and 10^- isomers are interpreted as the lowest members of the $\pi g_{9/2}^{-1/2} \nu h_{11/2}^{-1/2}$ multiplet [KCB74; FHS81; Fog+85], while the 5^+ state is attributed to the $\pi g_{9/2}^{-1/2} \nu d_{3/2}^{-1/2}$ configuration [Fog+85]. The masses of the three beta-decaying states were recently resolved in mass measurements [Nes+20] giving 58.6(82) keV and 385.5(50) keV for the excitation energies of the ^{130m1}In and ^{130m2}In states, respectively.

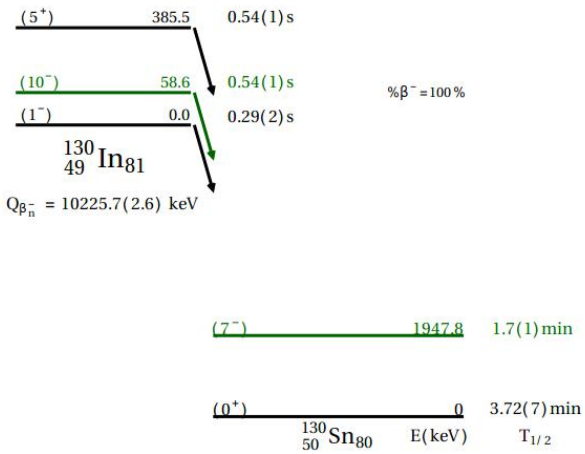

Figure 59: β **decay scheme of** ^{130}**In** β **decay populating** ^{130g}**Sn.** The ^{130}In ground state and second long-lived isomer populate the ground state of ^{130}Sn. In green, the (10^-) long-lived isomer of ^{130}In mainly populates the long lived (7^-) isomer in ^{130}Sn

The β decay of ^{130}In is displayed in Figure 59 where the ^{130g}In (1^-) and ^{130m2}In (5^+) β decay populate the ^{130g}Sn (0^+) ground state with some common γ rays, and specifically the one that goes from the (6^+) state at 2216 keV down to the ground state. In turn, the beta ^{130m1}In (10^-) decay populates the ^{130m1}Sn (7^-) long-lived isomeric state at 1947.8 keV.

7.3.1 Analysis methodology: construction of the level scheme

For this part of the analysis, the HPGe detectors play a crucial role in studying the γ decay spectra under study. Three different sorts of information can be employed in our experiment to identify the γ rays in the spectra. The half-life of the isotope decay in which they are emitted is significantly connected with their time distribution with respect to the proton pulse arrival time. Additionally, requiring a second coincidence with the β-detector assures that the γ rays were emitted after a β-decay, minimizing the impact of other types of contaminants. Thirdly, the construction of the level scheme via $\gamma\gamma$ coincidences using previously known transitions in order to allocate the new γ rays found during the analysis.

In order to analyse this data, the *xtrackn* tool from the GASPware data analysis package for nuclear spectroscopy [Mar+17] was employed to analyse the 2D matrices in GASP format. The GASP format is useful to generate the 2D and 3D matrices needed for the analysis. For the construction of the level scheme, beta gated matrices as well as a γ-γ were used to identify unknown peaks and do a coincident study, both can be seen in Figure 60.

In this analysis we will try to profit from the isomer separation in order to obtain

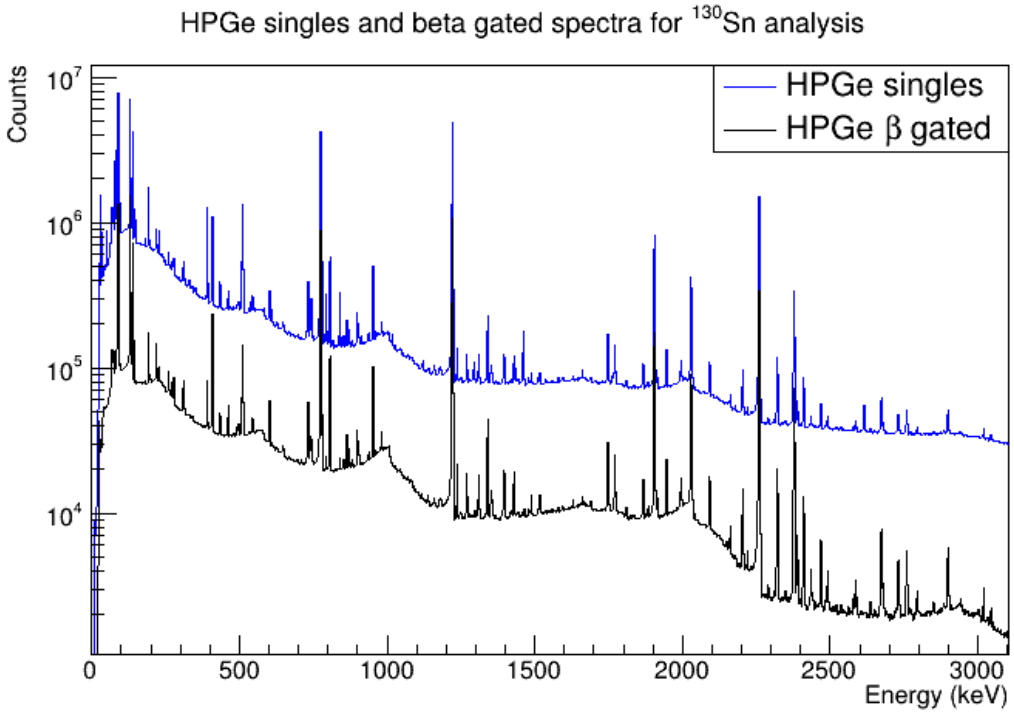

Figure 60: **HPGe spectra from the IS610 corresponding to the ^{130}Sn nuclei.** In order to study the level scheme of the desired nucleus, singles HPGe spectra and β gated spectra help to determine which γ rays come from the nucleus under study

β-feeding intensities for each individual isomer. Each one needs to be separated from the rest as much as possible. The performance of the RILIS for isomeric separation in narrow-band mode is illustrated in figure 61, where the decay of selected γ rays that are only populated in a given β decay due to the de-excitation of a particular level are chosen. These are the one at 2337 keV for the ^{130m2}In (5^+), the 2258-keV γ-ray for the ^{130m1}In (10^-) and the 1908-keV γ-ray for the (1^-) ground state decay. As illustrated, it is possible to enhance all the three isomers by selecting a particular wavelength. This works particularly well for the 10^+ and the 5^+ isomers, while the ^{130g}In (1^-) decay cannot be totally separated from the ^{130m2}In (5^+) excited state decay.

The data were taken in three sets during the experiments, each one with the enhancement of the ^{130g}In (1^-) decay, ^{130m1}In (10^-) decay and ^{130m2}In (5^+) decay, respectively. A fourth data set acquired in broad-band RILIS mode is also available. A full set with the total statistics has been constructed and it is used for the construction of the level scheme via $\gamma\gamma$ coincidences and for lifetime studies. The three narrow-band data sets are used to obtain the intensities and to determine the allocation of γ-ray to a particular decay. Although the isomer selection is not pure, in the following we identify the enhanced isomeric decays, for instance runs where the ^{130g}In decay is favoured has been labelled ^{130g}In decay run.

Since each data set still contains admixture of the three decays from the ^{130}In

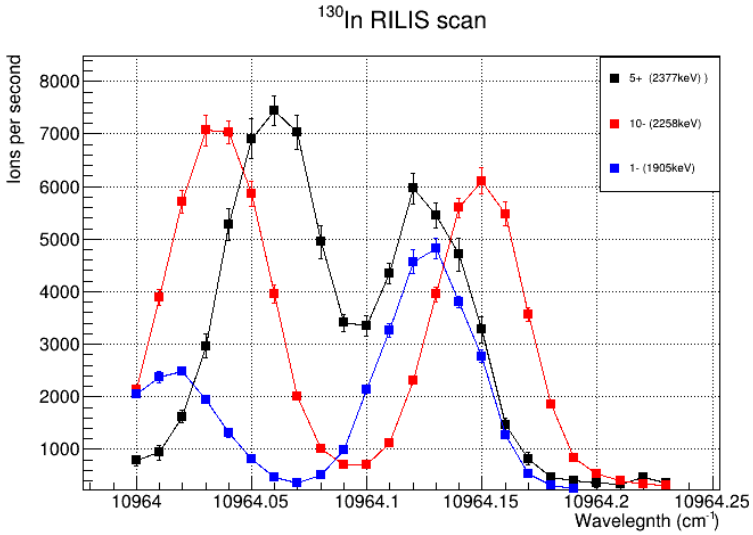

Figure 61: **Laser scan for the production of ^{130}Sn.** Each value has been obtained studying the characteristic γ rays from each isomer

isomeric states, the *contamination* factor of each of the isomers must be found. We can define this factor, or percentage, as the amount of isomer decays that do not correspond to the decay under study. This, can be done by studying the area of the exclusive γ-rays that come from each decay. The γ-rays employed are the one at 2337- and 3184-keV for the ^{130m2}In (5^+), the 391- and 2258-keV γ-rays for the ^{130m1}In (10^-) and the 952- and 1905-keV γ-ray for the (1^-) ground state decays. The obtained values for the area for each of the peaks on each of the data sets is displayed in Table 18. With this information, one can optimize the 3 equation system in order to obtain the factor of each of the *isomeric contamination* on the desired decay.

	Area of ^{130g}In decay γ rays (Counts)		**^{130m2}In decay γ rays (Counts)**		**^{130m1}In decay γ rays (Counts)**	
	1905 keV	**953 keV**	**2377 keV**	**3184 keV**	**2258 keV**	**391 keV**
^{130g}In (1^-) decay	*348336*	*125503*	191873	103125	223036	107827
^{130m2}In (5^+) decay	163261	59597	*269017*	*145206*	799193	363823
^{130m1}In (10^-) decay	192207	66906	44763	23301	*1156368*	*531965*

Table 18: **Areas of each of the exclusive γ rays on each of the β decays of ^{130}In ground and isomeric states**

Once the *contamination factors* have been obtained, they must be implemented. For this step, the time of arrival of a proton on target has been employed. By placing a time window on the time of arrival, we have the ability to control the amount of the desired isomer without the need of manipulating the data. By tuning the gate on the proton time of arrival, each of the percentages can be applied into the data sets in order to obtain the peak areas to clean the desired isomeric decay. Theses peak areas come from multiplying the *contamination factor* with the area on the

enhanced data set from the *isomer contaminant*.The spectra selected by a certain time since the proton arrival grants information about the nuclei production and its decay, as defined by the release time from the target and the decay lifetime. The procedure is not exact due to the statistical fluctuations and difficulties of defining the peak areas due to the different contributions of Compton events under the peak, but should provide a purified decay spectrum for each of the isotopes. Some over subtractions may arise due to the uneven contributions of the β decay of the ^{130}Sn states to ^{130}Sb. The final results of this procedure are displayed in Table 19.

	Area of ^{130g}In decay γ rays (Counts)		**^{130m2}In decay γ rays (Counts)**		**^{130m1}In decay γ rays (Counts)**	
	1905 keV	**953 keV**	**2377 keV**	**3184 keV**	**2258 keV**	**391 keV**
^{130g}In (1^-) decay	*288022*	*102394*	1352	0	0	8150
^{130m2}In (5^+) decay	0	2330	*219609*	*119153*	9494	0
^{130m1}In (10^-) decay	5800	0	1031	0	*1265655*	*577379*

Table 19: **Areas of each of the exclusive γ rays for each of teh β-decays after the cleaning procedure.**

An example of the results from this procedure is displayed in Figure 62. This image shows each of the spectra already cleaned in the region close to the most intense peak of the ^{130m1}Sn β decay (2258 keV γ-ray). As can be seen, some γ rays may display a subtraction either on the left or in the middle of the peaks. In case of the left side subtraction, the area from the subtraction has to be taken into account when obtaining the intensities of the γ ray under study. On the other hand, the ones that have a centred subtraction have been proven to approximately have zero net area of the order of the level of background.

7.3.2 Analysis methodology: β-delayed neutron emission and ground state feeding

In the A=130 experiment investigated in this PhD thesis there is no suitable data set that could be analysed to provide reliable P_n nor direct ground-state β feeding values. The reason is that data were collected on an aluminized tape that was moved periodically to removed long-lived activities, mainly coming from the β decay of ^{130}Sn but also from the β decay of ^{129}Sn, expected from β-delayed neutron emission branch. In any case, we have investigated the direct ground-state feeding and the β-delayed neutron emission probabilities from the observation of γ rays in ^{129}Sb and ^{130}Sb and correcting by the implantation pattern and the removal of activity using the Bateman equations.

Concerning the β-delayed one neutron emission probability, P_1n, several literature values exist from direct neutron detection. The evaluated values from [SIN01] give P_1n=1.20(29)% for the ^{130g}In, and P_1n=1.95(15)% for the combination of ^{130m1}In and ^{130m2}In. Admixtures of several β-decaying states cannot be excluded in the reported data.

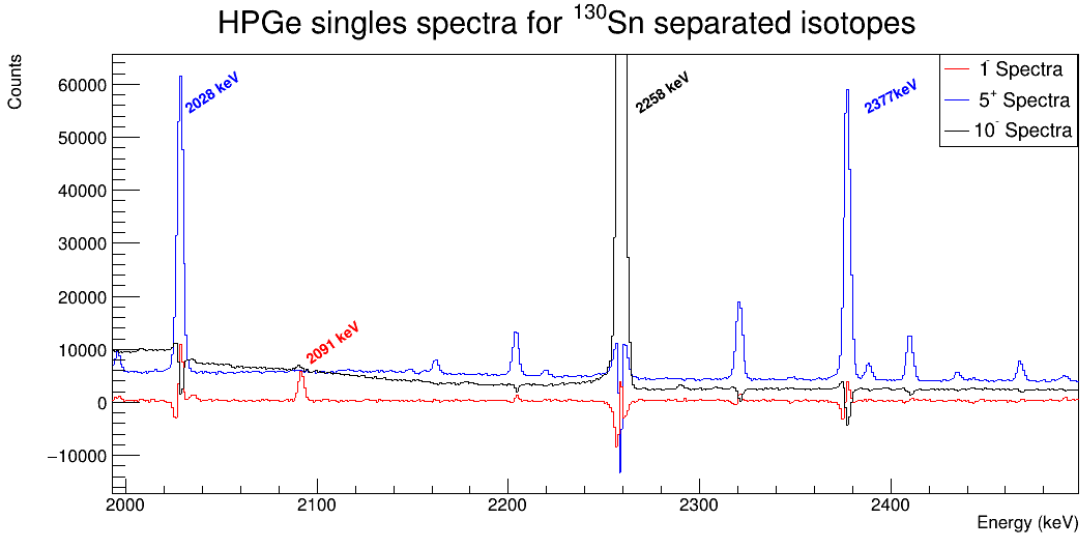

Figure 62: **HPGe clean spectra for each ^{130}Sn isomer.** Zoom has been made into the 2258 keV γ-ray region, where some of the most characteristic γ rays from each isomer appear. As can be seen, subtraction peaks can be seen in all the spectra, this is due to not appearing on the populating level scheme or low intensity.

From the observation of the γ-rays of 315 and 2118 keV a weak population of excited states in $129Sn$ cannot be totally excluded, which will entail the direct β-n decay branch to excited states. The weak intensity of these γ-rays and the proximity of strong peaks does not make it possible to quantify the intensity of the observed γ-rays. From the daughter activity the β-n branch can be studied. The 645 keV gamma in ^{129}Sb once corrected for the implantation sequence and the decay before the removal of activity, yields values compatible with literature but with very large uncertainty arising from the different correction factor. Thus, we adopt the literature values to correct the β-feeding.

For the analysis of the ground state β feeding a similar procedure is followed, but in this case employing the most intense γ-rays in ^{130}Sb from the decay of ^{130}Sn, with energies of 70 keV populating the ^{130m1}Sn and 733 keV populating the ^{130g}Sn are observed. It is again very difficult to measure precise values for the ground state feeding owing to the strong corrections that need to be applied, but it estimated that both the ground-state feeding from ^{130g}In to ^{130g}Sn and the ^{130m1}Sn to the β-decaying (7^-) state in ^{130}Sn are positive and compatible with $\approx$10%.

7.3.3 Level Scheme populated in ^{130g}In (1^-) β decay

The first analysed β decay comes from the ^{130}In ground state, ^{130g}In and populates the excited ^{130}Sn structure built on the ground state. This decay has been studied in depth by [FHS81] and displayed 8 levels in a range of energy from 0 up to 4119 keV. Our new level scheme covers all the previously known γ rays with the addition

of 4 new levels and 8 new γ transitions. Out of the five new levels one has been observed in the ^{130m2}In decay as well, but populated by different transitions. The spin and parity assigned to those levels is (4^-) and (6^+), which is not possible to populate by β feeding from the 1^- in the decay of ^{130g}In. These two levels have been added to the level scheme since the gammas populating them (γ transitions with energies $\approx$ 2.7 and 3.3 MeV) have been only observed in the clean spectra for ^{130g}In. The new level scheme is shown in Figure 66 and a table regarding the β feeding and logft is displayed as Table 20. The β feeding to ^{130gn}Sn has been determined from the balance between feeding and de-exciting γ rays from each level.

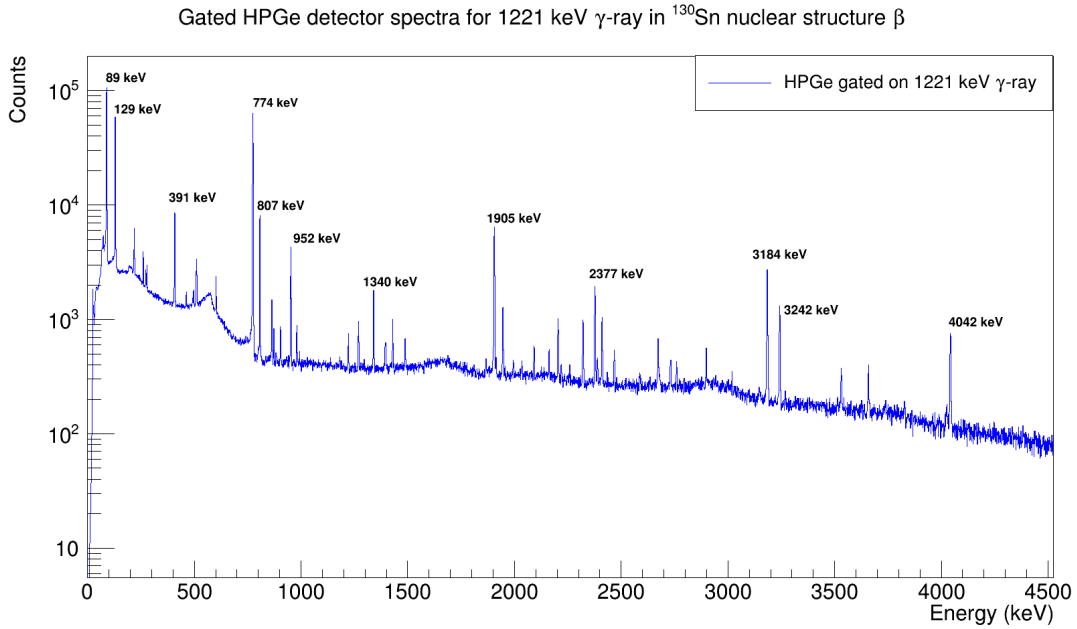

Figure 63: **HPGe detector coincident spectra with the 1221 keV γ ray** The spectrum comes from all the statistics, the recognized peaks are the common γ rays from most of the ^{130}In beta decays and some of the exclusive for each decay.

The common 2^+ state in all even-even nuclei is displayed as the first excited state at 1221 keV from the ground state, followed by the long-lived isomeric 7^- that is populated with a 137.8 keV γ ray on this decay (this level is heavily populated via ^{130m1}In beta decay). In order to build the level scheme the 1221-keV γ ray plays an important role since there are not many γ rays that feed the 0^+ directly, so most of the decays will end up in the first excited state. Figure 63 displays the $\gamma\gamma$ coincident spectrum between HPGe detectors which provides important information to build the level scheme, the γ rays identified on the figure are from both ^{130g}In and ^{130m2}In beta decays where 952- and 1905-keV γ rays come from ^{130g}In β decay and 2377-, 3184- and 4042-keV γ rays belong to ^{130m2}In β decay. In order to know which γ belongs to which decay the clean singles spectra have been used.

In the ^{130g}Sn levels scheme populated via ^{130g}In two γ rays are intense and

particular on the decay: the 1905 keV and the doublet at 952 keV. These transitions come from high energy excited states, which helps to configure the level scheme under 2216 keV for this decay. Figure 64 displays both of the coincident spectra when gated on both energies. As can be seen, the 952-keV γ is in coincidence with itself, denoting a doublet that populates and de-excites the $(2^-,3^+)$ level at 3168 keV. The intensity for each of the γ rays in the doublet has been obtained via coincidence measurements.

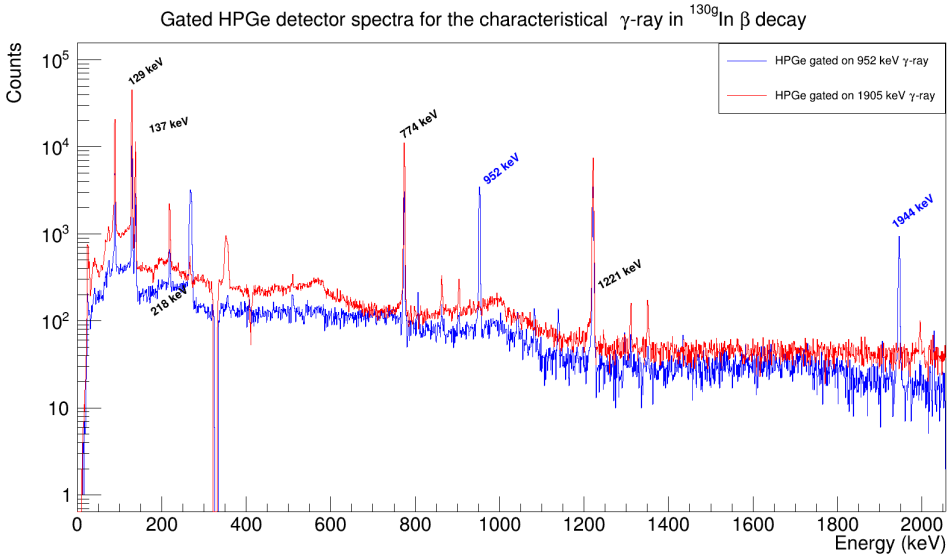

Figure 64: **HPGe detector coincident spectra with the 952 keV γ ray doublet (blue) and the 1905 keV (red) γ-ray.** Both γ rays are exclusive to the ^{130g}In β decay to the ^{130g}Sn and helps to study the low energy regions for this decay .

A new level has been added above 5.8 MeV with two de-exciting γ transitions. The level is located at 5840 keV and de-excites via 3626- and 3349-keV γ rays populating the 2216- and 2490-keV states, respectively. Both of the coincident spectra are displayed in Figure 65. Looking into the coincidence of the 3626-keV γ ray, a clear coincidence with 89-, 129-, 774- and 1220-keV γ rays is displayed, pointing to the direct feeding of the 2216-keV 4^- level. The reciprocal gates have been applied, and each of the γ transitions mentioned above show a coincidence with the 3626-keV γ ray.

On the other hand, the 3349-keV coincidence spectrum displays an interesting pattern. Prior to this analysis the 2490-keV state in ^{130g}Sn had feeding assigned only from the ^{130m2}In isomer β decay. In our analysis, the 1269-keV γ ray has been found on the cleaned singles spectrum for the ^{130g}In β decay, and two more γ rays have been added to the de-population of this level. The three γ rays that depopulate this level are 1269, 462 and 2490 keV, being the last two new additions to the level scheme. The three γ-ray are found in the coincident spectra of the 3349-keV

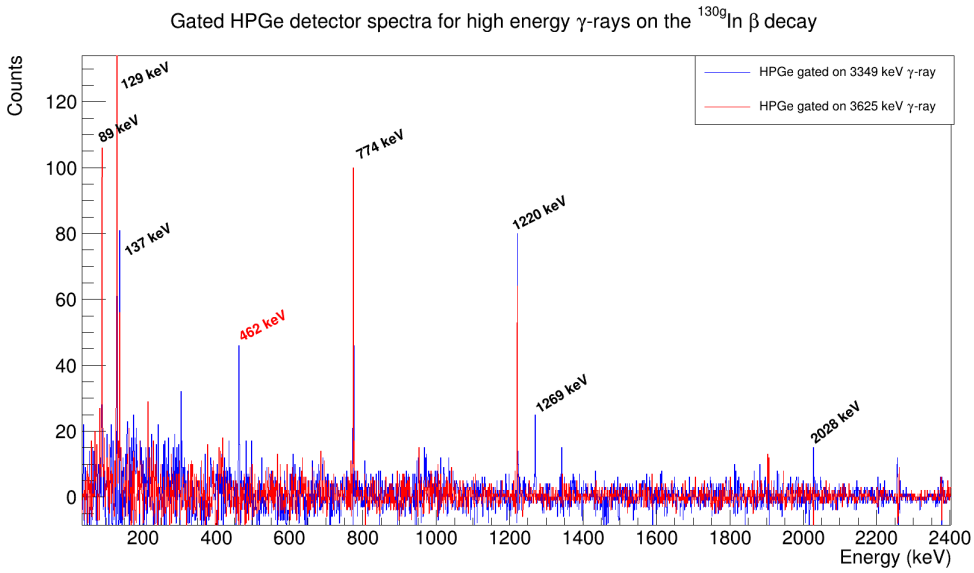

Figure 65: **HPGe detector coincident spectra with the 3349 keV γ ray (blue) and the 3626 keV (red) γ-ray.** New high energy γ rays

transition (2490 is not displayed in Figure 65 due to the energy cut so low energies could be observed), and on the reciprocal gates the 3349-keV line is observed. Due to the existence of these γ rays in singles plus their coincidence spectra with the 3349 keV γ-ray, it has been determined that the 2490 keV excited state is populated in both the ^{130g}In and ^{130m2}In β decays.

$\mathbf{E}_i$(keV)	$\mathbf{J}_i^{\Pi}$ (keV)	$\mathbf{E}_f$(keV)	$\mathbf{J}_f^{\Pi}$ (keV)	$\mathbf{E}_\gamma$(keV)	$\mathbf{I}_\gamma$ (%)	$\mathbf{I}_\beta$(%)	logft
1221.3(4)	2^+	0	0^+	1221.3(3)	100	4.2	6.27(5)
1995.6(5)	4^+	1221.3(4)	2^+	774.3(3)	64.9(7.2)		
2028.3(5))	2^+	1221.3(4)	2^+	807.0(3)	3.45(4)	1	6.75(4)
		0	7^-	2028.4(3)	5.40(5)		
2084.6(6)	5^-	1995.6(5)	4^+	89.0(3)	76.2(8.4)	12.4	5.87(5)
		1946.8(3)	7^-	137.8(3)	28.7(5.1)		
2216.4(6)	4^-	2084.6(6)	5^-	129.6(3)	119(13)		
2490.9(5)	(3-,4+)	2028.3(5)	2^+	462.5(3)	5.7(6)	6.9	5.75(4)
		1221.3(4)	2^+	1269.7(4)	2.1(3)		
		0	0^+	2490.8(3)	3.3(3)		
2709.31(4)	(?)	2028.3(5))	2^+	1488.9(3)	3.6(4)	1.9	6.24
3168.0(5)	(2^- ,3^+)	2216.4(6)	4-	952.7(4)	11.9(2.9)	7.5	5.54
		2028.3(5))	2^+	1138.9(3)	2.9(4)		
		1221.3(4)	2^+	1946.0(6)	10.3(1.3)		
4120.9(5)	2^+	3168.0(5)	(2^- ,3^+)	952.7(4)	14.24(4)	77.4	4.24
		2216.4(6)	4^-	1905.2(6)	83.4(9.3)		
		2084.6(6)	5^-	2035.1(3)	3.0(4)		
		2028.3(5))	2^+	2091.1(4)	6.8(9)		
		1221.3(4)	2^+	2898.8(3)	3.9(5)		
5839.0(5)	(?)	2490.9(5)	(3^- ,4^+)	3349.0(3)	1.23(8)	1	5.56
5840.4(5)	(?)	2216.4(6)	4^-	3625.8(4)	1.72(2)	1.2	5.42

Table 20: **List of γ rays observed in the β decay of ^{130g}In to ^{130g}Sn.** For absolute intensity per 100 decays, multiply by ≈0.79.

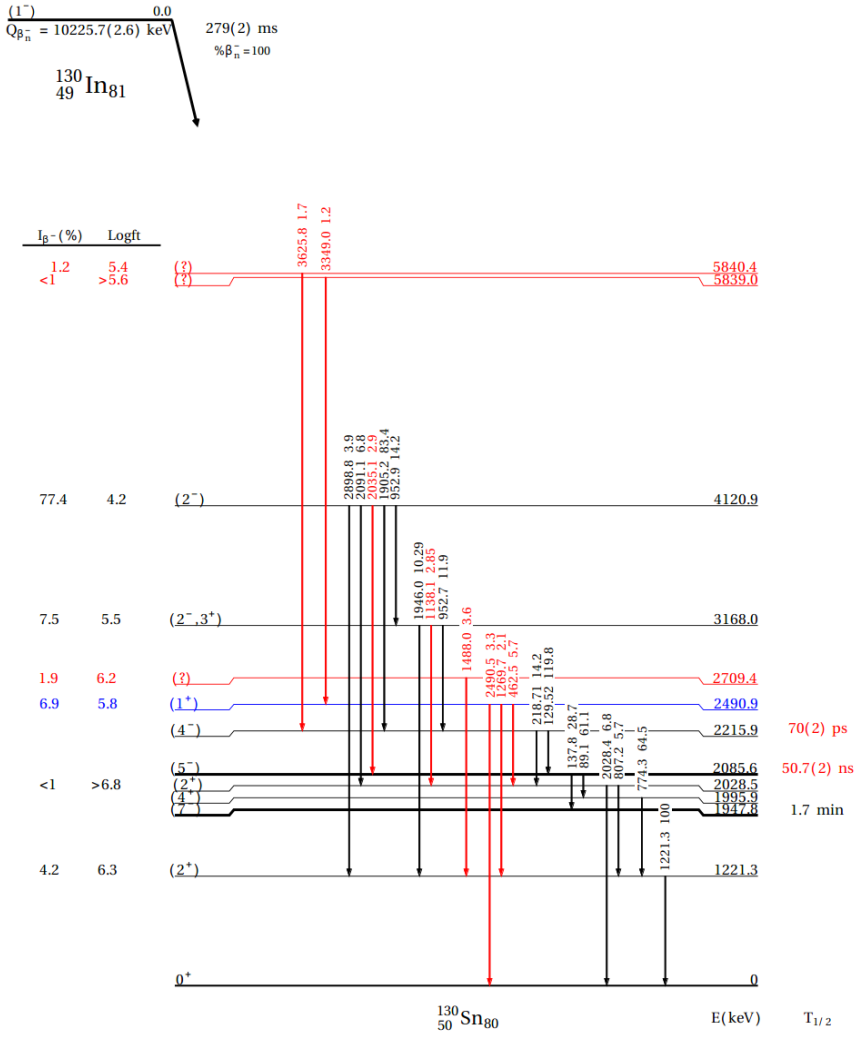

Figure 66: **Proposed Level scheme for ^{130g}Sn following the β-decay of ^{130g}In.** Level scheme was obtained by studying the γ-γ coincidences. The first number on every transition is the energy of the corresponding γ-ray, while the second number is the relative intensity (in %) respect to the 1221-keV transition. For absolute intensity per 100 decays, multiply by ≈0.79 [Cen].

7.3.4 Level Scheme populated in ^{130m1}In (10^-) β decay

The first long-lived isomer in ^{130}In has a proposed spin assignment of 10^- [FHS81]. The level is located ≈ 56 keV above the ^{130g}In state [Nes+20], with values of 58.6(82) and 66.5(99) keV depending on the reference nuclide used in the mass measurements. For our purposes we use a weighted mean value of 62(7) keV. The spin assignment

comes from the presence of strong β transitions populating high-spin levels and from the assumption of the level as one of the lowest members of the $\pi g_{9/2}^{-1/2} \nu h_{11/2}^{-1/2}$ multiplet [KCB74; FHS81; Fog+85]. The subsequent γ rays populate the 10^+ and 7^- levels, located at 2435.7 and 1947.8 keV from the ^{130}Sn ground state.

$\mathbf{E}_i$(keV)	$\mathbf{J}_i^\Pi$ (keV)	$\mathbf{E}_f$(keV)	$\mathbf{J}_f^\Pi$ (keV)	$\mathbf{E}_\gamma$(keV)	$\mathbf{I}_\gamma$ (%)	$\mathbf{I}_\beta$(%)
2339.1(4)	8^+	1947.8(3)	7^-	391.3(3)	19.2(1.2)	≈1
2435.7(5)	10^+	2339.1(4)	8^+	96.6(3)	18(1)	12.3
4206.7(6)	9^-	2435.7(5)	10^+	1771.0(3)	3.4(3)	86.7
		1947.8(3)	7^-	2258.9(4)	100	

Table 21: **List of γ rays observed in the β decay of ^{130m1}In to ^{130m1}Sn.** For absolute intensity per 100 decays, multiply by ≈0.84.

A review of the level scheme proposed in [FHS81] has been done and no new levels have been added to the level scheme, which is displayed in Figure 67 and with more detail in Table 21. For the converted $E2$ 96.2 keV transition the total intensity is provided, employing the theoretical conversion coefficient of $\alpha_T(E2)$=1.312. The level scheme has been built using $\gamma\gamma$ coincidences between HPGe detectors while the intensities have been obtained with the same method as the ^{130g}In β decay to ^{130g}Sn. In order to have a clean ^{130m1}In β decay to study the intensities, the 952 and 3184 keV γ-ray coming from ^{130g}In and ^{130m2}In have been employed. Partial spectra are displayed in Figure 67. We have actively searched for feeding from the (8^+) state to a possible 6^+ state, but no coincidences have been observed.

7.3.5 Level Scheme populated in ^{130m2}In (5^+) β decay

The level scheme of the ^{130m2}In (5^+) β decay to ^{130gn}Sn has been performed via $\gamma\gamma$ coincidences. The results, displayed in Figure 69, cover almost all the previously known γ-ray transitions with the addition of 19 new γ rays plus 5 new excited states. However, the reported γ ray of 3003.6 keV that de-populates the proposed 4224.9-keV level in [FHS81] has not being observed in our work. The β feeding to ^{130gn}Sn has been determined from the balance between feeding and de-exciting γ rays from each level. As for the γ intensities were obtained with the same procedure as for the other two β decays.

The level scheme displays a handful of new excited states above 3425 keV. Most of them decay directly to the (2^+) states at 1220 or 2028 keV excited levels. However, a new level between 3425 and 4405 keV has been found at 3912.3 keV, fed from the previously-known (4^+) 4405.5-keV state via a 493-keV γ ray. The 3912.3-keV level is de-populated via three γ rays of 1421, 1883 and 2691 keV γ-ray transitions. These transitions end up in the (2^+) levels at lower energies. The $\gamma\gamma$ coincidence spectra of the 493-keV γ ray is plotted in Figure 68 painted in blue, while the 1883-keV γ ray coincident spectrum is displayed in red. The spectra show a clear coincidence between two γ rays and the characteristic cascade from the (2^+) at 2028 keV to the

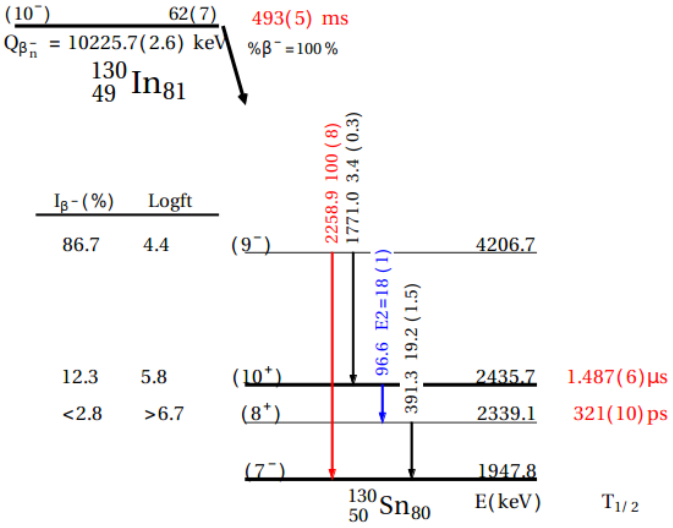

Figure 67: **Proposed Level scheme for ^{130m1}Sn following the β-decay of ^{130m1}In.** The level scheme was obtained by studying the γ-γ coincidences. The quoted β-decay and level half-lives are from this work. The relative intensity (in %) respect to the 2258-keV transition. For absolute intensity per 100 decays, multiply by ≈0.84

(0^+) ground state is shown, via a direct γ-ray of 2028 keV or the 807-1221 keV γ-ray cascade.

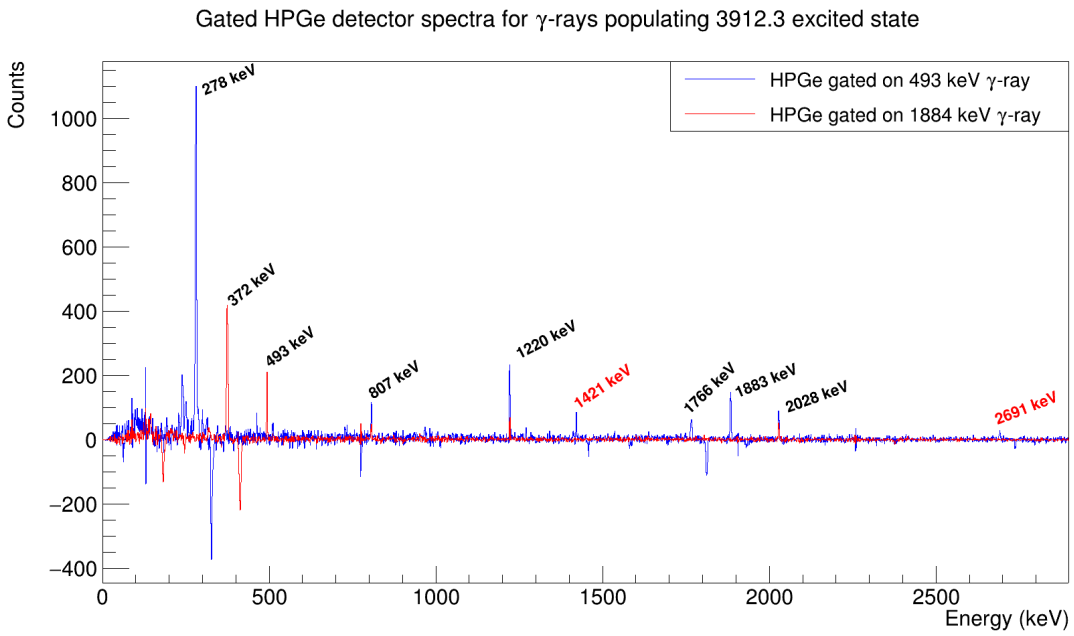

Figure 68: **493 and 1883 γ-ray coincidence spectra. Blue:** Coincidence spectrum gated by the 493-keV γ ray that populates the new 3912.3-keV excited level. **Red:** Coincidence spectrum gated by the 1883-keV γ ray that de-populates the new 3912.3-keV excited level.

7.4 Lifetimes of the β-decaying states in ^{130}In

In this section the β-decay half-lives of the isomeric ^{130}In states are reported. They have been measured from the time difference between the proton impact on target and the HPGe detectors, using the relative time stamps of the signals in the digital data acquisition. The time differences have been processed using a root-based program developed by Jaime Benito.

Since several levels in ^{130}Sn are populated in both the ^{130g}In and ^{130m2}In β decays the previous knowledge of the decay schemes, reported above, is needed. Common γ rays de-exciting levels fed by several isomeric β decays cannot be used to measure lifetimes since the influence from both lifetimes would be observed. For the ^{130g}In (1^-) decay, the 1905- and 953-keV γ rays have been employed. The ^{130m1}In (10^-) isomeric lifetime has been extracted with the 2258-keV γ ray while for the ^{130m2}In (5^+) the 2377- and 3184-keV γ-ray transitions have been used.

7.4.1 ^{130g}In lifetime measurement

Both of the 953- and 1905-keV γ rays used to extract the half-life of the ^{130g}In state are exclusive from the ^{130g}In β decay, de-exciting the 2^- level located 4120 keV, see Figure 66. The time distribution, obtained from the 953-keV γ ray and those of the weaker de-exciting γ rays, is too low in statistics and the time distribution

E_i(keV)	J_i^Π (keV)	E_f(keV)	J_f^Π (keV)	E_γ(keV)	I_γ (%)	I_β(%)	logft
1221.3(4)	2^+	0	0^+	1221.3(3)	100	0.10	8.85(5)
1995.6(5)	4^+	1221.3(4)	2^+	774.3(3)	64.2(7.8)	1.4	6.85(4)
2028.3(59	2^+	1221.3(4)	2^+	807.0(3)	9.0(1.1)	0.7	7.12(5)
		0	7^-	2028.4(3)	14.9(2.2)		
2084.6(6)	5-	1995.6(5)	4^+	89.0(3)	54.1(1.6)	12.4	5.87(5)
		1946.8(3)	7-	137.8(3)	35.2(2.8)		
2216.4(6)	4-	2084.6(6)	5-	129.6(3)	27.2(2.7)	16.4	5.72(5)
		1995.6(5)	4^+	218.7(3)	2.1(2)		
2256.3(6)	6+	1995.6(5)	4^+	260.8(3)	1.6(2)	1.2	6.84(4)
2357.6(7)	(?)	2084.6(6)	5-	273.1(3)	1.1(1)	0.8	6.97(5)
2490.9(5)	(3-,4+)	2028.3(5)	2^+	462.5(3)	1.1(1)	0.6	7.1(3)
		1221.3(4)	2^+	1269.7(4)	1.1(2)		
		0	0^+	2490.8(3)	2.5(4)		
2493.0(7)	(4,5)	2216.4(6)	4-	278.1(4)	1.6(2)	15.0	5.70(5)
		2084.6(6)	5-	408.3(3)	17.3(2.9)		
		1995.6(5)	4^+	497.2(3)	.54(7)		
2597.5(6)	(4,5)	1995.6(5)	4^+	602.0(3)	2.7(1)	2.0	6.54(5)
3425.1(6)	(4+)	2084.6(6)	5-	1340.4(3)	4.8(7)	6.8	5.80(5)
		2028.3(59	2^+	1396.9(3)	1.4(2)		
		1995.6(5)	4^+	1429.6(3)	1.4(2)		
		1221.3(4)	2^+	2204.0(5)	2.3(3)		
3912.3(6)	(?)	2490.9(3)	(3-,4+)	1421.7(3)	0.10(1)	0.2	7.31(5)
		2028.3(5)	2^+	1884.0(4)	0.40(6)		
		1221.3	2^+	2691.5(5)	0.1		
4405.5	(4+)	3912.3(6)	(?)	493.3(4)	0.4(1)	30.0	4.87(5)
		3425.1(6)	(4+)	980.4(3)	1.0(2)		
		2490.9(5)	(3-,4+)	1914.1(3)	0.7(1)		
		2084.6(6)	5-	2320.8(4)	4.6(6)		
		2028.3(59	2^+	2377.2(3)	17.6(2.5)		
		1995.6(5)	4^+	2410.0(3)	2.5(4)		
		1221.3(4)	2^+	3184.3(3)	12.2(1.7)		
4463.3(5)	(4+)	2028.3(59	2^+	2435.0(4)	0.4(1)	5.6	5.58(5)
		1995.6(5)	4^+	2467.8(5)	1.1(2)		
		1221.3(4)	2^+	3242.0(3)	5.8(8)		
4843.3(7)	(?)	2084.6(6)	5-	2758.7(4)	0.9(1)	0.7	6.35(4)
4879.4(5)	(?)	2490.9(5)	(3-,4+)	2388..5(3)	1.0(1)	1.9	5.91(3)
		2084.6(6)	5-	2794.5(4)	0.20(4)		
		1221.3(4)	2^+	3658.2(3)	1.3(2)		
4884.4(7)	(?)	2256.3(6)	6+	2587.4(4)	0.34(6)	0.3	6.78(5)
5263.3(5)	(4+)	1995.6(5)	4^+	3268.1(4)	0.15(2)	3.6	5.51(5)
		1221.3(4)	2^+	4042.1(3)	4.5(6)		
5823.3(7)	(?)	1995.6(5)	4^+	3794.9(5)	0.23(4)	0.3	6.33(5)
		2028.3(59	2^+	3827.8(4)	0.23(4)		

Table 22: **List of γ rays observed in the β decay of ^{130m2}In to ^{130g}Sn.** For absolute intensity per 100 decays, multiply by ≈0.86.

impracticable for the lifetime measurement. The time distribution used is the one of the 1905-keV γ ray, displayed in Figure 70. The value extracted by an exponential fit to the slope, $T_{1/2}$=285(6) ms, is in perfect agreement with the one of 0.29(2) s

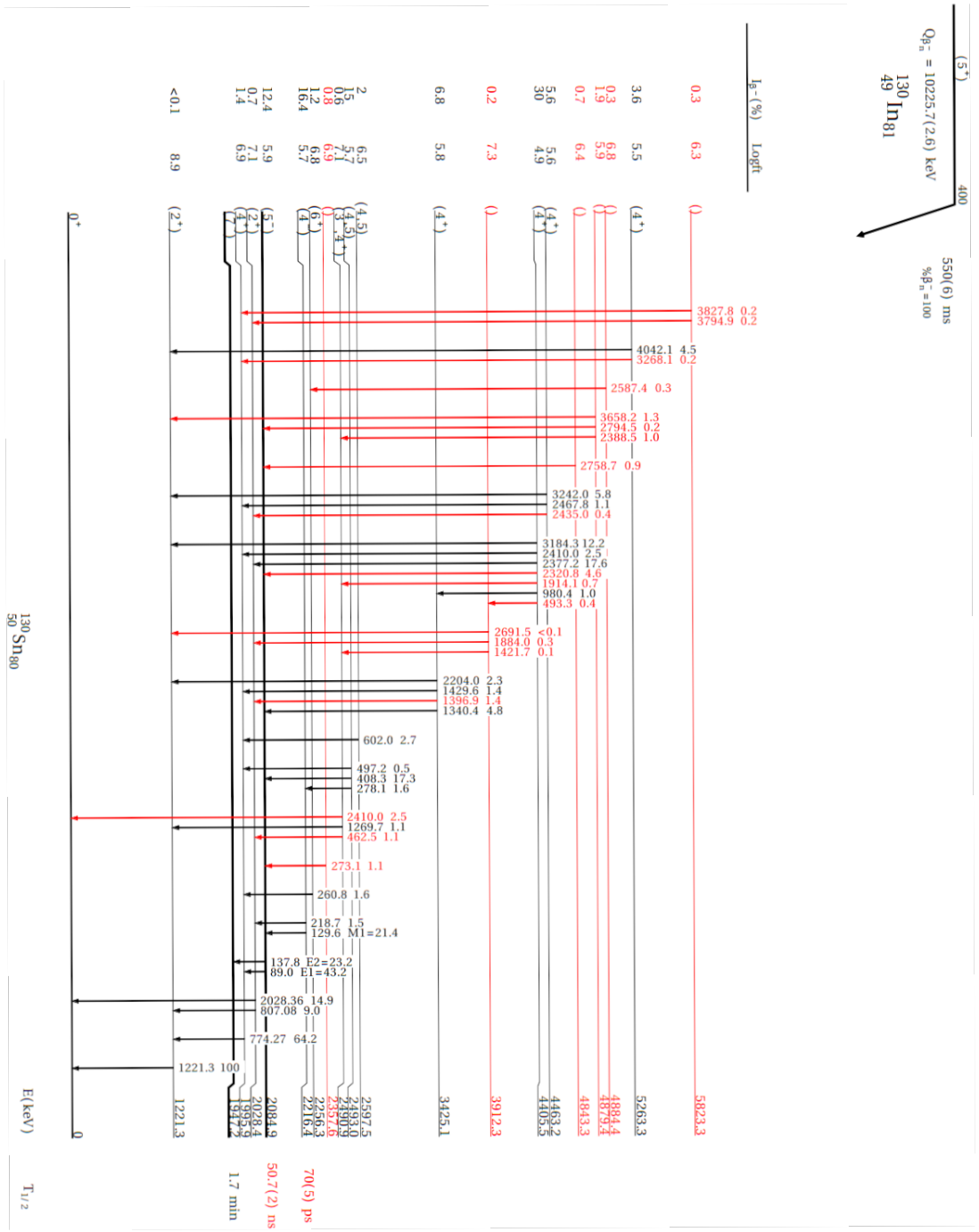

Figure 69: **Proposed Level scheme for ^{130g}Sn following the β-decay of ^{130m2}In.** Level scheme was obtained by studying the γ-γ coincidences. The first number on every transition is the energy of the corresponding γ-ray, while the second number is the relative intensity (in %) respect to the 2258-keV transition. For absolute intensity per 100 decays, multiply by ≈0.86 [Cen].

obtained in [FHS81], and also with the value of 284(10) ms measured in [Lor+15] based on β detection.

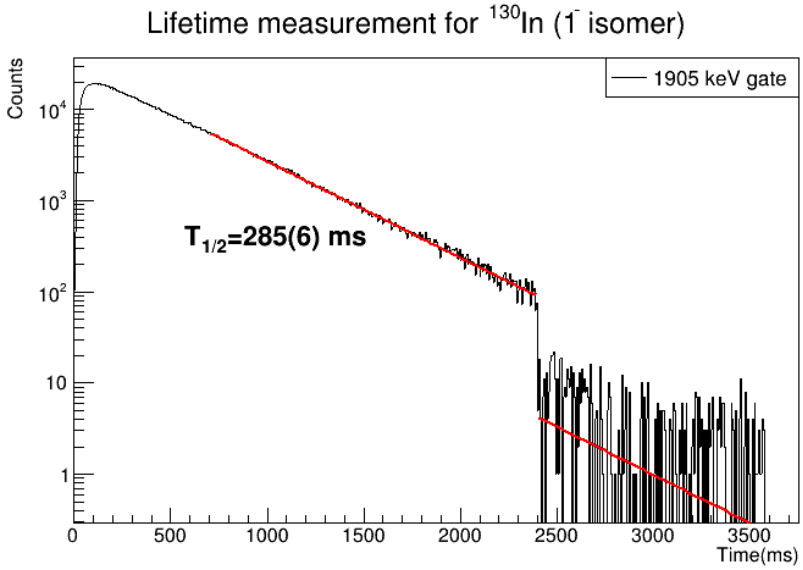

Figure 70: **Time distribution analysis of the ^{130g}In lifetime.** Time distributions relative to the time of the arrival of the last proton pulse. In order to extract the lifetime, an exponential fit in both regions has been performed. The region, ≈550-3500ms, has been adjusted to reduce dead-time effects.

7.4.2 ^{130m1}In lifetime measurement

Similarly to the ground state of the ^{130}In, the lifetime of the ^{130m1}In isomer has been measured by analysis of the most characteristic γ rays of the isomer populated in the β decay by HPGe-HPGe slow timing. From the level scheme displayed in Figure 67 the 2258-keV γ ray was used, from the de-excitation from 9^- level at 4206.7 keV to the 7^- ^{130m1}In state at 1946.8 keV. This transition is selected since it is only observed in the decay of the ^{130m1}In state, so no other contributions to the lifetime measurement should be expected. Figure 71 represents the time distribution analysed in this section. The adopted final lifetime value is $T_{1/2}$=493(10) ms, which is in agreement with the 0.53(3) s obtained in [FHS81] for both the 10^- and 5^+ β-decaying states. In this work we have been able to provide separate lifetimes for each.

7.4.3 ^{130m2}In lifetime measurement

In order to extract the lifetime of the ^{130m2}In state the γ rays of 2377 and 3184 keV have been employed. Both de-excite a 4^+ level located 4463.2 keV above the ground state with similar intensities. Having similar intensities favours the distribution of statistics between both of them (contrary to the ^{130g}In case). Both of the time distributions can be seen in Figure 72.

The two values obtained from the fit are in good agreement with each other and with the 0.53(3) s measured in [FHS81] for the combined 10^- and 5^+ isomers,

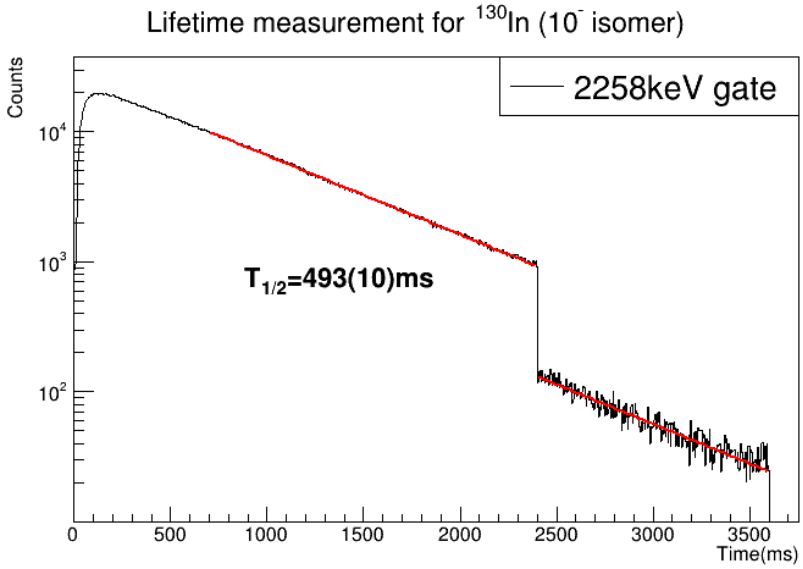

Figure 71: **Time distribution analysis of the ^{130m1}In lifetime.** Time distributions relative to the time of the arrival of the last proton pulse. In order to extract the lifetime, an exponential fit in both regions has been performed. The region, ≈550-3500ms, has been adjusted to reduce dead-time effects.

but with better precision. They are also in agreement with the adopted value of 0.54(1) s [SIN01] for the two 10^- and 5^+ isomers. The adopted half-life independent value from the weighted mean for the ^{130m2}In (5^+) state is $T_{1/2}$=550(6) ms.

7.5 Lifetime measurements of excited states in ^{130}Sn

This section focuses on the lifetime measurements of the ^{130}Sn excited states. Several lifetimes can be extracted from the data sets, ranging from the μs to the hundred of ps range. Longer lifetimes, those in the order of the μs, have been obtained by the coincidence between the β counter and the HPGe detectors, using the time stamps recorded by the DAQ with 100-ns precision. In such case the half-life shows up as a slope in the time distribution, and it is extracted via the slope method, where the half-life of the level comes from the fit of the slope to an exponential decay, usually with a background. Lifetimes in the ns down to the tens of ps range are measured using fast-timing techniques. These methods rely on time differences between two fast detectors, in this analysis the time differences between either the β detector and each of the $LaBr_3$ detectors or between the two $LaBr_3$. The methods employed in the fast-timing analysis are explained in Chapter 2.

When the lifetime under study does not show as a slope on the time distribution, the centroid shift method is employed, as described in Chapter 2. Detailed calibrations are required for the energy dependence of the time response both for Full-energy peaks and Compton events. The FEP walk curve for this experiment

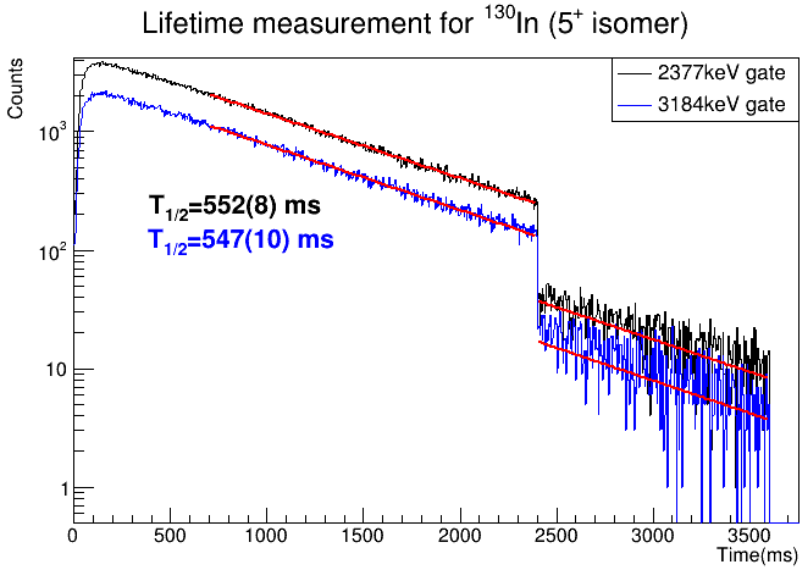

Figure 72: **Time distribution analysis of the ^{130m2}In lifetime.** Time distributions relative to the time of the arrival of the last proton pulse. In order to extract the lifetime, an exponential fit in both regions has been performed. The region, ≈550-3500ms, has been adjusted to reduce dead-time effects.

was done by Dr. Jaime Benito by measuring the system response for ^{140}Ce, ^{138}Ba, ^{152}Sm, ^{152}Gd and ^{88}Sr radioactive sources. These sources have prompt or well known lifetime transitions that allow the study of the experimental set-up over the energy range. The lifetime analysis in this thesis has been performed by using root-based programs developed by Dr. Jaime Benito [Ben]

7.5.1 Measurement of the 10$^+$ level lifetime

The half-life of the 10$^+$ level at 2435.7 keV has been obtained via β-HPGe(γ) from coincidences with the 391-keV transition. This level is populated exclusively in the ^{130m1}In β decay. The lifetime of this level can in principle be obtained by studying the $\beta\gamma$) coincidences of the 96-keV γ ray, but at low energies it is harder to place the energy gate and there is strong background contribution due to the Compton events from higher gammas. No extra selectivity was needed since the 391 keV γ-ray is clearly resolved. The resulting time distribution is displayed in Figure 74. The obtained value for the half-life is T$_{1/2}$=1.488(11) μs which is in good agreement with the reported value from [FHS81] 1.61(16) μs.

7.5.2 2084.9-keV 5$^-$ level lifetime measurement

The half-life of the 2084.9-keV level has been obtained via β-HPGe(γ) coincidences by selecting the 137-keV transition in the HPGe detectors. This level is populated in both the ^{130g}In and ^{130m2}In decay, so both data sets have been used in order to

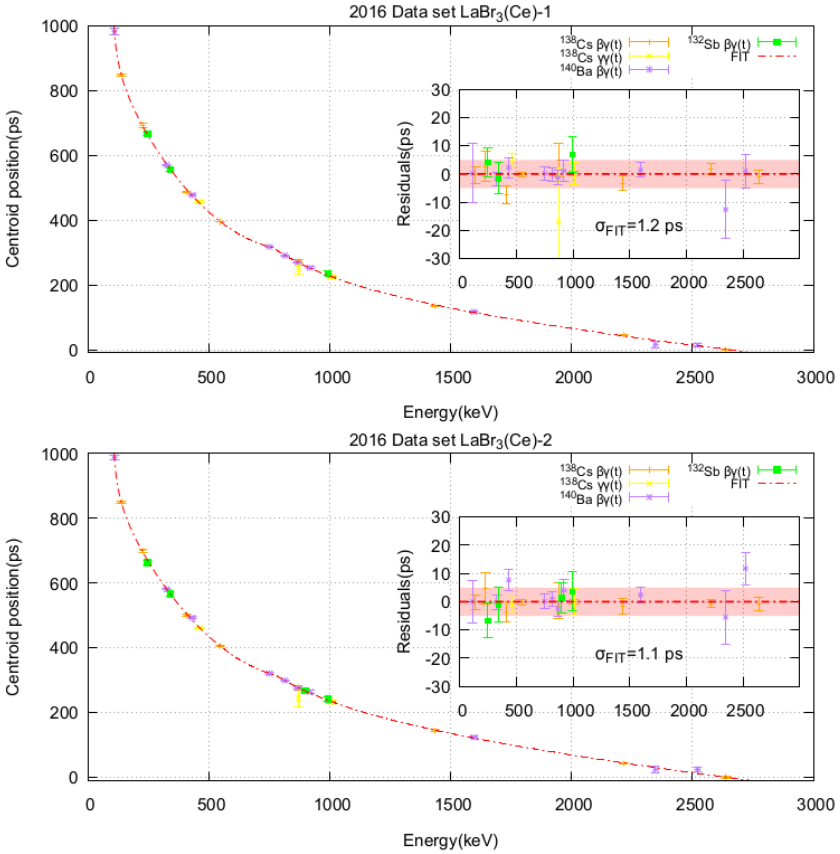

Figure 73: **FEP walk curve for both $LaBr_3$(Ce) detectors for the 2016 measurements.** FEP walk obtained for the IS610 experimental campaign during the 2016 phase. Calibration was performed by Dr. Jaime Benito [Ben] using ^{140}Ce, ^{138}Ba, ^{152}Sm, ^{152}Gd and ^{88}Sr radioactive sources

increase the statistics. The lifetime of this level could in principle also be obtained by studying the $\beta\gamma$ coincidences for the 89-kev γ ray, but at low energies it is much harder to place the energy gate and there is background contribution due to the Compton events from higher gammas. The resulting time distribution is displayed in Figure 75. The obtained value for the half-life is $T_{1/2}$=50.7(2) ns which is in good agreement with the reported value in [FHS81] of 52(3) ns, but with a better precision.

7.5.3 2339.1-keV excited level lifetime measurement

The half-life of the 8^+ excited state at 2339.1 keV has been obtained by $\gamma\gamma(t)$ coincidences with the fast-timing technique using the fast $LaBr_3$(Ce)detectors. The level is populated exclusively in the β decay of ^{130m1}In. The lifetime value has been obtained from the coincidence between the 96-keV and 391-keV γ rays populating and de-exciting the state. The delayed and anti-delayed time distributions are displayed

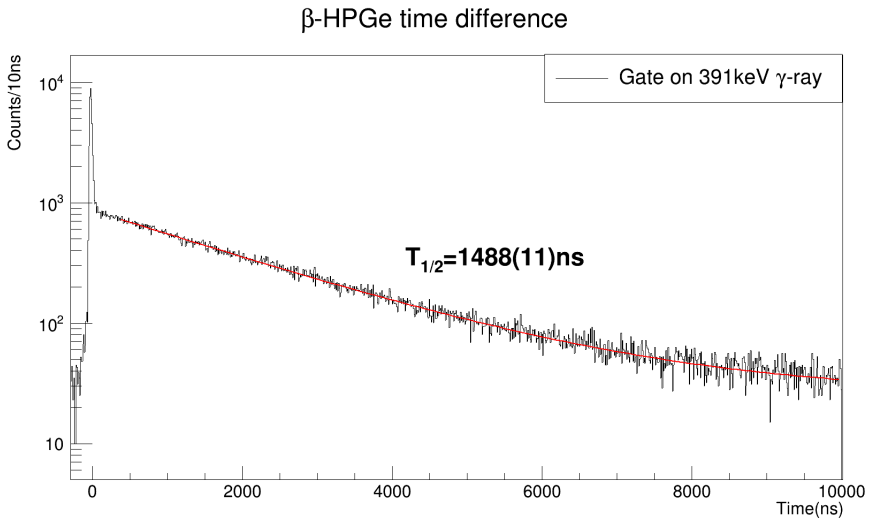

Figure 74: **Time distribution analysis to extract the half-life of the 10^+ 2435.7 keV excited state populated in the ^{130m1}In β decay.** The half-life for the 10^+ excited level has been obtained by fitting the slope to an exponential decay with a background component.

in Figure 76 in red and blue, respectively. Our result is obtained from the weighted mean of both values, which yields $T_{1/2}(8^+)$=321(10) ps for the half-life. This is the first direct measurement, since the previous limit of the half-life of <40ns given in [FHS81] was based on $\beta\gamma$ coincidences with a slow NaI scintillator.

7.5.4 The lifetime of the 4^- 2216-keV state

The half-life of the 2216-keV level has been obtained via $\beta\gamma\gamma(t)$ fast-timing method from coincidences with the 129-keV transition and a selection on the HPGe feeding transition. The level is populated in both the ^{130g}In and ^{130m2}In decay, so both data sets have been added in order to have more statistics. As can be seen in Figure 78, the lifetime measurement is on the limit for the de-convolution method, for that reason the centroid shift has also been employed.

The 1905-keV γ ray has been selected as a gating transition in the HPGe detectors, since it directly populates the level of interest. Figure 77 displays the coincident spectra for both HPGe and $LaBr_3$(Ce) detectors. Because the scintillator detector has difficulty resolving the 129-keV and thee 137-keV full-energy γ peaks, the HPGe is used to aid the selection. The 129- and 219-keV γ rays de-excite the 2216-keV level, but with a 219-keV gate there is not enough statistics to perform the analysis. For this reason the 129-keV gate has been used, but as illustrated it is not easily selected since it cannot be resolved from the 137-keV peak. Both the 89-keV and specifically the 137-keV γ rays come from the 2084-keV excited level, which is populated in the 129keV decay and has a half-life of 50.7(2) ns as discussed above. It should not interfere with this particular measurement on a much shorter timescale.

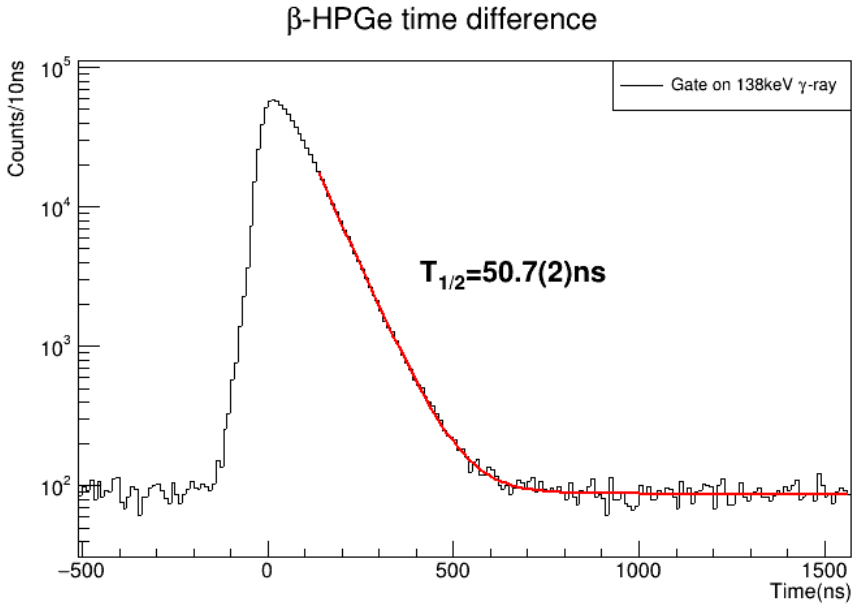

Figure 75: **Time distribution analysis to extract the half-life of the 5^- 2084.9 keV excited state populated in both the ^{130g}In and ^{130m2}In β decay.** Half life for the 5^-excited level has been obtained by the slope method, fitting the slope to an exponential decay with a background.

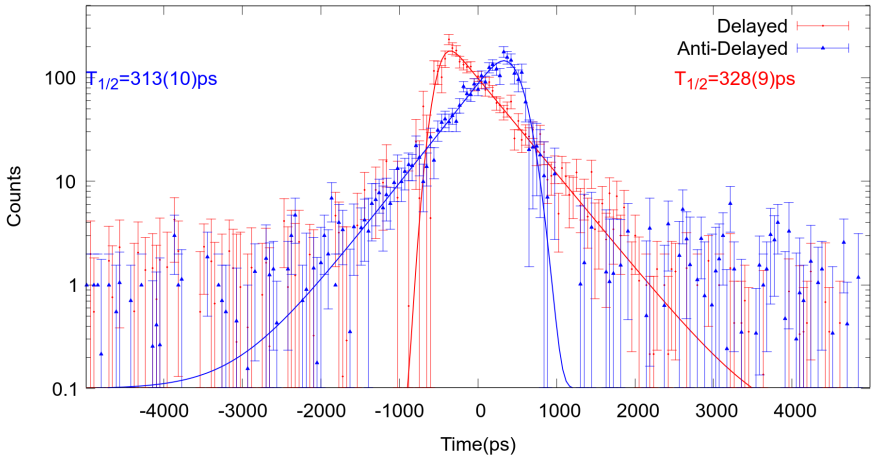

Figure 76: **Time delayed $\gamma\gamma$ analysis of the 96-391 keV coincidence.** The Compton-subtracted time distributions for the 96-391 keV coincidence are shown. The half-life is obtained from fitting the slope to an exponential decay curve.

The lifetime of this level has been obtained via two decays, the 129-keV γ ray and a combined γ-line coincidence gate set on the 129+137-keV peaks. The first one has been chosen by placing the gate towards the left-hand side of the combined 129+137-keV peak (in red in Figure 77) in order to isolate the 129-keV transition.

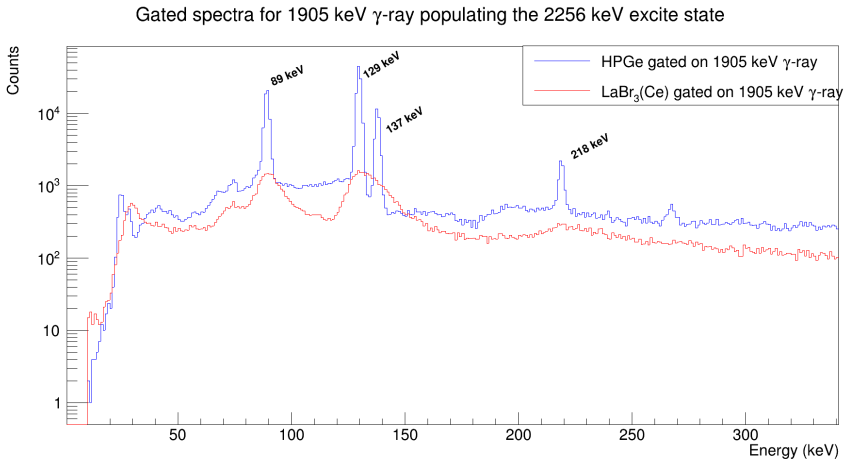

Figure 77: **Coincident spectra for both HPGe and $LaBr_3$(Ce) with the 1905-keV line selected on the HPGe detectors.**

Detector	Gated transition	Method	$T_{1/2}$ (ps)
$LaBr_3$(Ce)-1	1905-129 keV	Slope	63(2)
		Centroid	70(7)
	1905-(129+137) keV	Slope	70(3)
		Centroid	66(8)
$LaBr_3$(Ce)-2	1905-129 keV	Slope	70(2)
		Centroid	69(6)
	1905-(129+137) keV	Slope	68(3)
		Centroid	72(6)

Table 23: **2216 keV state half-lives obtained via the slope and the centroid methods using $\beta\gamma\gamma(t)$ coincidences.**

The time distribution for both $LaBr_3$(Ce) when this selection is used is displayed in 78. In the second case, a combined gate on the 129+137 keV peaks has been selected in order to enhance the statistics at the expense of a long-lived background. This second option should provide a cross-check of the results. The results obtained from the analysis are compiled in Table 23. The weighted mean of the results yields $T_{1/2}$ of 68(3) ps, which we adopt as the final value for the half-life of the 2216-keV state. No previous measurement is available in the literature.

7.6 Results and discussion: Reduced transition probabilities

With N=80, the neutron-rich nucleus ^{130}Sn lacks two neutrons to complete the N=82 magic number. The ordering of the neutron orbitals in the N=50-82 shell, given by the experimental single particle energies [Ben+20], is $\nu g_{7/2}$, $\nu d_{5/2}$, $\nu s_{1/2}$, $\nu h_{11/2}$ and $\nu d_{3/2}$, with the last three levels very close in energy. Therefore, the low-lying

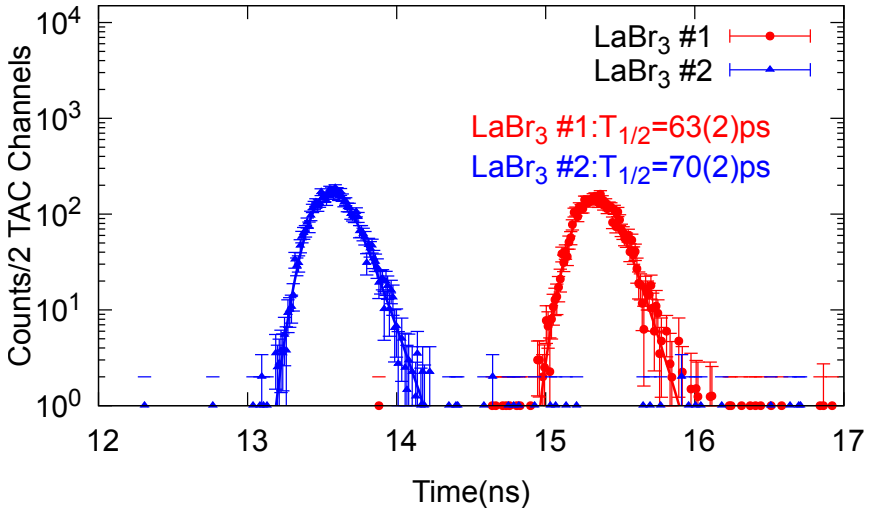

Figure 78: **Time delayed $\beta\gamma\gamma(t)$ fast-timing analysis of the 2216-keV state lifetime.** Compton-subtracted time distributions for the 129-keV γ-ray selected in the $LaBr_3$(Ce) detectors in coincidence with the 1905-keV transition selected in the HPGe detectors. The half-life is obtained from fitting the slope to an exponential decay curve.

structure in ^{130}Sn comes from the two neutron holes in the above configurations.

With a positive parity, the 10^+, 8^+, 6^+ and 4^+ state arise from the $\nu h_{11/2}^{-2}$ configuration, while the lower-lying 0^+ and 2^+ levels may contain both $\nu h_{11/2}^{-2}$ and $\nu d_{3/2}^{-2}$ components. Negative-parity excited states, such as the 7^-, 6^-, 5^- and 4^- ones come from $\nu h_{11/2}^{-1} d_{3/2}^{-1}$ couplings. These excited states with the same spin-parity also exist in the other even-even Sn isotopes, as displayed in Figure 82 as a function of the neutron number. As shown, higher spin levels arise for Sn isotopes with higher neutron seniority. The figure illustrates the evolution of the excitation energy of the relevant states, with the 2^+ staying almost constant while the other ones steadily decrease as neutrons are being added. The crossing of the 7^- and 5^- states from the $\nu h_{11/2} d_{3/2}$ multiplet occurs at N = 128.

The β-decay from ^{130}In populates different levels in ^{130}Sn depending on the starting nuclear state. Two of the β-decaying levels in ^{130}In, the 1^- ground state and 10^- isomer, are expected to arise from proton-neutron couplings based on the $\pi g_{9/2} \nu h_{11/2}^{-1}$ configuration, being the highest and lowest spin members of the multiplet. The β-decaying 5^+ ^{130m1}In isomer is most likely based on the $\nu d_{3/2}^{-1} \pi g_{9/2}$ configuration.

Most of the excited states were identified in the previous β-decay study by Fogelberg *et al.* [FHS81], and tentative spin parities values for some of them were assigned. In order to provide tentative spin-parity assignments for the newly discovered excited states in this work, the direct population in β-decay and electromagnetic transition selection rules have been taken into account. We propose spin-parity as-

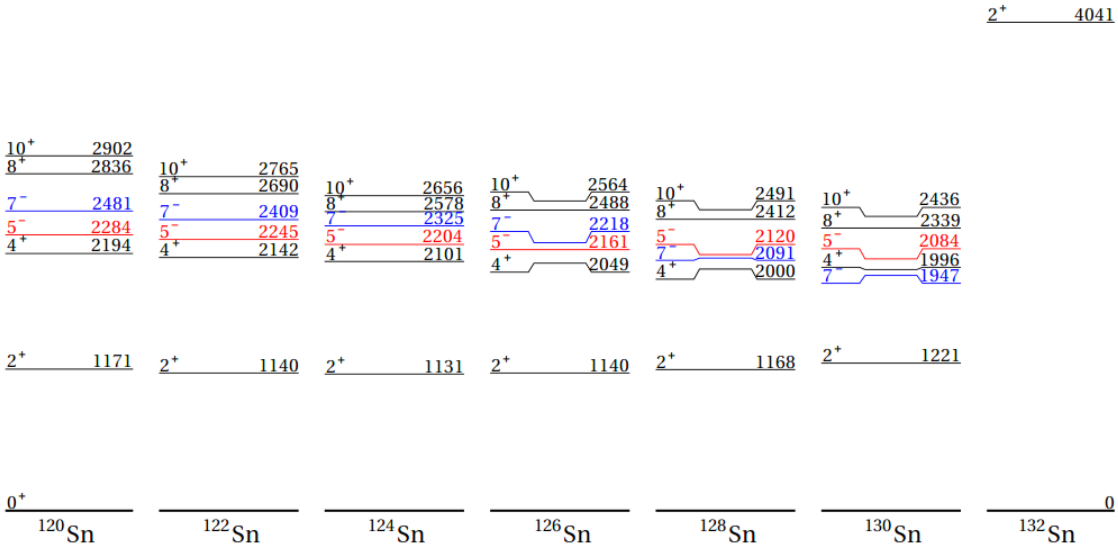

Figure 79: **Systematics of the excited states for even-even Sn isotopes.** Systematics of the excited states for even-even Sn isotopes. Data taken from NNDC [Cen], except for ^{130}Sn, from this work.

signment for two states. The first one, located at 2357.6 keV, has been observed for the first time in this analysis. Its main population mechanism is by direct β feeding from the ^{130m2}In (5^+) state. It de-excites via a 273.1-keV γ-ray to the (5^-) excited level at 2084.9 keV. With this in mind, a tentative (6^-) value has been given to the excited state in ^{130}Sn. With this proposal it should be part of the $\nu h^{-1}_{11/2} d^{-1}_{3/2}$ multiplet, where the 6^- member had not been identified in previous studies. The second excited level is located at 3912.3 keV, and it is populated via direct β-feeding and γ de-excitation from the (4^+) at 4405.5 keV. It decays with three γ-rays that populate (2^+) states located at 1221 and 2028 keV as well as a tentative (3^-,4^+) placed at 2490 keV [FHS81]. The β-decay feeding suggests a first or second forbidden transition and with the electromagnetic selection rules tentative (3^+, 3^-) values could be given to this new level.

The corresponding B(Xλ) have been calculated for the measured lifetimes in ^{130}Sn. Calculations are derived from the lifetimes and the branching ratios obtained in this work, as well as from the theoretical internal conversion coefficients calculated using the BrIcc tool [Uni]. Transition rates have been calculated assuming a pure multipolarity of the transitions using the existing spin and parity assignments [FHS81], and therefore they should be understood as limits in case when mixing is possible. The results are displayed in Table 24.

Reduced transition probabilities calculated can be compared to the ones from the even-even Sn isotopes. The results obtained for the B(E2) transitions can be seen in Figure 80. In red, the E2 reduced transition probability corresponds to the $10^+ \rightarrow 8^+$ transition, present in all the even Sn isotopes. The trend reveals an increase

E_i(keV)	$T_{1/2}$	J_i^Π	E_f(keV)	J_f^Π	E_γ(keV)	I_γ(%)	Xλ	B(λL) (W.u.)
2084.8	50.3(2) ns	5^-	1995.6	4^+	89.2	46.5(1.3)	E1	$2.26\text{x}10^{-6}$
			1947.2	7^-	137.9	30.3(2.0)	E2	1.25
2339.1	321(10) ps	8^+	1947.8	7^-	391	16.1(1.0)	E1	$1.44\text{x}10^{-5}$
2435.7	1.487(6) μs	10^+	2339.1	8^+	96.6	15.1(8)	E2	0.459
2214.48	68(3) ps	4^-	2084.8	5^-	129.5	23.4(2.3)	M1	0.109
			2028.4	2^+	218.7	1.8(2)	M2	2.6

Table 24: **State half-lives and reduced transition probabilities in ^{130}Sn.** Intensities are given per 100 parent decays.

in the collectivity as the number of neutron pairs increases towards the neutron shell closure at ^{132}Sn, except for ^{120}Sn with N=70. A similar effect is displayed for the other E2 transition but, since the 5^- and 7^- excited states change their energy as the neutron number increases, the E2 transition changes from $7^- \rightarrow 5^-$, from ^{120}Sn up to ^{126}Sn, to $5^- \rightarrow 7^-$ for ^{128}Sn and ^{130}Sn. The B(E2) for ^{128}Sn is not displayed in the figure since the lifetime of the 7^- has not been measured. This, however, does not affect the overall behaviour since the values obtained are plotted in Weisskopf units (W.u.) and it is apparent that the magnitude of the E2 transition rate increases as we approach N=82. This behaviour is opposite for the B(E2; $2_1^+ \rightarrow 0_1^+$) transition rates, which strongly diminishes when approaching ^{130}Sn [**Pritychenko2016**].

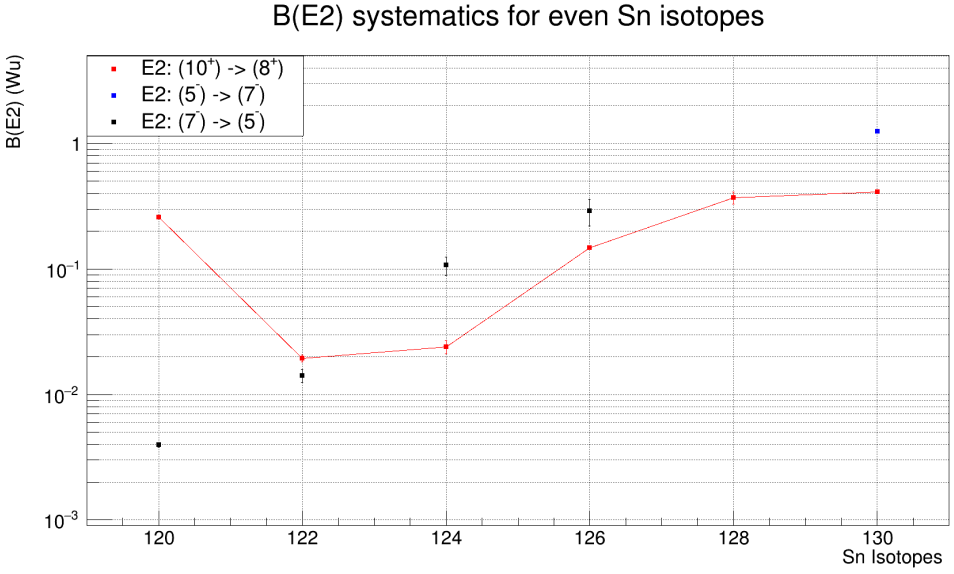

Figure 80: Reduced E2 transition probabilities as a function of A for even Sn isotopes. Values displayed have been taken from reference [Cen], except for those stemming from this thesis work. See text for details.

For completion, the B(E1) transition rates have been calculated and compared to literature values for the same nuclei. They are displayed in Figure 81. For the $8^+ \rightarrow 7^-$ transition only two lifetimes have been measured, belonging to ^{128}Sn and

to ^{130}Sn, measured in this PhD thesis. There is no salient feature in the graph except that B(E1) rates from $5^- \rightarrow 4^+$ are roughly of the same order of magnitude, with some exceptions. E1 transitions connect the two neutron hole configurations $\nu h^{-1}_{11/2} d^{-1}_{3/2}$ and $\nu h^{-2}_{11/2}$.

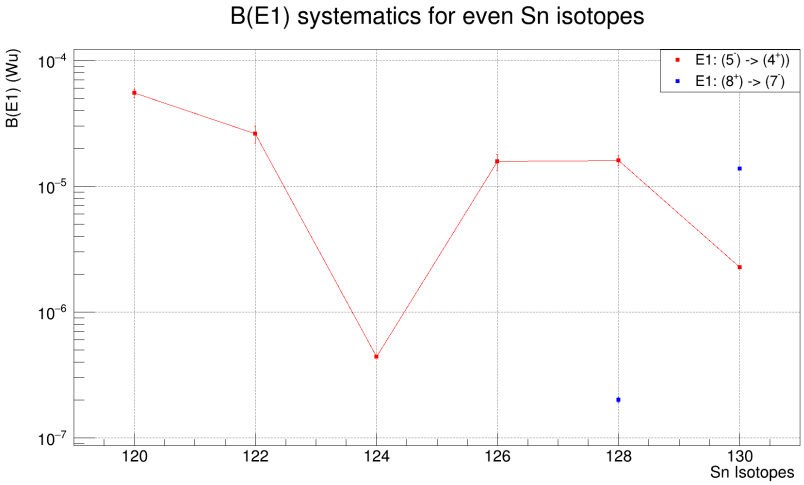

Figure 81: Reduced E1 transition probabilities for the indicated transitions as a function of A for even Sn isotopes. The values have been obtained from [Cen].

There is an interesting point to be made regarding the proposed β-decay scheme of ^{130m1}In to ^{130m1}Sn. The isomeric ^{130m1}Sn state has a proposed spin of 7^- and it is populated from the 8^+ level via an E1 γ transition of 391 keV. From the decays of ^{130gn}In and ^{130m2}In a 6^+ excited state at 2256 keV is populated and a transition between the 8^+ and the 6^+ might be expected, connecting then the three isomerically-populated structures. The transition would occur with an E2 transition of $\approx$82 keV that would compete with the E1 391-keV γ-ray. This E2 decay would then lead to a γ-ray cascade from the 10^+ populated in the ^{130m1}In β decay to 0^+ the ground state, which is directly or indirectly fed in both ^{130g}In and ^{130m2}In β decays. The supposed γ ray of 82 keV should be in coincidence with the 96.6 keV populating the 8^+ level at 2339.1 (Figure 67) but as displayed in Figure 82, there is no obvious γ-ray in the 80 keV region, while the 391 keV coincidence is quite clean, reaffirming the β decay path $10^+ \rightarrow 8^+ \rightarrow 7^-$.

7.7 Summary and conclusions

In this chapter the data analysis from the IS610 experiment regarding the ^{130}Sn nucleus has been described. The experiment was carried out in 2016 using the ISOLDE Decay Station (IDS) located at the ISOLDE facility at CERN. In the experiment, the ^{130}Sn was populated via β-decay of ^{130}In produced via fission of a UC_x target. The excited level scheme of ^{130}Sn has been constructed via double coincidences employing the high resolution HPGe detectors. The study has been

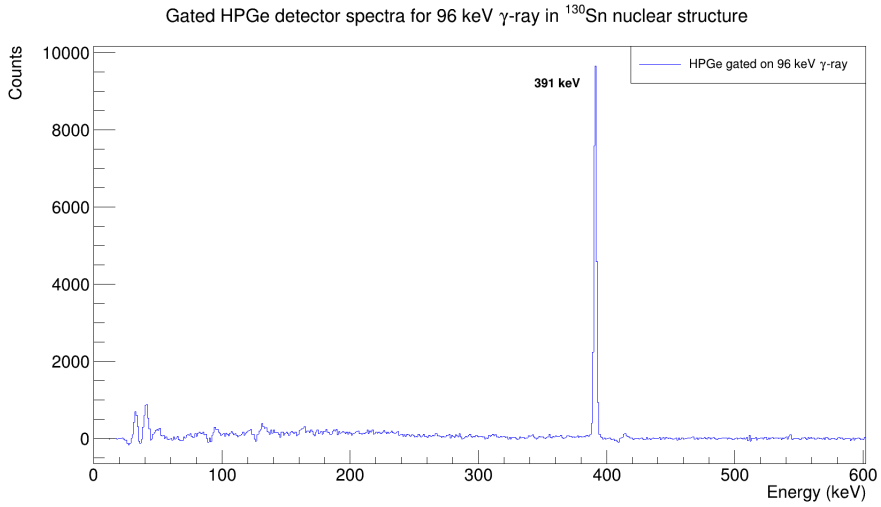

Figure 82: **HPGe detector coincident spectrum with the 96.6 keV γ ray.** The spectrum comes from the data set with the total statistics, the 391 keV γ-ray coincidence that de-populates the 8^+ level at 2339.1 keV to the long-lived 7^- state at 1947.8 keV.

performed for each of the β decays from the three isomeric ^{130}In states, taking advantage from the RILIS selectivity for the ionization of the three known 130 In β decaying isomers. Expanded level schemes are proposed. Eight new γ transitions and 2 new levels have been added to the ^{130m}In decay, while 6 new γ transitions and 6 excited levels have been added to the ^{130m2}In decay. No new γ rays nor excited levels have been added for the decay of ^{130m1}In. In order to obtain the intensities relative to each decay, a clean-up procedure employing the time of arrival of the proton has been employed. Data has been divided into three sets for this method where each isomeric ^{130}In state is produced the most. By studying the ratio between decays in each set of data a relationship between each decay is found. By placing a gate on the proton time of arrival one can control the amount of a non-desired isomer on the data set under study, allowing to clean each of the spectra populated on the different decays.

The β-decay half-lives of the three isomers in ^{130}In have been obtained using the time distribution of HPGe events. The γ rays employed to measure the ^{130}In isomer lifetimes were exclusive to each decay for this reason the 1905-keV (^{130g}In), 2258-keV (^{130m1}In), 2377-keV and 3184-keV (^{130m2}In) γ rays have been selected. The results are in good agreement with literature for ^{130g}In [FHS81] yielding $T_{1/2}$=285(6) ms, while the first independent measurement of the ^{130m1}In and ^{130m2}In is performed, giving $T_{1/2}$=550(6) ms and $T_{1/2}$=493(10) ms, respectively.

Several excited state lifetimes have been measured in the ^{130}Sn and the reduced transition probabilities have been calculated. Two half-lives have been obtained using β-HPGe(t) coincidences that correspond to the (10^+) and (5^-) excited states located at 2434 and 2085 keV above the ground state. The values, 1.48(6) μs for the (10^+) and 50.7(2) ns for the (5^+), are in agreement with the previously measured

ones [FHS81].

Two new lifetimes have been measured and correspond to the levels (8^+) and (6^+) located at 2338 and 2256 keV respectively. Both lifetimes have been extracted with fast-timing measurements. The (8^+) half-life has been obtained with the 96-391 keV $\gamma\gamma$(t) coincidence with the $LaBr_3$(Ce) detectors, and yields a value of 321(10) ps. The (6^+) half-life has been extracted with the full $\beta\gamma\gamma$(t) measurement using the 129-keV transition and a HPGe selection on the 1905-keV transition. It yields a half-life value of 68(3) ps.

The knowledge about ^{130}Sn has been expanded by the β-decay of isomeric states from ^{130}In investigated at ISOLDE facility at CERN. To the previous known level scheme of the nuclei, 8 excited levels and 14 new γ-ray have been assigned. Beta-decay ^{130}In half-lives have been reviewed and given a more precise value. ^{130}Sn half-lives have been studied and revised, giving more precise values to the previously known lifetimes and obtaining two new lifetimes for this nucleus.

8 Conclusions and outlook

Neutron-rich nuclei far from the stability line provide key information on the evolution of nuclear structure in exotic regions of the nuclear landscape. The region near the double magic ^{132}Sn (Z=50,N=82) draws particular attention due to the observed modifications of the shell structure and the arising collective behaviour. In this thesis we have studied two nuclei with A=130 in the proximity of this region, ^{130}I (Z=53, N=77) and ^{130}Sn (Z=50, N=80).

For the study of these nuclei, fast-timing methods have been employed to access lifetimes of excited states down to the 10 ps range. Lifetime measurements are relevant because they grant access to reduced transition probabilities, which allow a better understanding of the nuclear states, help to compare experimental data with proposed theoretical models, and may point towards collective behaviour and modifications of the standard shell configurations. These methods rely on fast scintillator detectors that are capable of measuring the time difference between the radiation populating and de-populating the excited level under study.

Nowadays, the usual choice of scintillator detectors for fast-timing applications resides in state-of-the-art $LaBr_3$(Ce) crystals coupled to Photomultiplier Tubes (PMT) used as photosensors. Nonetheless PMTs may not be the optimal choice under certain conditions due to their sensibility to magnetic fields, inhomogeneities due to manual fabrication and sometimes price. Magnetic recoil separators or fission fragment separation allow for a nuclei selection, hence their implementation in gamma spectroscopy and fast-timing experimental set-ups will provide an advantage to reach more exotic nuclei. One of these experimental set-ups to combine such magnetic field separators with a high-sensitivity HPGe array will be located at Institut Laue Langevin (ILL): the Fission Product Prompt γ-ray Spectrometer (FIPPS). This instrument is made of 8 segmented HPGe detectors that can be coupled to several ancillary devices in order to perform experimental campaigns that suit the need of users coming to the ILL, with the expectation that it will allow for further understanding of neutron-rich nuclei and of the fission process itself. Currently on phase 2 of its development, FIPPS will be complemented with a recoil spectrometer based on a gas-filled magnet, rendering PMTs not optimal for timing measurements. With this background in mind, this thesis has also been focused on the development of a magnetically-compatible readout for $LaBr_3$(Ce) detectors in order to be able to perform fast-timing experiments.

The results obtained in this thesis for both of the analyses of the structure of ^{130}I and ^{130}Sn, and on the detector development are outlined below.

Silicon-Photomultiplier-array readout for $LaBr_3$(Ce) crystals

In the first part of the thesis, the focus has been on the development of a magnetically-compatible readout for fast scintillators. The reason behind this development is the future implementation of a recoil spectrometer based on a gas filled magnet at the FIssion Product Prompt γ-ray Spectrometer (FIPPS) at the Institut Laue Langevin (ILL).

Two Silicon Photomultiplier (SiPM) based arrays have been developed with the readout to provide a standard and a fast output. Both of the arrays are made from Onsemi (previously SenSL) sensors: one is a commercially-available MicroFJ-30035-TSV array and the other is custom-built with the MicroFJ60035-TSV sensor array. The 30035-TSV is a square-shaped array that covers $\sim$65% of the scintillator $LaBr_3$(Ce) crystal used for the tests. On the other hand, the 60035-TSV-based array has a quasi-circular shape that covers basically the whole of the crystal coupling area. In order to characterize both of the arrays a truncated cone $LaBr_3$(Ce) crystal with is 1.5" height and 1" and 1.5" diameter bases has been employed.

The selection of both of the sensors is based on the two outputs provided by Onsemi sensors: the standard and the fast outputs. The fast output has a lower capacitance and a faster rise time, which makes it useful to determine the time of arrival of incoming signals, while the standard output has a slower rise time and a much larger capacitance, and it is better suited for spectroscopy measurements. The idea behind the readout is similar to the way the customized Hamamatsu R9779 PMT works, since it provides two outputs as well: a fast negative signal and a slower positive one. This PMT has been chosen since it's used on fast-timing experiments due to its very fast time response and linearity, combined with good energy resolution. One of the main differences between the chosen SiPM array and the PMT is the number of outputs that it provides, the PMT provides 2 but the SiPM provides two per sensor on the array so an active approach when developing the readout has been performed. This method groups the fast signals and extracts the fastest arriving to each group via the Schottky diodes while the standard output signals are all summed up.

The characterization of each array has been performed by coupling them to a $LaBr_3$(Ce) crystal and comparing the performance to the aforementioned R9779 PMT. The main results are described below:

- At 29 V of power supply, the energy response of the SIPM-based detectors is competitive with the R9779 PMT, yielding values of 3.7(%) and 3.9(%) of energy resolution at FWHM against the 4.0(%) obtained with the PMT tube at ^{137}Cs energies. At this voltage both types of detectors behave linearly in the 120-1408 keV range and have similar γ-ray detection efficiency making the SiPM based detector a good alternative for spectroscopy measurements.

- The best time resolution for both of the arrays has been obtained at 32 V of power supply. The intrinsic time resolution for the SiPM detectors is 239(12) and 262(12) ps for the 30035-TSV and the 60035-TSV arrays respectively,

while the PMT had a reported value of 110(3) ps at ^{60}Co energies. At this voltage the energy resolution slightly drops to a 4.0(%) and a 4.3(%) for the 30035-TSV and 60035-TSV arrays, respectively. The time dependence of the supply applied to the Schottky diode has been studied and it does not affect the time resolution.

- The time walk for both of the arrays has been tested and the SiPM based detectors can be used in fast-timing measurements since it can be controlled.

- Energy resolution dependence with the surface covered of the detector show that not all the area has to be covered in order to be competitive with the R9779 PMT tube. This may be a promising step towards reducing the number of sensors and enhancing the time resolution.

- Due to a lower capacitance, the 30035-TSV array has a better time response than the 60035-TSV. This difference of approximately 20 ps difference, combined with the previous points, suggests that a custom-made quasi-circular array made of 30035-TSV array covering more area would be more competitive against a PMT than the 60035-TSV one.

- The suggested supply voltage for the SiPM-based arrays is 31 V since it gives a compromise between a competitive energy resolution against the PMT, while maintaining a time resolution below 300 ps .

As a first version of the detector, both of the SiPM based arrays have a slightly better energy response than the current PMT used in fast-timing measurements. On the other hand, the time resolution is still far from being competitive with the PMT-based detector for this kind of crystals. However, it cannot be said that the detector is slow since it yield time resolution values of $\sim$250 ps, which is similar to responses of larger detectors and the resolution obtained in multi-channel digital processing. Another advantage of SiPM is their development, since new versions make it to the market with faster and more compact sensors. This, combined with future updates to the readout such as reducing the rise time of the fast output, could still make SiPM-based arrays a competitive alternative to current PMTs. Further work is still required on this field.

Structure of ^{130}I (Z=53, N=77)

The second block of this thesis is the experimental analysis of ^{130}I populated by the ^{129}I(n,γ)^{130}I reaction performed by the impact of thermal neutrons onto a PbI_2 target. The experiment took place on FIPPS at ILL. For the experimental campaign, the HPGe detector array was coupled to 16 $LaBr_3$(Ce) detectors in order to measure lifetimes down to the 10-ps range. In order to perform the measurements

by the electronic coincidences required in the fast-timing method, the multiplexed-start/multiplexed-stop method was implemented since it optimizes the amount of analogue modules require to perform the technique. The radioactivity from the β-decay of ^{130}I to ^{130}Xe has hampered the analysis to a large extent.
The main conclusions of this investigation are summarized below.

- Compared to the published work the level scheme does not show any new levels nor γ transition.
- Several lifetimes of excited levels have been measured. A limit has been set in the $(3,4,5)^-$ excited level at 761 keV, yielding $T_{1/2} \leq 21$ ps, which is on the limit of the technique employed.
- A new lifetime for the $(3,4)^-$ excited level at 353 keV has been obtained via the centroid shift method. The half-life for this level is $T_{1/2}=24(9)$ ps.
- The half-life of the $(4)^-$ excited level at 296 keV has been obtained for the first time via the de-convolution method. The measured value for this half-life is $T_{1/2}=129(6)$ ps.
- The half-life of $(5)^-$ excited level at 245 keV has been measured for the first time with the centroid shift method. The half-life has a value of $T_{1/2}=45(13)$ ps.
- Reduced transition probabilities have been obtained from the above-mentioned half-lives pointing to the M1 nature of the transitions involved.

Structure of ^{130}Sn (Z=50, N=80)

The last block of this thesis has been aimed at the study of the nuclear structure of ^{130}Sn populated in the β-decay of ^{130}In. Data analysed was obtained in the IS610 experiment carried out in 2016 at the ISOLDE facility at CERN. The experiment took place on the ISOLDE Decay Station (IDS), where the time difference was measured with two $LaBr_3$ detectors and a β plastic in a standard fast-timing set up. In order to construct the level scheme HPGe detectors were employed. By taking advantage of the isomer selectivity capabilities from the RILIS ion-source, independent investigations of the β decay of the ^{130g}In (1^-), ^{130m1}In (10^-) and ^{130m2}In (5^+) populating the ^{130}Sn excited states has been performed.
The main conclusions of this part of the thesis are as follows:

- The β-decays from the isomeric states in ^{130}In have been investigated independently by implementing a procedure to clean the spectra from the isomer-enhanced data sets. Once separated, the intensities of the decay γ rays have been obtained via the singles spectra for each of the three isomers.

- The β-decay half-lives have been measured for the three β-decaying ^{130}In isomeric states. The lifetime measurements have been performed using the HPGe time stamps and the time from proton impact, yielding results of 285(6) ms, 493(10) ms and 550(6)ms for ^{130g}In (1^-), ^{130m1}In (10^-) and ^{130m2}In (5^+), respectively. These values are in good agreement with the previously measured one when available, but with better precision. Independent values for the (10^-) and (5^+) states are provided for the first time.

- The level scheme of ^{130}Sn has been expanded with 8 new excited levels and 14 new γ-rays

- Via β-HPGe(t) and HPGe-HPGe(t) coincidences the ^{130}Sn 10^+ and 5^- state lifetimes have been revised. The 10^+ state is populated in the ^{130m1}In decay and yields a value of $T_{1/2}$=1.48(6) μs. The 5^- excited level is populated in the other two β-decays, ^{130g}In (1^-) and ^{130m2}In (5^+); we have obtained a value of $T_{1/2}$=50.7(2) ns. Both are in agreement with the previously available measurements, but with enhanced precision.

- The lifetime of the 8^+ state populated on the ^{130m1}In has been measured using fast-timing methods for the first time. It yields a value of $T_{1/2}$=321(10) ps, confirming the E1 character of the 391-keV de-exciting transition in [FHS81].

- The lifetime of the 6^+ state populated in both the ^{130g}In and the ^{130m2}In β-decay has been measured for the first time. It yields a value of $T_{1/2}$=68(3) ps, consistent with the E2 multipolarity of the connecting transition to the 4^+ state.

- The excited states in ^{130}Sn keep a certain resemblance to core-breaking states in the doubly-magic ^{132}Sn.

As final summary of the thesis, we underline that two SIPM-based detectors have been developed and have been fully characterized in order to investigate whether SIPMs can compete in the nuclear spectroscopy field against the PMTs. Both of the proposed arrays display better spectroscopic qualities than the usual PMT employed for fast-timing measurements, however the time response of the SIPM-based detectors is still slower than the PMT-based ones, although maintaining a good time response below the 300 ps barrier. Since SiPM is in constant evolution and updates will be implemented into the readout in the future, there is still hope that the SiPM-based detector could achieve a better time response that could compete against PMT-based detectors. The future of this detector could have a great impact on current fast-timing set-ups, allowing the use of the technique in locations where a gas based spectrometer is used for mass selection of the desired nucleus, such as the one planned at FIPPS.

The excited structure of two A=130 nuclei have been studied on this thesis: ^{130}I and ^{130}Sn. Both of them are in the region of the doubly-magic ^{132}Sn and their nuclear

structure may provide information on how the behaviour evolves when we approach the doubly-magic shell closure. Lifetimes have been extracted on both nuclei using fast-timing methods in two different experimental set-ups (IDS and FIPPS). The nuclear structure for both nuclei has been studied and new information has been added to the previous information available in the literature.

The measurement of the neutron capture reaction at FIPPS populating the structure of ^{130}I illustrates the potential of the instrument for capture and fission measurements, once the magnetic selection capabilities are included. The inclusion of a fast-timing array based on SiPM readout will be of paramount importance to enhance the reach of the new device. On the other hand, fission is a powerful tool to populate highly-excited states among other nuclei in ^{130}Sn, and this possibility will be explored in the future at FIPPS, with the hope of finding feeding transitions to the known long-lived isomers.

List of Figures

List of Tables

References

[Adr+05] P. Adrich et al. "Evidence for Pygmy and Giant Dipole Resonances in ^{130}Sn and ^{132}Sn". In: *Phys. Rev. Lett.* 95 (13 Sept. 2005), p. 132501. DOI: 10.1103/PhysRevLett.95.132501. URL: https://link.aps.org/doi/10.1103/PhysRevLett.95.132501.

[Ahm07] Syed Naeem Ahmed. *Physics and engineering of radiation detection*. Academic Press, 2007.

[And+06] V Andreev et al. "A high-granularity plastic scintillator tile hadronic calorimeter with APD readout for a linear collider detector". In: *Nuclear Instruments and Methods in Physics Research Section A: Accelerators, Spectrometers, Detectors and Associated Equipment* 564.1 (2006), pp. 144–154.

[Arm+76] P Armbruster et al. "The recoil separator Lohengrin: Performance and special features for experiments". In: *Nuclear instruments and Methods* 139 (1976), pp. 213–222.

[Ben] J. Benito. "PhD thesis: Gamma and fast-timing spectroscopy of exotic tin isotopes around ^{132}Sn". In: ().

[Ben+20] J Benito et al. "Detailed spectroscopy of doubly magic Sn 132". In: *Physical Review C* 102.1 (2020), p. 014328.

[Ben22] J. et al. Benito. In: *Phys. Rev. C* (2022).

[Bil+08] A Biland et al. "First detection of air shower Cherenkov light by Geigermode-Avalanche Photodiodes". In: *Nuclear Instruments and Methods in Physics Research Section A: Accelerators, Spectrometers, Detectors and Associated Equipment* 595.1 (2008), pp. 165–168.

[Bla+13] A Blanc et al. "Spectroscopy of neutron rich nuclei using cold neutron induced fission of actinide targets at the ILL: The EXILL campaign". In: *EPJ Web of Conferences*. Vol. 62. EDP Sciences. 2013, p. 01001.

[Bla+15] A Blanc et al. "From EXILL (EXogam at the ILL) to FIPPS (FIssion Product Prompt γ-ray Spectrometer)". In: *EPJ Web of Conferences*. Vol. 93. EDP Sciences. 2015, p. 01015.

[BM75] A. Bohr and B. Mottelson. "Nuclear Structure". In: *Benjamin* (1975).

[Bon+09] G Bonanno et al. "Precision measurements of photon detection efficiency for SiPM detectors". In: *Nuclear Instruments and Methods in Physics Research Section A: Accelerators, Spectrometers, Detectors and Associated Equipment* 610.1 (2009), pp. 93–97.

[Bon+19] M Bonesini et al. "Study on SiPM breakdown voltage, dark current and gain from room down to liquid nitrogen temperature". In: *Nuclear Instruments and Methods in Physics Research Section A: Accelerators, Spectrometers, Detectors and Associated Equipment* 936 (2019), pp. 192–194.

[Bro+05] BA Brown et al. “Magnetic moments of the 2 1+ states around Sn 132”. In: *Physical Review C* 71.4 (2005), p. 044317.

[Cat+17] R Catherall et al. “The ISOLDE facility”. In: *Journal of Physics G: Nuclear and Particle Physics* 44.9 (2017), p. 094002.

[Cen] National Nuclear Data Center. *"NNDC"*. Tech. rep. URL: `https://www.nndc.bnl.gov/`.

[Cer+04] R Cerulli et al. “Performances of a BaF2 detector and its application to the search for β β decay modes in 130Ba”. In: *Nuclear Instruments and Methods in Physics Research Section A: Accelerators, Spectrometers, Detectors and Associated Equipment* 525.3 (2004), pp. 535–543.

[Cha] Colourfull Nuclide Chart. *"Colourfull Nuclide Chart"*. Tech. rep. URL: `https://people.physics.anu.edu.au/~ecs103/chart/`.

[Che+16] A Chebboubi et al. “Development of a Gas Filled Magnet spectrometer within the FIPPS project”. In: *Nuclear Instruments and Methods in Physics Research Section B: Beam Interactions with Materials and Atoms* 376 (2016), pp. 120–124.

[Chm+17] V Chmill et al. “Study of the breakdown voltage of SiPMs”. In: *Nuclear Instruments and Methods in Physics Research Section A: Accelerators, Spectrometers, Detectors and Associated Equipment* 845 (2017), pp. 56–59.

[Chr+95] N L Christensen et al. “Positron emission tomography within a magnetic field using photomultiplier tubes and lightguides”. In: *Physics in Medicine Biology* 40.4 (Apr. 1995), p. 691. DOI: `10.1088/0031-9155/40/4/014`. URL: `https://dx.doi.org/10.1088/0031-9155/40/4/014`.

[Cie+16] N Cieplicka-Oryńczak et al. “Approaching complete low-spin spectroscopy of Bi 210 with a cold-neutron capture reaction”. In: *Physical Review C* 93.5 (2016), p. 054302.

[Dro+08] W Drozdowski et al. “CeBr _{3} Scintillator Development for Possible Use in Space Missions”. In: *IEEE Transactions on Nuclear Science* 55.3 (2008), pp. 1391–1396.

[Dun+19] R. Dunlop et al. “β decay and β-delayed neutron decay of the $N = 82$ nucleus $^{131}_{49}\mathrm{In}_{82}$”. In: *Phys. Rev. C* 99 (4 Apr. 2019), p. 045805. DOI: `10.1103/PhysRevC.99.045805`. URL: `https://link.aps.org/doi/10.1103/PhysRevC.99.045805`.

[Dut+22] S Dutt et al. “Large-scale shell-model calculations near mass region 100-130”. In: *Indian Journal of Pure & Applied Physics (IJPAP)* 58.4 (2022), pp. 308–313.

[Eck+10] Patrick Eckert et al. “Characterisation studies of silicon photomultipliers”. In: *Nuclear Instruments and Methods in Physics Research Section A: Accelerators, Spectrometers, Detectors and Associated Equipment* 620.2-3 (2010), pp. 217–226.

[Eig+16] Gerald Eigen et al. “SiPM gain stabilization studies for adaptive power supply”. In: *arXiv preprint arXiv:1603.00016* (2016).

[Fed+17] Valentin Fedosseev et al. “Ion beam production and study of radioactive isotopes with the laser ion source at ISOLDE”. In: *Journal of Physics G: Nuclear and Particle Physics* 44.8 (2017), p. 084006.

[FHS81] B Fogelberg, K Heyde, and J Sau. “Energy levels and transition probabilities in 130Sn”. In: *Nuclear Physics A* 352.2 (1981), pp. 157–180.

[Fir19] FirstSensor. *First Sensor, “Introduction to silicon photomultipliers (SiPMs).* Tech. rep. First Sensor), 2019. URL: `https://www.first-sensor.com/cms/upload/appnotes/AN_SiPM_Introduction_E.pdf)`.

[Fog+85] B. Fogelberg et al. “Three β-decaying isomers of ^{130}In”. In: *Phys. Rev. C* 31 (3 Mar. 1985), pp. 1026–1028. DOI: `10.1103/PhysRevC.31.1026`. URL: `https://link.aps.org/doi/10.1103/PhysRevC.31.1026`.

[Gar+14] E Garutti et al. “Afterpulse effect in SiPM and neutron irradiation studies”. In: *2014 IEEE Nuclear Science Symposium and Medical Imaging Conference (NSS/MIC)*. IEEE. 2014, pp. 1–7.

[Glo+05] J Glodo et al. “Effects of Ce concentration on scintillation properties of LaBr/sub 3: Ce”. In: *IEEE Transactions on Nuclear Science* 52.5 (2005), pp. 1805–1808.

[GMS19] M Grodzicka-Kobylka, M Moszyński, and T Szczęśniak. “Silicon photomultipliers in gamma spectroscopy with scintillators”. In: *Nuclear Instruments and Methods in Physics Research Section A: Accelerators, Spectrometers, Detectors and Associated Equipment* 926 (2019), pp. 129–147.

[Ham] Hamamatsu. *Hamamatsu Photonics. Photomultiplier Tube H6610 Specifications.* Tech. rep.

[Ham21] Hamamatsu. *Technical note:"MPPC 1S13360 series"*. Tech. rep. Hamamatsu, 2021. URL: `https://www.hamamatsu.com/content/dam/hamamatsu-photonics/sites/documents/99_SALES_LIBRARY/ssd/s13360_series_kapd1052e.pdf`.

[Hop+73] PK Hopke et al. “Radioactive Decay of I m 130, I g 130, and Cs 130 to Levels of Xe 130”. In: *Physical Review C* 8.2 (1973), p. 745.

[IDS] IDS. *THe IDS collaboration.* Tech. rep. URL: `http://isolde-ids.web.cern.ch/isolde-ids/.`.

[Isk+14] ŁW Iskra et al. “Higher-seniority excitations in even neutron-rich Sn isotopes”. In: *Physical Review C* 89.4 (2014), p. 044324.

[Jen+17] M Jentschel et al. "EXILL—a high-efficiency, high-resolution setup for γ-spectroscopy at an intense cold neutron beam facility". In: *Journal of instrumentation* 12.11 (2017), P11003.

[JK94] Valentin T Jordanov and Glenn F Knoll. "Digital synthesis of pulse shapes in real time for high resolution radiation spectroscopy". In: *Nuclear Instruments and Methods in Physics Research Section A: Accelerators, Spectrometers, Detectors and Associated Equipment* 345.2 (1994), pp. 337–345.

[Jol+15] J Jolie et al. "The (n, γ) campaigns at EXILL". In: *EPJ Web of Conferences*. Vol. 93. EDP Sciences. 2015, p. 01014.

[Jor+94] Valentin T Jordanov et al. "Digital techniques for real-time pulse shaping in radiation measurements". In: *Nuclear Instruments and Methods in Physics Research Section A: Accelerators, Spectrometers, Detectors and Associated Equipment* 353.1-3 (1994), pp. 261–264.

[Kan+13] A. Kankainen et al. "Isomeric states close to doubly magic ^{132}Sn studied with the double Penning trap JYFLTRAP". In: *Phys. Rev. C* 87 (2 Feb. 2013), p. 024307. DOI: 10.1103/PhysRevC.87.024307. URL: https://link.aps.org/doi/10.1103/PhysRevC.87.024307.

[KCB74] A. Kerek, P. Carlé, and S. Borg. "Beta decay studies in the vicinity of 13250Sn82: Excited states in 13051Sb, 13052Te and 13252Te". In: *Nuclear Physics A* 224.2 (1974), pp. 367–395. ISSN: 0375-9474. DOI: https://doi.org/10.1016/0375-9474(74)90694-0. URL: https://www.sciencedirect.com/science/article/pii/0375947474906940.

[Kim+20] YH Kim et al. "Development of a gas filled magnet for FIPPS phase II". In: *Nuclear Instruments and Methods in Physics Research Section B: Beam Interactions with Materials and Atoms* 463 (2020), pp. 269–271.

[Kno10] Glenn F Knoll. *Radiation detection and measurement*. John Wiley & Sons, 2010.

[Kra91] Kenneth S Krane. *Introductory nuclear physics*. John Wiley & Sons, 1991.

[LFA00] Sergey V Los, James Edward Freeman, and Sam Atac. *A low cost SIPM evaluation and control prototyping system including accurate bias voltage generation, leakage current measurement, and temperature control using Peltier cooling*. Tech. rep. Fermi National Accelerator Lab.(FNAL), Batavia, IL (United States), 1900.

[LFA21] Sergey V Los, James Edward Freeman, and Sam Atac. *Hamamatsu Photonics Technical note: "MPPC"*. Tech. rep. Hamamatsu Photonics K.K. (China, EU, Japan, Korea, Switzerland, UK, U.S.A.), 2021. URL: https://www.hamamatsu.com/content/dam/hamamatsu-photonics/sites/documents/99_SALES_LIBRARY/ssd/mppc_kapd9005e.pdf.

[Lor+15] G. Lorusso et al. "β-Decay Half-Lives of 110 Neutron-Rich Nuclei across the $N = 82$ Shell Gap: Implications for the Mechanism and Universality of the Astrophysical r Process". In: *Phys. Rev. Lett.* 114 (19 May 2015), p. 192501. DOI: 10.1103/PhysRevLett.114.192501. URL: https://link.aps.org/doi/10.1103/PhysRevLett.114.192501.

[Mar+17] N. Marginean et al. *GASPware*. 2017. URL: https://github.com/sztaylor89/GASPware-1.

[Mat+22] A Mattera et al. "Decay spectroscopy of the blocked fission product I 130". In: *Physical Review C* 106.6 (2022), p. 064326.

[MF14] Henryk Mach and Luis Mario Fraile. "Fast life-time measurements on fission products". In: *Hyperfine Interactions* 223.1 (2014), pp. 147–156.

[MGM89] H Mach, RL Gill, and M Moszyński. "A method for picosecond lifetime measurements for neutron-rich nuclei:(1) outline of the method". In: *Nuclear Instruments and Methods in Physics Research Section A: Accelerators, Spectrometers, Detectors and Associated Equipment* 280.1 (1989), pp. 49–72.

[Mic] MicroNotes. *"Introduction to Schottky Rectifiers"*. Tech. rep. URL: https://www.microsemi.com/sites/default/files/micnotes/401.pdf.

[Mic+18] Caterina Michelagnoli et al. "FIPPS (FIssion Product Prompt γ-ray Spectrometer) and its first experimental campaign". In: *EPJ Web of Conferences*. Vol. 193. EDP Sciences. 2018, p. 04009.

[Mih+20] C Mihai et al. "Development of large area Silicon Photomultipliers arrays for γ-ray spectroscopy applications". In: *Nuclear Instruments and Methods in Physics Research Section A: Accelerators, Spectrometers, Detectors and Associated Equipment* 953 (2020), p. 163263.

[MM89] M Moszyński and H Mach. "A method for picosecond lifetime measurements for neutron-rich nuclei:(2) Timing study with scintillation counters". In: *Nuclear Instruments and Methods in Physics Research Section A: Accelerators, Spectrometers, Detectors and Associated Equipment* 277.2-3 (1989), pp. 407–417.

[Moe+06] Sascha Moehrs et al. "A detector head design for small-animal PET with silicon photomultipliers (SiPM)". In: *Physics in Medicine & Biology* 51.5 (2006), p. 1113.

[Mus+95] MM Musthafa et al. "Semiclassical and quantum mechanical analysis of the excitation function for the Te 130 (p, n) I 130 reaction". In: *Physical Review C* 52.6 (1995), p. 3174.

[Mut17] Paolo Mutti. "Nuclear and Particle Physics at the Institute Laue-Langevin". In: *Nuclear Physics News* 27.1 (2017), pp. 6–12.

[Nak+19] Yuki Nakamura et al. “Characterization of SiPM optical crosstalk and its dependence on the protection-window thickness”. In: *Proceedings of the 5th International Workshop on New Photon-Detectors (PD18)*. 2019, p. 011003.

[Nes+20] D. A. Nesterenko et al. “Three beta-decaying states in ^{128}In and ^{130}In resolved for the first time using Penning-trap techniques”. In: *Phys.Lett. B* 808 (2020), p. 135642.

[Nog+06] G Noguere et al. “Neutron capture and total cross sections of ^{127}I and ^{129}I”. In: *Physical Review C* 74.5 (2006), p. 054602.

[Nut] Nutaq. *Nutaq data acquisition system*. Tech. rep. URL: https://nutaq.com/.

[ONS21a] ONSemi. *ON Semiconductor Technical note: "AND9770/D:Introduction to the Silicon Photomultiplier (SiPM)"*. Tech. rep. ON Semi), 2021. URL: https://www.onsemi.com/pub/Collateral/AND9770-D.PDF.

[ONS21b] ONSemi. *ON Semiconductor Technical note: "AND9778/D: Readout Mehotds for Arrays of SIlicon Photomultipliers"*. Tech. rep. ON Semi), 2021. URL: https://www.onsemi.com/pub/Collateral/AND9778-D.PDF.

[ONS21c] ONSemi. *ON Semiconductor Technical note: "AND9782/D: Biasing and Readout of ON Semiconductor SiPM Sensors"*. Tech. rep. ON Semi), 2021. URL: https://www.onsemi.com/pub/Collateral/AND9782-D.PDF.

[ONS21d] ONSemi. *ON Semiconductor Technical note: "ArrayJ Series"*. Tech. rep. ON Semi), 2021. URL: https://www.farnell.com/datasheets/2704146.pdf.

[Pau+89] Michael Paul et al. “Heavy ion separation with a gas-filled magnetic spectrograph”. In: *Nuclear Instruments and Methods in Physics Research Section A: Accelerators, Spectrometers, Detectors and Associated Equipment* 277.2-3 (1989), pp. 418–430.

[PN87] Robert F Pierret and Gerold W Neudeck. *Advanced semiconductor fundamentals*. Vol. 6. Addison-Wesley Reading, MA, 1987.

[Rad+05] D.C. Radford et al. “Coulomb excitation and transfer reactions with rare neutron-rich isotopes”. In: *Nuclear Physics A* 752 (2005). Proceedings of the 22nd International Nuclear Physics Conference (Part 2), pp. 264c–272c. ISSN: 0375-9474. DOI: https://doi.org/10.1016/j.nuclphysa.2005.02.040. URL: https://www.sciencedirect.com/science/article/pii/S0375947405001776.

[Ram08] Marco Ramilli. “Characterization of SiPM: temperature dependencies”. In: *2008 IEEE Nuclear Science Symposium Conference Record*. IEEE. 2008, pp. 2467–2470.

[RDJ18] J-M Régis, M Dannhoff, and J Jolie. "A simple procedure for γ-γ lifetime measurements using multi-element fast-timing arrays". In: *Nuclear Instruments and Methods in Physics Research Section A: Accelerators, Spectrometers, Detectors and Associated Equipment* 897 (2018), pp. 38–46.

[Rec+08] Ivan Rech et al. "Optical crosstalk in single photon avalanche diode arrays: a new complete model". In: *Optics express* 16.12 (2008), pp. 8381–8394.

[Rég+10] J-M Régis et al. "The mirror symmetric centroid difference method for picosecond lifetime measurements via γ–γ coincidences using very fast $LaBr_3$(Ce) scintillator detectors". In: *Nuclear Instruments and Methods in Physics Research Section A: Accelerators, Spectrometers, Detectors and Associated Equipment* 622.1 (2010), pp. 83–92.

[Rég+13] J-M Régis et al. "The generalized centroid difference method for picosecond sensitive determination of lifetimes of nuclear excited states using large fast-timing arrays". In: *Nuclear Instruments and Methods in Physics Research Section A: Accelerators, Spectrometers, Detectors and Associated Equipment* 726 (2013), pp. 191–202.

[Rég+14] J-M Régis et al. "Germanium-gated γ–γ fast timing of excited states in fission fragments using the EXILL&FATIMA spectrometer". In: *Nuclear Instruments and Methods in Physics Research Section A: Accelerators, Spectrometers, Detectors and Associated Equipment* 763 (2014), pp. 210–220.

[Rég+15] J-M Régis et al. "The Generalized Centroid Difference method for lifetime measurements via γ-γ coincidences using large fast-timing arrays". In: *EPJ Web of Conferences*. Vol. 93. EDP Sciences. 2015, p. 01013.

[Rég+16] J-M Régis et al. "Reduced γ–γ time walk to below 50 ps using the multiplexed-start and multiplexed-stop fast-timing technique with LaBr3 (Ce) detectors". In: *Nuclear Instruments and Methods in Physics Research Section A: Accelerators, Spectrometers, Detectors and Associated Equipment* 823 (2016), pp. 72–82.

[Rég+20] J-M Régis et al. "γ-γ fast timing at X-ray energies and investigation on various timing deviations". In: *Nuclear Instruments and Methods in Physics Research Section A: Accelerators, Spectrometers, Detectors and Associated Equipment* 955 (2020), p. 163258.

[Ren06] Dieter Renker. "Geiger-mode avalanche photodiodes, history, properties and problems". In: *Nuclear Instruments and Methods in Physics Research Section A: Accelerators, Spectrometers, Detectors and Associated Equipment* 567.1 (2006), pp. 48–56.

[Sae] N . Saed-Samii. *"SOCOV2 user manual"*. Tech. rep. Institute for Nuclear Physics University of Cologne(IKKP). URL: `https://gitlab.ikp.uni-koeln.de/nima/soco-v2/tree/master/manual`.

[Sak+89] SL Sakharov et al. "Low-lying 130I excited states from the (n, γ) reaction". In: *Nuclear Physics A* 494.1 (1989), pp. 36–74.

[San+19] V Sanchez-Tembleque et al. "Optimizing time-pickup algorithms in radiation detectors with a genetic algorithm". In: *Nuclear Instruments and Methods in Physics Research Section A: Accelerators, Spectrometers, Detectors and Associated Equipment* 927 (2019), pp. 54–62.

[Sik+05] G. Sikler et al. "Mass measurements on neutron-deficient Sr and neutron-rich Sn isotopes with the ISOLTRAP mass spectrometer". In: *Nuclear Physics A* 763 (2005), pp. 45–58. ISSN: 0375-9474. DOI: https://doi.org/10.1016/j.nuclphysa.2005.08.014. URL: https://www.sciencedirect.com/science/article/pii/S0375947405010584.

[SIN01] BALRAJ SINGH. "Nuclear Data Sheets for A = 130". In: *Nuclear Data Sheets* 93.1 (2001), pp. 33–242. ISSN: 0090-3752. DOI: https://doi.org/10.1006/ndsh.2001.0012. URL: https://www.sciencedirect.com/science/article/pii/S0090375201900122.

[SW22] Andrew E Stuchbery and John L Wood. "To Shell Model, or Not to Shell Model, That Is the Question". In: *Physics* 4.3 (2022), pp. 697–773.

[Tec21] Eljen Technologies. *ON Semiconductor Technical note: "AND9778/D: Readout Mehotds for Arrays of SIlicon Photomultipliers"*. Tech. rep. 2021. URL: https://eljentechnology.com/products/plastic-scintillators/ej-232-ej-232q..

[Ter+15] E Teruya et al. "Shell-model calculations of nuclei around mass 130". In: *Physical Review C* 92.3 (2015), p. 034320.

[Uni] Australian National University. *BrIcc Conversion Coefficient Calculator*. Tech. rep. URL: https://bricc.anu.edu.au/.

[Van+13] J. Van Schelt et al. "First Results from the CARIBU Facility: Mass Measurements on the r-Process Path". In: *Phys. Rev. Lett.* 111 (6 Aug. 2013), p. 061102. DOI: 10.1103/PhysRevLett.111.061102. URL: https://link.aps.org/doi/10.1103/PhysRevLett.111.061102.

[Ved] V. Vedia. "PhD thesis: Fast-timing investigation with $LaBr_2(Ce)$ arrays:detector optimization and measurements in ^{136}Te". In: ().

[Ved+] V Vedia et al. "Enhanced time response of 1-inch LaBr3 (Ce) crystals by leading edge and constant fraction techniques". In: ().

[Ved+17] V Vedia et al. "Performance evaluation of novel LaBr3 (Ce) scintillator geometries for fast-timing applications". In: *Nuclear Instruments and Methods in Physics Research Section A: Accelerators, Spectrometers, Detectors and Associated Equipment* 857 (2017), pp. 98–105.

[VPa] V.Paziy. "PhD thesis: Ultra fast timing study of exotic nuclei around ^{78}Ni: the β decay chain of ^{81}Zn". In: ().

[Wan+21] Meng Wang et al. “The AME 2020 atomic mass evaluation (II). Tables, graphs and references”. In: *Chinese Physics C* 45.3 (2021), p. 030003.

Scientific publications and conferences contributions

During this PhD thesis the following investigations were published in international journals relevant to the field.

Scientific publications in indexed international journals

1. B. Andel, P. Van Duppen, A. N. Andreyev, A. Blazhev, H. Grawe, R. Lica, H. Naïdja, M. Stryjczyk, A. Algora, S. Antalic, A. Barzakh, J. Benito, G. Benzoni, T. Berry, M. J. G. Borge, K. Chrysalidis, C. Clisu, C. Costache, J. G. Cubiss, H. De Witte,1 D. V. Fedorov, V. N. Fedosseev, L. M. Fraile, H. O. U. Fynbo, P. T. Greenlees, L. J. Harkness-Brennan, M. Huyse, A. Illana, J. Jolie, D. S. Judson, J. Konki, I. Lazarus, M. Madurga, N. Marginean, R. Marginean, C. Mihai, B. A. Marsh, P. Molkanov, P. Mosat, **J. R. Murias,**, E. Nacher, A. Negret, R. D. Page, S. Pascu, A. Perea, V. Pucknell, P. Rahkila, E. Rapisarda, K. Rezynkina, V. Sánchez-Tembleque, K. Schomacker, M. D. Seliverstov, C. Sotty, L. Stan,7 C. Sürder, O. Tengblad, V. Vedia, S. Viñals, R. Wadsworth, and N. Warr. New β-decaying state in ^{214}Bi. *Physical Review C 104:054301,2021*

2. A.K. Mistry, H.M. Albers, T. Arıcı, A. Banerjee, G. Benzoni, B. Cederwall, J. Gerl, M. Górska, O. Hall, N. Hubbard, I. Kojouharov, J. Jolie, T. Martinez, Zs. Podolyák, P.H. Regan, J.L. Tain, A. Tarifeno-Saldivia, H. Schaffner, V. Werner, G. Ağgez, J. Agramunt, U. Ahmed, O. Aktas 5, V. Alcayne, A. Algora, S. Alhomaidhi, F. Amjad, C. Appleton, M. Armstrong, M. Balogh , K. Banerjee, P. Bednarczyk, J. Benito, C. Bhattacharya, P. Black, A. Blazhev, S. Bottoni, P. Boutachkov, A. Bracco, A.M. Bruce, M. Brunet, C.G. Bruno, I. Burrows, F. Calvino, R.L. Canavan, D. Cano-Ott, M.M.R. Chishti, P. Coleman-Smith, M.L. Cortés, G. Cortes, F. Crespi, B. Das, T. Davinson, A. De Blas, T. Dickel, M. Doncel, A. Ertoprak, A. Esmaylzadeh, B. Fornal, L.M. Fraile, F. Galtarossa, A. Gottardo, V. Guadilla, J. Ha, E. Haettner, G. Häfner, H. Heggen, P. Herrmann, C. Hornung , S. Jazrawi, P.R. John, A. Jokinen , C.E. Jones, D. Kahl, V. Karayonchev, E. Kazantseva, R. Kern, L. Knafla,

R. Knöbel, P. Koseoglou, G. Kosir, D. Kostyleva, N. Kurz, N. Kuzminchuk, M. Labiche, J. Lawson, I. Lazarus, S.M. Lenzi, S. Leoni, M. Llanos-Expósito, R. Lozeva, A. Maj, J.K. Meena, E. Mendoza, R. Menegazzo, D. Mengoni, T.J. Mertzimekis, M. Mikolajczuk, B. Million, N. Mont-Geli, A.I. Morales, P. Morral, I. Mukha, **J.R. Murias**, E. Nacher, P. Napiralla, D.R. Napoli, B.S. Nara-Singh, D. O'Donnell, S.E.A. Orrigo, R.D. Page, R. Palit, M. Pallas, J. Pellumaj, S. Pelonis, H. Pentilla, A. Pérez de Rada, R.M. Pérez-Vidal, C.M. Petrache, N. Pietralla, S. Pietri, S. Pigliapoco, J. Plaza, M. Polettini, C. Porzio, V.F.E. Pucknell, F. Recchia, P. Reiter, K. Rezynkina, S. Rinta-Antila, E. Rocco, H.A. Rösch, P. Roy, B. Rubio, M. Rudigier, P. Ruotsalainen, S. Saha, E. Şahin, Ch. Scheidenberger , D.A. Seddon, L. Sexton, A. Sharma, M. Si, J. Simpson, A. Smith, R. Smith, P.A. Söderström, A. Sood, A. Soylu, Y.K. Tanaka, J.J. Valiente-Dobón, P. Vasileiou, J. Vasiljevic, J. Vesic, D. Villamarin, H. Weick, M. Wiebusch, J. Wiederhold, O. Wieland , H.J. Wollersheim, P.J. Woods, A. Yaneva, I. Zanon, G. Zhang, J. Zhao, R. Zidarova, G. Zimba, A. Zyriliou. The DESPEC setup for GSI and FAIR. *Nuclear Instruments and Methods in Physics Research A 1033:166662,2022*

Current publications being written and corrected by several collaborators

1. J. Benito, L. M. Fraile, A. Korgul, M. Piersa, E. Adamska, A. N. Andreyev, R. Álvarez-Rodríguez, A. E. Barzakh, G. Benzoni, T. Berry, M. J. G. Borge, M. Carmona, K. Chrysalidis, C. Costache, J. G. Cubiss, T. Day Goodacre, H. De Witte, D. V. Fedorov, V. N. Fedosseev, G. Fern¸ez-Martínez, A. Fijałkowska, M. Fila, H. Fynbo, D. Galaviz, P. Galve, M. García-Díez, P. T. Greenlees, R. Grzywacz, L. J. Harkness-Brennan, C. Henrich, M. Huyse, P. Ibáñez, A. Illana, Z. Janas, J. Jolie, D. S. Judson, V. Karayonchev, M. Kicińska-Habior, J. Konki, J. Kurcewicz, I. Lazarus, R. Lică, A. López-Montes, M. Lund, H. Mach, M. Madurga, I. Marroquín, B. Marsh, M. C. Martínez, Mazzocchi, C. N. Mărginean, R. Mărginean, K. Miernik, C. Mihai, R. E. Mihai, **J.R. Murias**, E. Nácher, A. Negret, B. Olaizola, R. D. Page, S. V. Paulauskas, S. Pascu, A. Perea, V. Pucknell, P. Rahkila, C. Raison, E. Rapisarda, J.-M. Régis, K. Rezynkina, F. Rotaru, S. Rothe, D. Sánchez-Parcerisa, V. Sánchez-Tembleque, K. Schomacker, G. S. Simpson, Ch. Sotty, L. Stan, M. Stănoiu, M. Stryjczyk, O. Tengblad, A. Turturica, J. M. Udías, P. Van Duppen, V. Vedia, A. Villa-Abaunza, S. Viñals, W. B. Walters, R. Wadsworth, N. Warr. Structure of ^{131}Sn populated in teh β-decay of isomerically-purified ^{131}In states.

2. **J.R. Murias**, L. M. Fraile, P. Mutti, E. Ruiz-Martinez, K. Olivier, J. M. Udías. Silicon Photomultiplier array based readout for $LaBr_3$(Ce) in fast-timing studies.

3. **J.R. Murias**, J. Benito, L. M. Fraile, A. Korgul, M. Piersa, E. Adamska, A. N. Andreyev, R. Álvarez-Rodríguez, A. E. Barzakh, G. Benzoni, T. Berry, M.

J. G. Borge, M. Carmona, K. Chrysalidis, C. Costache, J. G. Cubiss, T. Day Goodacre, H. De Witte, D. V. Fedorov, V. N. Fedosseev, G. Fern¸ez-Martínez, A. Fijałkowska, M. Fila, H. Fynbo, D. Galaviz, P. Galve, M. García-Díez, P. T. Greenlees, R. Grzywacz, L. J. Harkness-Brennan, C. Henrich, M. Huyse, P. Ibáñez, A. Illana, Z. Janas, J. Jolie, D. S. Judson, V. Karayonchev, M. Kicińska-Habior, J. Konki, J. Kurcewicz, I. Lazarus, R. Lică, A. López-Montes, M. Lund, H. Mach, M. Madurga, I. Marroquín, B. Marsh, M. C. Martínez, Mazzocchi, C. N. Mărginean, R. Mărginean, K. Miernik, C. Mihai, R. E. Mihai, E. Nácher, A. Negret, B. Olaizola, R. D. Page, S. V. Paulauskas, S. Pascu, A. Perea, V. Pucknell, P. Rahkila, C. Raison, E. Rapisarda, J.-M. Régis, K. Rezynkina, F. Rotaru, S. Rothe, D. Sánchez-Parcerisa, V. Sánchez-Tembleque, K. Schomacker, G. S. Simpson, Ch. Sotty, L. Stan, M. Stănoiu, M. Stryjczyk, O. Tengblad, A. Turturica, J. M. Udías, P. Van Duppen, V. Vedia, A. Villa-Abaunza, S. Viñals, W. B. Walters, R. Wadsworth, N. Warr. Population of ^{130}Sn from the three β-decaying states in ^{130}In.

Conference and workshop presentations

1. XXXVIII Bienal Meeting of the RSEF | RSEF and UM, *2022*. Oral Contribution: *"Investigation of ^{130}Sn populated in the β decay of isomerically-purified ^{130}In isomers"*

2. ANIMMA 2019,*2019*. Talk: *"Silicon photomultiplier based detectors for fast timing applications"*

3. IFIN-HH | ILL Recent results and perspectives at FIPPS, *2019*. Oral Contribution: *"Digital coincidence study with SiPM for nuclear structure studies"*

4. Annual PhD seminar at Institute Laue Langevin, *2019*. Oral Contribution: *"Neutron Scattering theory 1 Part II"*

5. Annual PhD seminar at Institute Laue Langevin, *2018*. Oral Contribution: *"Fast-timing at FIPPS with SiPM"*

6. Universidad Complutense Physics Postgraduate year workshop, *2018*. Oral Contribution: *"SiPM based fast scintillators for fast-timing applications"*